In-Situ Synchrotron X-Ray Studies of Microstructural Effects on Brittle Fracture

Thesis by

Sara Frances Gorske

In Partial Fulfillment of the Requirements for
the degree of
Doctor of Philosophy

CALIFORNIA INSTITUTE OF TECHNOLOGY
Pasadena, California

2026
(Defended May 5, 2026)

Sara Frances Gorske
ORCID: 0000-0002-1329-962

ACKNOWLEDGEMENTS

I would like to express my sincerest and deepest thanks to all those who supported me throughout this journey to my doctorate.

First, to my advisor Prof. Katherine Faber, for always believing in me even when I despaired that the work was too big and too hard, and for providing me with the groundwork to become a good scientist by always pushing me to ask more questions and dig deeper.

To my family: my parents, whose unconditional love and support got me through the hardest days, and who constantly reminded me who I am and what I can do; and my sister Libby, who reminded me to always stay positive and passionate.

To my committee members: Prof.s Kaushik Bhattacharya, Peter Voorhees, and Brent Fultz, for taking the time to care about this research and my readiness to graduate, and for the classes and meetings that have taught me so much.

To my collaborators and mentors in the ONR project, Prof.s Voorhees and Bhattacharya, and Prof. Blaise Bourdin, for continually asking questions that pushed me to refine my methods and presentations; and to my fellow students on the project, Dr. Mythreyi Ramesh and Carter Cocke, for expanding my knowledge of all the connections our work, and the fields of computation, materials science, and mechanical engineering, have to each other.

To my undergraduate advisor Prof. C. Rick Johnson, Jr., for providing me with the avenue to start research and for showing me what it looks like to unite multidisciplinary and extra-scientific passion into scientific research for great results.

To my labmates in the Faber group, for providing me with feedback on presentations, papers, and all the interim steps leading up to this thesis, with particular thanks to Dr. Benjamin Herren for showing me the synchrotron ropes, Dr. Celia Chari for encouraging me to stay interested in the art history world, and Dr. Kevin Yu for being the most knowledgeable cohort-mate I could have asked for.

To all the friends I've made here at Caltech, for showing me how great the world is when one doesn't shut oneself in a room all day to do work, and especially Dr. Cullen Quine for letting me be alternately weird, despondent, and manic whenever the situation demanded it, and for showing me what true scientific passion in the world at work looks like.

To the APhMS admins and staff, especially Christy Jenstad and Jennifer Blankenship, for all of the work they do to keep the department running while still having time to talk with and encourage students.

To the beamline scientists and collaborators at Argonne National Lab's Advanced Photon Source and the Cornell High Energy Synchrotron Source, for helping to make these experiments possible and providing invaluable guidance on setup, analysis, and scientific merit.

ABSTRACT

Brittle fracture, despite having been mathematically described more than a century ago, has remained a difficult topic of experimental and computational study. While the end states of brittle materials which have failed via fracture have been characterized using post-mortem fractography, sequential focused-ion beam studies, and tomography, the intermediate stages of brittle crack growth are difficult to study due to the unstable and fast nature of crack propagation. As a result, only partial characterization of a full crack front in a brittle material has been achieved, via two-dimensional studies or in simple systems that lack the complexity of most materials used in real-world applications. Presented in this thesis is a novel method of studying brittle cracks and their interaction with material microstructures using a combination of high-energy synchrotron X-ray radiation, precise loading, and a geometry capable of achieving stable crack growth, the double-cleavage drilled compression geometry. Cracks in two materials, a glass-ceramic with an alkali-aluminosilicate matrix and cubic crystals, and polycrystalline aluminum oxynitride, are characterized using this method. Full three-dimensional reconstructions of cracks at multiple loading steps are obtained via X-ray micro-computed tomography; the sizes, orientations, and strains of grains in the surrounding microstructures are characterized using both near-field and far-field high-energy diffraction microscopy; and the relationship between the crack paths and the microstructures is explored, elucidating behavior such as crack deflection in the presence of residual stress, intergranular versus transgranular crack motion through grains, and crack arrest after extension. Individual grain orientations and mechanical states are not found to be predictive as to whether a grain will crack in a certain manner, but average and cumulative properties for ensembles of grains around and ahead of the crack front have a significant effect on the length to which it extends and the fracture toughness.

PUBLISHED CONTENT AND CONTRIBUTIONS

Sections of this thesis were previously published in:

Gorske, S.F., Park, J-S., Kenesei, P., Sharma, H., Almer, J., Voorhees, P., Faber, K.T. "In-situ visualization of a growing brittle crack in aluminum oxynitride using synchrotron X-rays and the double-cleavage drilled compression geometry". In: *Acta Materialia*, vol. 312, 2026, 122213. https://doi.org/10.1016/j.actamat.2026.122213

S.F.G. participated in collecting, managing, and analyzing the synchrotron data; writing and developing code for analysis; writing the initial draft of the manuscript; and synthesizing comments and edits in later drafts.

Additional work is being prepared for publications:

Gorske, S.F., Shanks, K., Voorhees, P., Faber, K.T.. "3D brittle crack paths in an alkali-aluminosilicate glass-ceramic visualized in-situ using synchrotron X-rays and stable fracture geometry." In preparation.

S.F.G. is participating in collecting, managing, and analyzing the synchrotron data; writing and developing code for analysis; writing the initial draft of the manuscript; and will synthesize comments and edits in later drafts.

Gorske, S.F., Bhattacharya, K., Voorhees, P., Faber, K.T.. "Grain ensemble effects on brittle crack propagation using Voronoi-Laguerre tessellations verified against real microstructures." In preparation.

S.F.G. is participating in collecting, managing, and analyzing the synchrotron data; writing and developing code for analysis; writing the initial draft of the manuscript; and will synthesize comments and edits in later drafts.

Related work with portions inspired by or using parts of the datasets collected during experiments for this thesis:

Cocke, C.K., Akerson, A., **Gorske, S.F.**, Faber, K.T., Bhattacharya, K. "On recovering intragranular strain fields from grain-averaged strains obtained by high-energy X-ray diffraction microscopy". In: *Mathematics and Mechanics of Solids*, vol. 31, issue 1, 2026. https://doi.org/10.1177/10812865251376693

S.F.G. participated in collecting and managing the synchrotron data and provided edits and comments on manuscript drafts.

TABLE OF CONTENTS

LIST OF FIGURES

Number *Page*

LIST OF TABLES

Chapter 1

INTRODUCTION: BREAKING APART

Fracture is a word with nearly overwhelmingly negative connotations. Its close relatives—cracking, breaking, rupturing—generally relate to objects, relationships, and the like being sundered irrevocably. Consider the sad sighs and echoed consolations that follow the sentence, "We broke up," or the wince-inducing sound of a plate shattering on the ground, usually followed by a string of curse words. People do not like things to change, especially when that change is irreversible.

In materials science, the case is no different. The trouble is that fracture in many materials is not particularly predictable nor fully understood. Engineers using materials in applications have different criteria—the most well-known being the Tresca and von Mises criteria—for estimating when an object might fail [1]. However, even these are estimates, since real materials may have unknown flaws and may deviate from ideal models' stress states, and the users and vendors of these parts and materials are often advised to report an even smaller load to failure than calculated, just in case. When fracture is allowed, it is usually never meant to lead all the way to failure, and a growing crack is carefully monitored as it extends further into a material.

However, in many materials, that growing crack cannot be monitored due to the fact that its speed of advancement is simply too fast to be captured before catastrophic failure occurs. Further complicating the issue is that a subset of these materials undergoes only very limited, visually undetectable, plastic deformation, and some exhibit no plasticity whatsoever. As a consequence, cracks in these materials advance quickly, often progressing to failure in the same step as crack genesis, or pop-in [2]. These materials are termed brittle materials.

The earliest mathematical basis for brittle fracture was formulated more than a century ago by Griffith [3]. If this was all there was to the story, studying these materials would be much simpler than it actually is. However, Griffith and other early researchers into brittle fracture focused on ideal, isotropic, homogeneous structures with equally idealized cracks taking on nice geometric shapes and undergoing evenly distributed loads. Real materials,

however, are rarely homogeneous or isotropic, thus leading to uneven internal and external stresses and properties; real cracks are rarely straight or elliptical; and real samples have flaws both intrinsic and artificial, such as those induced by manufacturing [4]. As a result, brittle cracks are highly dependent on microstructure and rarely behave according to mathematical models for their entire lifetime, and much about how they progress is unknown due to the speed at which they break after the initial onset of failure.

As such, in order to use brittle materials in applications requiring them to perform well over a specific lifetime, many verification tests must be undertaken to determine their integrity, which is highly dependent on the size and density of flaws present in the material prior to its use, as well as how reproducible the microstructural conditions are. Testing criteria reliant on detecting the onset of plasticity or other phenomena indicating imminent or eventual fracture are limited in brittle materials due to the lack of plasticity. Instead, specific materials in specific geometries must be tested to failure many times, often hundreds or thousands, in order to create a Weibull distribution and to gain a statistical estimate of when fracture occurs in that material and geometry [5].

Of course, progress has been made in stopping the progression of cracks through materials both brittle and ductile alike. The incorporation of various inclusions of differing aspect ratios and sizes can lead to crack bridging, inducing additional constraints on a material that keep the crack from separating under a normally catastrophic load [6–8], or crack deflection, reorienting the crack into a region which might not be as conducive to further extension [9–12]. Interfaces in composites or grain boundaries can also serve as locations for crack deflection or arrest, and layered brittle materials or engineered grain boundaries are therefore attractive in some situations [13–15]. Some materials also rely on phase transformations ahead of the growing crack, which can blunt the crack's speed and hinder its progress [6,16]. However, some materials have no natural barriers to crack formation and cannot be engineered with additional fracture resistance without hampering the original intended use. Further utilization of these materials requires a better understanding of the conditions that cause failure, especially in situations where creating many thousands of parts for calculating a failure criterion is infeasible.

Past studies of brittle fracture have tended to fall into two categories: postmortem analyses and two-dimensional (2D) in-situ experiments. Types of post-mortem study include fractography, the study of already-fractured surfaces, as a way to investigate deviations along boundaries and crystallographic planes, and sequential focused-ion beam analysis to track the crack's shape change over progressively deeper layers [17–20]. However, this form of analysis requires an already failed sample and gives no insight into the shape of the crack front or location of the crack tip during arbitrary points during its growth phase. Some forms of postmortem measurements do allow for a three-dimensional (3D) crack front to be obtained without destroying the sample, such as by using tomography or acoustic methods combined with indentation, which usually does not cause ultimate failure in a material [21,22]. However, such methods are limited to the observation of a single fracture event for each indentation rather than a progressing crack front at multiple load steps. 2D experiments can more accurately measure the velocity of a crack front as it grows perpendicular to a surface, and can also detect branching and the opening of crack fronts that later closed due to the remission of stress at failure, if present and visible on the surface [23,24]. 2D methods cannot, however, visualize the crack front at other depths within the material and cannot therefore track any other interactions with interior microstructure.

One area of research addressing the unknown factors influencing brittle crack growth is modeling, which allows microstructures, stress and strain fields, and cracks to be simulated and subsequently monitored upon the application or change of environmental factors in time. An optimized model would ideally even be able to predict where and when a crack would appear and propagate in a material, given a few initial conditions. However, several limitations still apply to computational models. The first is that because brittle materials crack elastically, no plastic deformation zone exists to blunt the crack, giving it a sharp tip acting as a singularity in the stress field [25,26]. In order to accurately capture that stress field, nodes in the model mesh at which calculations occur must be made progressively denser in the volume near to the crack tip, drastically increasing computational time and complexity. Furthermore, no matter how small the voxels are that are associated with each node, that singularity can never be fully described by finite voxels, limiting understanding of how the stress field develops and impacts the path of a growing crack. Secondly, models on their own

can serve only as elaborate guesswork without combining them and verifying them against experimental observations to be sure that the equations, initial conditions, and simulations are accurately capturing the realities of materials and samples.

A promising method for mitigating the meshing issue is to use a phase-field (PF) model in place of methods such as finite element analysis (FEA). FEA models have been used in many engineering and physics computations, as properties at nodes can be finely tuned to create conditions imitating real-life situations and experiments. However, cracks can be difficult to model, not only because of the singularity at the tip, but because upon separation of the bulk material, and movement of the crack tip the mesh must be recomputed [27,28]. PF models, on the other hand, use continuum mechanics to create smoothly varying fields of properties throughout a volume, changes in which affect the entirety of the studied region. A material's closeness to cracking or its having been already cracked are also properties that can be tracked. As such, PF models are increasingly being explored for use in modeling fracture, especially in brittle materials [29,30].

The work presented in this thesis addresses the need for model verification as well as the unknowns in our current understanding of brittle fracture by capturing the progression of a real crack in a real microstructure in real time. By performing tests at a synchrotron X-ray facility, the interior of a fracturing brittle material can be viewed, and many types of experiment performed with a fast acquisition rate. The high resolution of synchrotron X-rays also allows small features, including narrow cracks and small grains, to be viewed and tracked spatially, which many laboratory systems cannot achieve. Specifically, diffraction experiments can reveal aspects of the microstructure of a material before, after, and during crack propagation, while tomography experiments can capture the extent of the growing crack. By using a geometry capable of stable crack propagation, these experiments can be performed and data collected for brittle materials with a crack within them over multiple iterations of crack growth. This thesis explores the results of performing these types of experiments on several different brittle materials with the purpose of collaborating with PF modelers to enhance knowledge of where cracks propagate and grow in real microstructures.

Chapter 2 of this thesis covers the theoretical basics of brittle fracture and presents the experimental method used at the synchrotron, including the material geometry and the types

of X-ray techniques along with the method of load application, before introducing the classes of materials studied in the next chapters. Chapter 3 describes experiments performed on the first material, a glass-ceramic, for the purpose of determining to what extent a second phase present in an isotropic matrix impacts crack growth. Chapter 4 presents similar experiments performed on aluminum oxynitride, an anisotropic polycrystalline material, to explore the effect of larger grains and grain boundaries on crack path. Chapter 5 extends the aluminum oxynitride experiments by using Voronoi-Laguerre tessellations to estimate microstructure in regions where it was not precisely obtained, and uses additional data not examined in Chapter 4 to examine the effects collections of many grains have upon the crack as compared to the effect of individual grains. Chapter 6 concludes the thesis, speculates on the effects of this work on the field of brittle fracture, and presents ideas for the future direction of this work and the field in general, in both designing experiments and connecting them to computational models.

Bibliography

[1] Elements of solid mechanics, in: Fracture Mechanics with an Introduction to Micromechanics, Springer, 2006: pp. 1–38. https://doi.org/10.1007/b22134.
[2] Unstable crack propagation: dynamic fracture, in: Fracture of Brittle Solids, 2nd ed., Cambridge University Press, 1993: pp. 86–105. https://doi.org/10.1017/CBO9780511623127.
[3] The Griffith concept, in: Fracture of Brittle Solids, 2nd ed., Cambridge University Press, 1993: pp. 1–15. https://doi.org/10.1017/CBO9780511623127.
[4] Crack initiation: flaws, in: Fracture of Brittle Solids, 2nd ed., Cambridge University Press, 1993: pp. 307–334. https://doi.org/10.1017/CBO9780511623127.
[5] Strength and reliability, in: Fracture of Brittle Solids, 2nd ed., Cambridge University Press, 1993: pp. 335–362. https://doi.org/10.1017/CBO9780511623127.
[6] Microstructure and toughness, in: Fracture of Brittle Solids, 2nd ed., Cambridge University Press, 1993: pp. 194–248. https://doi.org/10.1017/CBO9780511623127.
[7] M. Bannister, H. Shercliff, G. Bao, F. Zok, M.F. Ashby, Toughening in brittle systems by ductile bridging ligaments, *Acta Metall Mater* 40 (1992) 1531–1537. https://doi.org/10.1016/0956-7151(92)90096-W.
[8] C. Redon, J.-L. Chermant, Compactness of the cement microstructure versus crack bridging in mortars reinforced with amorphous cast iron fibers and silica Ffumes, *Appl Compos Mater* 8 (2001) 149–161. https://doi.org/10.1023/A:1011245515368.
[9] K.T. Faber, A.G. Evans, Crack deflection processes—I. Theory, *Acta Metall* 31 (1983) 565–576. https://doi.org/10.1016/0001-6160(83)90046-9.
[10] K.T. Faber, A.G. Evans, Crack deflection processes—II. Experiment, *Acta Metall* 31 (1983) 577–584. https://doi.org/10.1016/0001-6160(83)90047-0.
[11] H.W. Chandler, I.J. Merchant, R.J. Henderson, D.E. Macphee, Enhanced crack-bridging by unbonded inclusions in a brittle matrix, *J Eur Ceram Soc* 22 (2002) 129–134. https://doi.org/10.1016/S0955-2219(01)00242-4.
[12] N.R. Brodnik, C.-J. Hsueh, K.T. Faber, B. Bourdin, G. Ravichandran, K. Bhattacharya, Guiding and trapping cracks With compliant inclusions for enhancing toughness of brittle composite materials, *J Appl Mech* 87 (2020). https://doi.org/10.1115/1.4045682.
[13] K.T. Faber, Ceramic composite interfaces: properties and design, *Annu Rev Mater Sci* 27 (1997) 499–524. https://doi.org/10.1146/annurev.matsci.27.1.499.
[14] R. Daniel, M. Meindlhumer, W. Baumegger, J. Zalesak, B. Sartory, M. Burghammer, C. Mitterer, J. Keckes, Grain boundary design of thin films: Using tilted brittle interfaces for multiple crack deflection toughening, *Acta Mater* 122 (2017) 130–137. https://doi.org/10.1016/j.actamat.2016.09.027.
[15] J.J.-W. Lee, I.K. Lloyd, H. Chai, Y.-G. Jung, B.R. Lawn, Arrest, deflection, penetration and reinitiation of cracks in brittle layers across adhesive interlayers, *Acta Mater* 55 (2007) 5859–5866. https://doi.org/10.1016/j.actamat.2007.06.038.
[16] R.H.J. Hannink, P.M. Kelly, B.C. Muddle, Transformation toughening in zirconia-containing ceramics, *J Amer Ceram Soc* 83 (2000) 461–487. https://doi.org/10.1111/j.1151-2916.2000.tb01221.x.

[17] J. Delage, E. Saiz, N. Al Nasiri, Fracture behaviour of SiC/SiC ceramic matrix composite at room temperature, *J Eur Ceram Soc* 42 (2022) 3156–3167. https://doi.org/10.1016/j.jeurceramsoc.2022.01.060.
[18] A.L. Horovistiz, J.R. Frade, L.R.O. Hein, Comparison of fracture surface and plane section analysis for ceramic grain size characterisation, *J Eur Ceram Soc* 24 (2004) 619–626. https://doi.org/10.1016/S0955-2219(03)00260-7.
[19] A.D. Spear, S.F. Li, J.F. Lind, R.M. Suter, A.R. Ingraffea, Three-dimensional characterization of microstructurally small fatigue-crack evolution using quantitative fractography combined with post-mortem X-ray tomography and high-energy X-ray diffraction microscopy, *Acta Mater* 76 (2014) 413–424. https://doi.org/10.1016/j.actamat.2014.05.021.
[20] S.S. Scherrer, J.B. Quinn, G.D. Quinn, J.R. Kelly, Failure analysis of ceramic clinical cases using qualitative fractography., *Int J Prosthodont* 19 (2006) 185–192.
[21] G. Okuma, K. Maeda, S. Yoshida, A. Takeuchi, F. Wakai, Morphology of subsurface cracks in glass-ceramics induced by Vickers indentation observed by synchrotron X-ray multiscale tomography, *Sci Rep* 12 (2022) 6994. https://doi.org/10.1038/s41598-022-11084-0.
[22] J.J. Guo, K. Wang, T. Fujita, J.W. McCauley, J.P. Singh, M.W. Chen, Nanoindentation characterization of deformation and failure of aluminum oxynitride, *Acta Mater* 59 (2011) 1671–1679. https://doi.org/10.1016/j.actamat.2010.11.034.
[23] O. Preuß, Z. Li, E. Bruder, P. Carrez, Y. Cui, J. Rödel, X. Fang, Stable crack propagation in dislocation-engineered oxide visualized by double cleavage drilled compression test, *J Eur Ceram Soc* 46 (2026) 117905. https://doi.org/10.1016/j.jeurceramsoc.2025.117905.
[24] P.L. Swanson, C.J. Fairbanks, B.R. Lawn, Y.-W. Mai, B.J. Hockey, Crack-Interface Grain Bridging as a Fracture Resistance I, Mechanism in Ceramics: I, Experimental Study on Alumina, *J Amer Ceram Soc* 70 (1987) 279–289. https://doi.org/10.1111/j.1151-2916.1987.tb04982.x.
[25] S. Goswami, W. Becker, Computation of 3-D stress singularities for multiple cracks and crack intersections by the scaled boundary finite element method, *Int J Fract* 175 (2012) 13–25. https://doi.org/10.1007/s10704-012-9694-2.
[26] Continuum aspects of crack propagation I: linear elastic crack-tip field, in: Fracture of Brittle Solids, 2nd ed., Cambridge University Press, Cambridge, 1993: pp. 16–50. https://doi.org/10.1017/CBO9780511623127.
[27] A. Pascuzzo, F. Greco, P. Lonetti, D. Ammendolea, Dynamic fracture analysis in quasi-brittle materials via a finite element approach based on the combination of the ALE formulation and M−integral method, *Eng Fail Anal* 141 (2022) 106627. https://doi.org/10.1016/j.engfailanal.2022.106627.
[28] S. Mariani, U. Perego, Extended finite element method for quasi-brittle fracture, *Int J Numer Meth Eng* 58 (2003) 103–126. https://doi.org/10.1002/nme.761.
[29] C. Kuhn, R. Müller, A phase field model for fracture, *Proc Appl Math Mec* 8 (2008) 10223–10224. https://doi.org/10.1002/pamm.200810223.
[30] A. Kumar, B. Bourdin, G.A. Francfort, O. Lopez-Pamies, Revisiting nucleation in the phase-field approach to brittle fracture, *J Mech Phys Solids* 142 (2020) 104027. https://doi.org/10.1016/j.jmps.2020.104027.

Chapter 2

BACKGROUND: BREAKING IT DOWN

2.1 The initial problem: defining brittle fracture mathematically

At the most basic level, the propagation of a brittle crack can be defined by an energy balance. Griffith developed an equation to describe when a brittle crack will propagate spontaneously from an existing elliptical flaw (Equation 2.1); the two energetic factors are the stress generated ahead of a crack tip, the release of which would decrease the stored potential energy in the region, and the energetic cost to break atomic bonds to create new surfaces [1,2].

$$\sigma_e = \sqrt{\frac{2E'\gamma}{\pi c_0}} \qquad \text{Equation 2.1}$$

σ_e = load at extension E' = modulus for sample geometry γ = surface energy
c_0 = crack length prior to extension

In the simple case of this single, perfectly elliptical crack located in an isotropic, homogenous matrix, when the applied load exceeds the value defined above, the crack will propagate spontaneously to failure. While real cracks and real materials are more complex, Griffith's formulation became a basis for further developments in understanding brittle fracture. A more general treatment of brittle fracture reveals the same energy-balance concept between mechanical and potential energies, such that crack extension can be related to the change in the sample conditions, such as when load is applied. A quantity known as the energy release rate can subsequently be calculated (Equation 2.2), the form of which can indicate whether a crack will extend and if it is stable or unstable while doing so by comparing it to the intrinsic work in the sample opposing crack extension, sometimes termed crack resistance (Equation 2.3) [3,4].

$$G = -\frac{\partial U_E}{\partial C} \qquad \text{Equation 2.2}$$

U_E = work done to extend the crack C = crack area $\propto$ crack length c

$$G_C = \frac{\partial U_S}{\partial C} \qquad \text{Equation 2.3}$$

U_S = energy opposing crack extension

Under equilibrium conditions, crack extension occurs when the intrinsic forces within the sample can be overcome, that is, when $G > G_C$. As G is a function of crack length, its value changes with extension; if it continues to increase, that is, $\partial G/\partial C > 0$, it remains favorable to extend the crack, and propagation will continue unstably. Conversely, when $\partial G/\partial C < 0$, the crack is stable and extension will halt. The examination of energetic quantities related to crack extension later led to Irwin's formulation of solutions for the stress and strain in the volume ahead of the crack [3,4]. The stress field ahead of a crack tip has remained an important factor in fracture studies, especially in modeling, where its proper calculation and minimization is crucial in determining a crack's direction upon propagation [5].

For homogeneous, isotropic materials, the stress field is well-defined for existing cracks in each of the three main modes of brittle fracture (Figure 2.1) [4]. In Mode I fracture, the load is tensile and directed across the crack, serving to open it wider and extend it deeper; this is the dominant mode in brittle fracture due to the lack of shear forces acting on the crack. Mode II fracture occurs when stresses are applied parallel to the direction of extension of the crack, but with opposite signs on either side, essentially sliding the two sections of material along each other until bonds break. In Mode III fracture, the loads are applied parallel to the crack opening, again with opposite signs, such that the material fractures via a tearing motion. The Irwin crack-top solutions for stress in all modes have the form $\sigma \propto r^{1/2}$, indicating a concentration of stress near the crack tip that drops off with greater distance. The extent of stress concentration is governed by a factor known as the stress-intensity factor, *K*, which is different for each mode and dependent on the sample loading, boundary conditions, and crack length [3]. The total stress-intensity in a region is additive between the three modes, indicating that a crack can be mixed-mode when the forces on it are not purely one type [4].

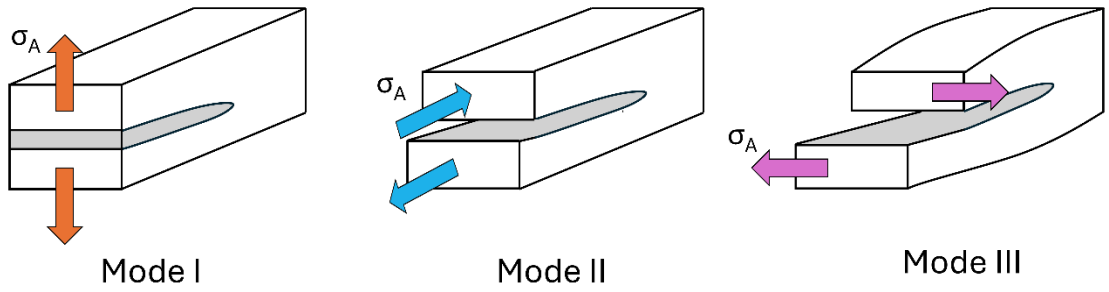

Figure 2.1: The three modes of fracture, with the direction of applied load indicated.

The stress-intensity factor is related to the energy-release rate, such that there is also a critical value governing crack propagation and stability, K_c, which is termed the fracture toughness. As Mode I tends to be the dominant mode in brittle fracture and the modeling of it, the Mode I fracture toughness, K_{Ic}, is often the reported value [4].

$$G = \frac{K^2}{E'} \qquad \text{Equation 2.4}$$

2.2 The instability problem: achieving stable fracture with the DCDC geometry

Several limitations have thus far precluded a full investigation covering the entire lifetime of a growing brittle crack. Foremost among these issues is the velocity at which the crack front grows, which, when coupled with the sudden onset of crack initiation and brittle fracture's tendency to be unstable, means that the crack has often progressed to failure before data collection can begin [6]. Additionally, even if crack initiation is caught on camera, very little data on the crack's shape and location can be captured at the frequencies of data collection at which many instruments operate. Trying to capture 3D data, which usually requires collecting multiple sets of data at different angles for a sample at a single state, is usually not attempted, with any in-situ experiments being limited to the 2D observable plane [7,8]. Therefore, studies are often limited to postmortem fractography, studying surfaces after materials have failed and the interior stress state has changed significantly so that it no longer represents that observed during the fracture experiment [7,9]. Thus, a necessity in any experiment aimed at capturing data over multiple iterations of a growing crack is a sample geometry which can sustain stable crack growth.

A solution to the problem of brittle crack instability is to use a geometry capable of halting the crack's motion. While materials exist which hinder crack propagation through the inclusion of second phases or self-healing, this does not provide a way to investigate general brittle materials. The double-cleavage drilled compression (DCDC) geometry was proposed in 1977 in order to achieve the phenomenon of stable crack growth in brittle materials, particularly glass [10]. Modifications and variations have since been tested, but the original DCDC sample is a parallelepiped with one dimension significantly longer than the others (Figure 2.2) [11,12]. In one of the long faces, a hold is drilled directly into the center. When the sample is compressed along its longest dimension, tensile stress is generated at the upper and lower poles of the hole. At some load, those tensile forces will be sufficient to pop in a crack on the top and bottom of the sample. Eventually, the energy required to extend the crack forward through the internal strain field is insufficient, stopping the crack from extending further and thus achieving stable fracture. The resultant crack tip will in turn experience tensile forces working to open it, and at increased load, the crack will once more extend.

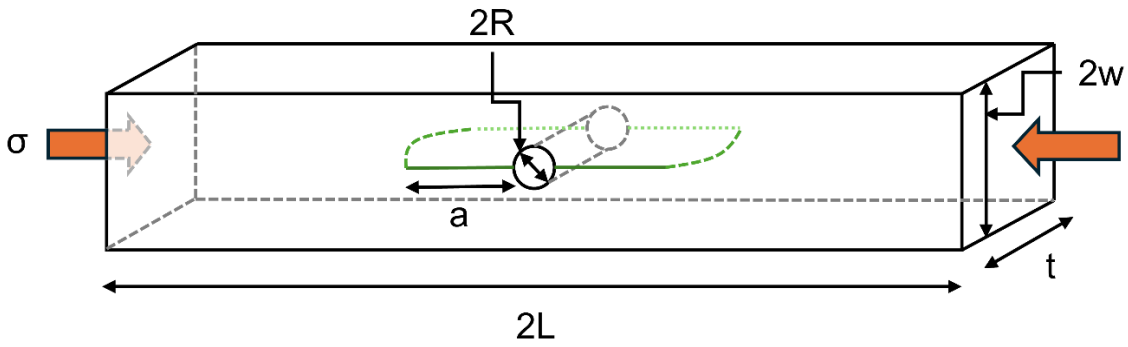

Figure 2.2: The DCDC geometry, with the directions of loading (orange arrows) and crack growth (green planes) shown.

As it was initially designed for use in glass, DCDC studies have been performed on a variety of glasses as well as other isotropic, homogeneous materials such as polymers [13,14]. The DCDC sample has also been a subject of interest in modeling, both for tracking stable fracture computationally as well as testing crack nucleation modeling, which has historically been a challenge to capture, partially because of the statistically variant presence

and density of micro-cracks and defects [11–13,15,16]. As such, the conditions under which a crack grows in the DCDC geometry can be captured to an extent by equations, which allow for the calculation of the stress-intensity factor and fracture toughness of materials. For the isotropic, homogeneous, ideal model, the crack grows in pure Mode I fracture. Using known quantities including the sample dimensions, crack length, and applied compressive load, its fracture toughness is given by Equation 2.5 [17].

$$K_I = \frac{\sigma\sqrt{\pi R}}{\beta + 0.235\beta\alpha - 0.259\alpha} \left(\beta = \frac{w}{R}, \alpha = \frac{a}{R}, \beta \le \alpha \le 15, 2 \le \beta \le 4\right) \quad \text{Equation 2.5}$$

a = crack front depth w = half sample width (Figure 2.1)

R = hole radius σ = overall compressive load

Observed stable crack growth occurs in the region of $w < c < 15R$ where the crack is neither very short, and thus impacted by the stress field of the hole, nor very long, where the crack is becoming unstable and close to spontaneous complete fracture. Equations cannot, however, predict exactly the load required for pop-in, which is impacted by statistical variables such as the presence and number of microcracks [18,19].

The stability of the crack can be confirmed by calculating the sign of $\partial G/\partial c$ keeping in mind that α, β, and R are all positive quantities (Equations 2.6-2.7).

$$G = \frac{K_I^2}{E'} = \frac{\sigma^2\pi R}{E'}[\beta + 0.235\beta\alpha - 0.259\alpha]^{-2} \quad \text{Equation 2.6}$$

$$\frac{\partial G}{\partial c} = \frac{\partial G}{\partial(\alpha R)} = \frac{1}{R}\frac{\partial G}{\partial \alpha} = -2\frac{\sigma^2\pi}{E'}[\beta + 0.235\beta\alpha - 0.259\alpha]^{-3}[0.235\beta - 0.259] \quad \text{Equation 2.7a}$$

$$0.235\beta - 0.259 \begin{cases} > 0, & w > 1.1R \\ < 0, & R < w < 1.1R \end{cases} \quad \text{Equation 2.7b}$$

$$\beta + 0.235\beta\alpha - 0.259\alpha = \beta + \alpha(0.235\beta - 0.259) \begin{cases} > 0, & w > 1.1R \\ > 0, & R < w < 1.1R, w \le c \le 15R \end{cases} \quad \text{Equation 2.7c}$$

Thus when $w > 1.1R$, the two bracketed components (Equations 2.7b-c) will both be positive, and the overall expression for $\partial G/\partial c$ will be negative, making the crack stable at all crack lengths. However, for $R < w < 1.1R$, the components will have opposite signs for the admissible crack lengths, and $\partial G/\partial c$ will be positive. Thus, for stability, the DCDC hole radius should be smaller than 91% the half-width of the sample.

2.3 The interior problem: obtaining 3D views of the crack and surrounding microstructure with synchrotron X-ray techniques

Requisite to calculating the fracture toughness in a DCDC sample and identifying the crack tip location and any variations in the crack front shape is obtaining a full 3D model of the crack within the sample. As their wavelengths are close to interatomic spacings, X-rays are a natural solution to viewing the interior of materials. Synchrotron sources produce X-rays with high enough energies to penetrate and pass through macroscopic samples nondestructively. As a result, obtain multiple sources of information can be obtained, describing both the sample and any potential fractures within it [20].

X-rays occupy the energies of the electromagnetic spectrum greater than ultraviolet light and lower than gamma rays; that is, energies in approximately the range 10^2 to 10^6 eV [20]. Correspondingly, their wavelengths are in approximately the picometer to nanometer range, as described by the relationship between energy and wavelength for all forms of light (Equation 2.8).

$$E = \frac{hc}{\lambda} \qquad \text{Equation 2.8}$$

h = Planck's constant (6.626×10^{-34} J·s) $\quad$ c = speed of light (2.9979×10^{8} m/s) $\quad$ λ = wavelength

At synchrotron sources, X-rays are generated when electrons, which move around a circular building called a storage ring, are accelerated. These electrons move close to the speed of light, and without acceleration would propagate along a straight line; however, using insertion devices and undulators, which generate magnetic forces, the electrons' path is deflected [21]. The acceleration involved in changing the electrons' direction of motion results in a loss of both energy and momentum, which is compensated for by the generation

of X-rays. Stations equipped with instrumentation for various X-ray techniques are located along the resultant path of the X-rays (beamlines), and have further methods of tuning the X-ray beam's energy, collimation, and size to that desired for the specific technique being used [22].

Most relevant to studying the shape and length of a crack front is X-ray computed tomography (XCT). This technique leverages the different X-ray interactions of different elements, and their arrangement into different phases and materials, to build a picture of the interior of the sample. In fracture experiments, the crack appears distinct in XCT images, as its composition of air necessarily differs from the bulk of the sample [23]. When there are multiple materials contained within a sample, they will also be easily differentiable as a result of the different elements or concentrations of elements in them. Thus, the crack can be related to the location, size, and type of material within such a sample [24].

Two main forms of XCT exist: absorption contrast and phase contrast. The former reflects the fact that in regions of high X-ray absorption, which normally increases for elements of higher atomic number [23], fewer of those X-rays will reach the detector, thus building an image from the varying intensity of detected light. A single image taken using this technique, as might be familiar from a dentist's office, merely provides information on which regions in a 2D projection absorbed more X-rays, and therefore had fewer X-rays reach the detector. When images of multiple 2D projections are collected at sequential angles while rotating the sample, every point within the sample can be associated with each of the linear projections passing through it to build a 3D model of phase, density, and material [24,25].

Phase contrast, on the other hand, works by determining where X-rays have undergone a phase shift upon encountering regions of different material or atomic arrangement with a different refractive index. The phase is an integral part of defining the wavefunction of quantum phenomena, including light and X-rays. Simply using the same method and detectors used in absorption contrast is insufficient, because the phase is contained in the complex exponential part of the wavefunction. This value does not affect the intensity of the wave, which is calculated using the complex conjugate and which is what is measured by most detectors [25]. However, when waves of different phases interact, they can do so

constructively or destructively, which does change the signal. Therefore, in regions where the phase has changed, the wavefunction will deviate from that emitted by the X-ray source. To obtain phase contrast data, detectors can be placed at short distances from the sample, before the interference has propagated and become indistinguishable upon mixing with light in many other phase shifts. By rotating the sample and collecting 2D projections, just as in absorption contrast, these changes in the wavefunction and their effect on the measured signal amplitude and frequency can provide information on the edges and faces where the phase change was induced [24].

As phase contrast does not rely on absorption differences to build the tomographic volume, it can be performed even with very high energy X-rays, which would otherwise pass through many materials with very little absorption and which would thus provide little contrast in absorption contrast XCT experiments [24]. As a result, the beam can be tuned to the best energy for any other techniques being performed during the duration of the synchrotron experiment, many of which are optimized at higher energies. Additionally, materials with very little internal elemental composition difference or with elements with close absorption coefficients but with density or atomic arrangement differences can have these differences revealed as a result of a phase change [25]. For fracture experiments in particular, phase contrast XCT is attractive as the crack's location can be highlighted by a phase shift even when it is very thin and does not change the overall absorption of the sample by much, rendering it hard to detect using just absorption contrast [26]. The narrow crack opening width of brittle cracks is also a reason to use synchrotron XCT instead of commercially available instruments; the resolution at synchrotron beamlines is often on the micron or sub-micron scale, allowing for further precision in describing the crack front. For this reason, the technique is often known as micro-computed tomography (μ-CT).

Regardless of the tomography technique and energy used, knowing the location and extent of the crack is only part of the story. When the sample is composed of a single material type, even if it is polycrystalline or contains different arrangements of the same atomic composition, there will be very few apparent features near the crack, and further techniques are required in order to describe the microstructure around the crack and to relate the two.

X-ray diffraction (XRD) is one of the best-known applications of X-rays in material characterization. Because X-ray wavelengths are similar in size to interatomic spacings in materials, their diffraction from stacked atomic layers can result in amplification, dampening, or extinguishment of the X-ray wave depending on how much the phase is shifted after interacting with the sample [27]. At most angles, the phase changes as a result of scattering are randomly scrambled and interfere destructively. When X-ray light impinges on a grain at the right angle, however, the resulting reflected wave off of a certain lattice plane will have the same phase as the incoming wave, thus amplifying the signal at that angle. The relationship between where X-rays diffract and the atomic planes is described by Bragg's Law (Equation 2.9).

$$d_{hkl} \cdot \sin\theta = \lambda \qquad \text{Equation 2.9}$$

λ = X-ray wavelength θ = diffraction angle d_{hkl} = lattice spacing

$$d_{hkl} = \frac{1}{\sqrt{\frac{h}{a_0}^2 + \frac{k}{b_0}^2 + \frac{l}{c_0}^2}} \qquad \text{Equation 2.10}$$

a_0, b_0, c_0 = unit cell lattice parameters h, k, l = Miller indices

In a polycrystalline sample, each crystal or grain will diffract individually. While the relationship between d and θ is maintained, the same diffraction condition is not met for every grain at a single sample rotation angle ω [28]. Planes of the same family in grains of different orientations will still produce a diffracted beam angled at θ to the incident beam, but the diffracted beam also has an angular component η depending on the orientation of the lattice. As a result, diffraction from one set of planes defines a cone with an opening angle of 2θ, and a detector placed downstream of the sample will receive signals along a ring corresponding to that diffraction condition [29,30]. The size of the ring on the detector is dependent on the sample-to-detector distance, which also affects the maximum θ able to be detected.

The number of spots corresponding to a specific d-spacing is equal to the multiplicity of the corresponding plane, and thus each grain will diffract at multiple orientations relative to the incoming beam. These diffraction spots will all occur for the same θ, but at different

positions η around the corresponding diffraction ring depending on the relative orientation of the grain to the sample. Collecting all the diffraction spots for every diffracting θ for every grain requires rotating the sample through a full 360° circuit, similarly to the 180° rotation used in XCT. Additionally, because of crystal imperfections, the diffraction spot may be smeared over multiple rotation angles and some distribution in θ and η. Such imperfections include the finite size of grains, faults such as dopants or dislocations which create a distribution in lattice spacing, and crystal strain putting the lattice under tension or compression. As a result, diffraction spots become 3D features in reciprocal space containing much more information than simply the spacing between lattice planes [29,30]. Consolidating the information from all of the diffraction spots corresponding to a single grain can provide insight into that grain beyond its material makeup.

Laboratory-size XRD instruments produce the same information as synchrotron sources about which *d*-spacings diffract and at what relative intensities; however, they usually provide only the summed intensity of all detected diffraction at a given θ. The high brilliance of synchrotron X-ray radiation and the greater resolution of the detectors at beamlines allow for much more precision in this measurement because the signal-to-noise ratio is improved as the diffracted beams are more coherent with higher intensity [27]. By using high-energy diffraction microscopy (HEDM), high-quality information on individual diffraction spots can be collected.

Far-field HEDM (FF-HEDM) is a technique where the detector is placed a meter or more downstream of the sample, where it captures and records diffraction spots from rings with $\cos\theta \leq h/2L$ (Figure 2.3), where L is the distance between the sample and the detector, and h is the smallest dimension of the detector [31]. By evaluating the spots in reciprocal space, information on the granular scale can be obtained.

The first piece of information to be extracted from a diffraction pattern is the orientation. Taking a particular θ ring as a seed, the spots in that ring, which have a known multiplicity, can be associated with particular grains. From there, all possible spot patterns for each grain in the other rings can be generated. When one of those possibilities matches well with a set of actual detected spots, the grain's orientation can be assigned, and from there other calculations become possible [29–31]. The orientation can be represented in a number of

ways, including the rotation matrix Q, the quaternion, and a set of three Euler angles, all of which indicate how to transform the unit cell of a grain in the reference configuration to its orientation in the sample frame, and thus its orientation relative to the other grains in a volume.

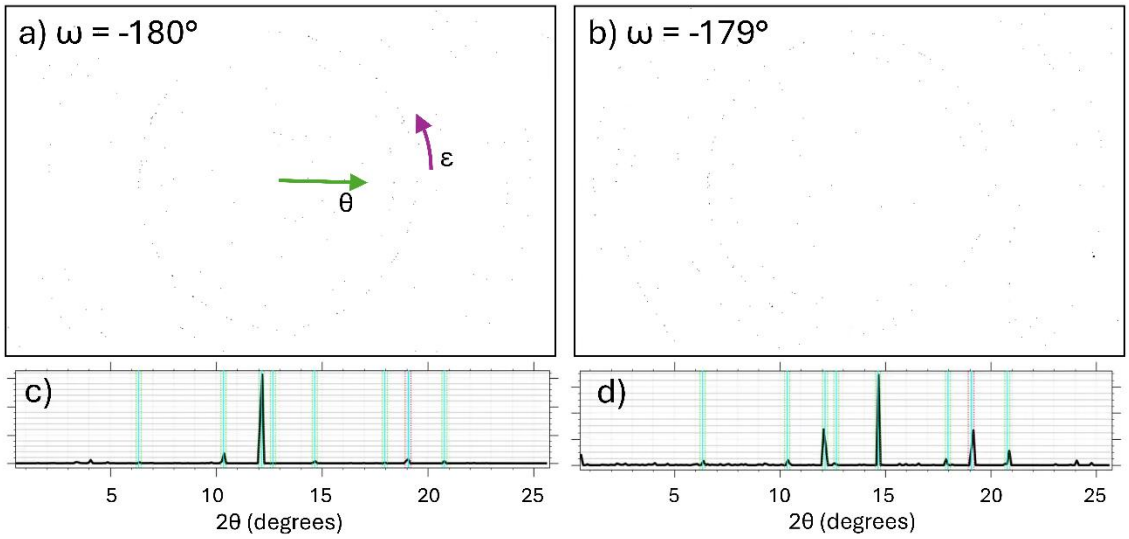

Figure 2.3: a-b) Detected signals on an FF-HEDM detector at the Cornell High Energy Synchrotron Source. A measurement is taken at different rotation angles ω and diffraction signals are recorded on rings corresponding to θ in the Bragg diffraction condition. c-d) Summing the rings' signals radially produces graphs of the signal intensity in θ, with the same peaks but different relative intensities.

As a grain under an amount of strain will present with lattice parameters different than those under no strain, being compressed or in tension, the values of d which satisfy the Bragg condition will be altered, and thus the resultant diffraction spots will be shifted from the ideal θ. Using a detector which collects every diffracting spot for a grain further allows all six fundamental lattice parameters (three lengths and three angles) to be obtained for that grain, based on how the shifts in the spots corresponding to different sample rotations, and therefore different relative grain orientations, differ [32]. These parameters can then be used to build a strain tensor for the grain using Equations 2.11-13 [28–30].

$$\varepsilon_{ij} = \frac{1}{2}\left(T_{ij} + T_{ji}\right) - \delta_{ij} \qquad \text{Equation 2.11}$$

$$T_{ij} = A_{ik}A_{0\,kj}^{-1} \quad \text{Equation 2.12}$$

$$A = \begin{pmatrix} a & b\cos(\gamma) & c\cos(\beta) \\ 0 & b\sin(\gamma) & -c\sin(\beta)\cos(\alpha^*) \\ 0 & 0 & c\sin(\beta)\sin(\alpha^*) \end{pmatrix} \quad \text{Equation 2.13}$$

A_0 uses unstrained lattice parameters

$a, b, c, \alpha, \beta, \gamma$ = strained lattice parameters

ε = strain tensor

a_0 … : unstrained lattice parameters

α^* … : reciprocal lattice parameters

δ_{ij} = Kronecker delta

For a cubic unit cell, where the angular lattice parameters are equal to 90° and the sides of the unit cell are equal in length, A_0 is equal to the lattice parameter a_0 along the diagonal and is zero elsewhere, but the relative deformation in each direction is not equal. Some HEDM methods report the strain tensor in relation to the left stretch tensor V, which describes the amount by which the unit cell vectors in the deformed basis have been changed from their unstrained state (Equations 2.14-18) [33].

$$\varepsilon_{ij} = \frac{1}{2}(C_{ij} - \delta_{ij}) \quad \text{Equation 2.14}$$

$$C = \sum_{i=1}^{3} \lambda_i^2 \hat{p_\imath}\, \hat{p_\imath} \quad \text{Equation 2.15}$$

$$U = \sum_{i=1}^{3} \lambda_i \hat{p_\imath}\, \hat{p_\imath} \quad \text{Equation 2.16}$$

$$\hat{q_\imath} = Q\hat{p_\imath} \quad \text{Equation 2.17}$$

$$V = \sum_{i=1}^{3} \lambda_i \hat{q_\imath}\, \hat{q_\imath} \quad \text{Equation 2.18}$$

C = right Cauchy-Green deformation tensor

U = right stretch tensor

V = left stretch tensor

$\hat{p_\imath}$ = principal material directions

$\hat{q_\imath}$ = principal spatial directions

λ_i = principal stretches (eigenvalues of U and V)

Q = rotation matrix (grain reference frame to sample frame)

By considering the strain tensor using the definitions of deformation, it follows that ε_{11}, ε_{22}, and ε_{33} represent changes in relative length of the unit cell's sides, related to the principal stretches represented in V. The off-axis or shear terms represent angular deformation, and are often small. Obtaining the strain tensor, with its information on the deformation of the unit cell, for each grain provides information on the relative response for each grain and volume [34,35]. Knowledge of the material's anisotropic stiffness tensor can further be used to calculate the stress tensor for each grain (Equation 2.19), which describes the distribution and direction of the forces in each grain and can be related to the overall load on the sample and the pressures on grains from their neighbors [36].

$$\sigma_{ij} = C_{ijkl}\varepsilon_{kl} \qquad \text{Equation 2.19}$$

σ = stress tensor $\qquad$ C = stiffness tensor

Additionally, an estimate of grain size can be obtained via HEDM. An ideal, infinite crystal will present with a sharp diffraction peak in an XRD map, as its infinite size means that any diffracted X-ray which reaches the detector has undergone perfect constructive interference. However, real, finite crystals, even if they have no imperfections, will not have the same level of constructive interference, as only a finite amount of waves have been summed to create the signal. As a result, the XRD peaks broaden around the Bragg conditions in θ, and this can give an estimate of the crystal size when enough diffraction spots are considered [27,29,30].

Finally, just as in XCT, the knowledge of the sample's rotation and where diffraction occurred for each grain allows its center of mass to be estimated, giving it a position within the sample. In a fracture experiment, this allows grain proximity to the crack to be considered [37,38].

However, FF-HEDM does not provide information on whether grains close to the crack were actually intersected by it. Thus, another method, near-field HEDM (NF-HEDM), can be performed as a corollary. In this method, a detector is brought within 20 mm of the sample, and the diffracted beams are detected before much interference has occurred, just as in phase-contrast XCT [31,32]. In this case, the information being gathered is not the phase-shift of light, but rather a more detailed spatial map of diffraction.

Unlike FF-HEDM, which can only capture the center of mass of the grain due to the limited nature of the small diffraction spots, using NF-HEDM, the shape and size of the grains along with their location in space can be obtained. The interrogating beam is made smaller in height than the grains, such that only a limited amount of light is interacting with the sample, and thus only a few grains are diffracting at any one time. By performing scans at multiple sample-to-detector distances, the point of origin for the angular spread of a diffraction spot can be obtained, and the diffraction signal can be related spatially to the material the X-rays have passed through [28,31,32]. Since the grains are all oriented differently and diffracting at different sample rotation angles, a grain satisfying a Bragg condition at a given sample rotation angle will generally be distinct on the detector, especially for the high-symmetry angles with low reciprocity and therefore low spot overlap (Figure 2.4) [39]. At such close sample-to-detector distances, the diffraction spot no longer covers only a few voxels on the detector. Instead, its size on the detector is directly related to the amount of the incident beam that was diffracted by that grain; that is, the grain's width in that direction. Additionally, diffraction conditions at steeper angles pass through more of the vertical dimension of the grain, and therefore diffraction spots from lower symmetry planes provide additional information on the grain's vertical dimension.

While most NF-HEDM reconstruction methods work off of the assumption of each grain having constant orientation and strain values in order to perform the forward reconstruction that allows for orientation identification, some amount of intragranular variance can be detected [31,39]. A diffraction spot can be present across multiple sample rotations (Figure 2.4). If the spot remains in the same diffraction ring, a single interatomic spacing d_{hkl} must satisfy the Bragg condition in multiple regions of the grain at different rotations ω, indicating some amount of orientation fluctuation within the grain. If instead it shifts in θ, d_{hkl} must have a spread of values within the grain, indicating likely intragranular strain variance; work is currently being done to progress such intragranular reconstructions [31,35,40].

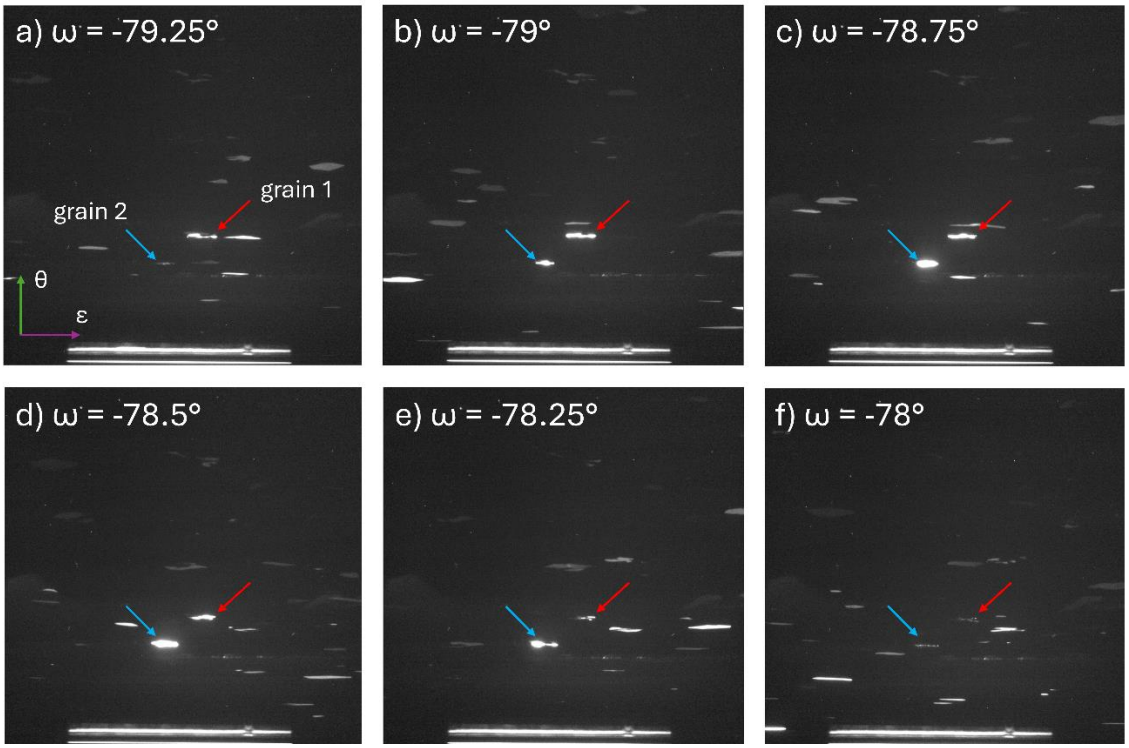

Figure 2.4: NF-HEDM measurements taken at sequential sample rotations at Argonne National Laboratory's Advanced Photon Source. Many grains are evident at each rotation, satisfying some Bragg condition, while a few grains are present across multiple rotations at the same height, corresponding to the value of θ.

Similarly to FF-HEDM, processing NF-HEDM information starts with the orientation. Usually using FF-HEDM grain orientations as a seed, a 2D map of nodes is created for each scan and a forward reconstruction is performed to determine if diffraction from that spatial point in any of the seeded orientations matches the observations [31]. Each voxel is then assigned a grain and orientation, which may differ slightly from the average orientation found during FF-HEDM, along with a confidence value indicating how sure it is that the assigned grain is the correct one. Confidence values usually drop off near grain boundaries as a point may partially match the projected signals from multiple neighboring grains. The result is a 2D orientation map that reveals grain contours and boundaries. Performing multiple sequential NF-HEDM scans in a volume permits reconstructing the grains and approximate grain boundaries in 3D.

The linchpin to performing a successful synchrotron experiment with a growing crack in a DCDC sample is a fixture that can apply both load and rotation to the sample. The Rotational and Axial Motion System (RAMS) designed by Dr. Paul Shade and colleagues at the Air Force Research Laboratory performs both these functions (Figure 2.5) [41]. The stage of RAMS also rotates independently of the frame of the fixture, with the grips rotating in tandem, so that the supports between the upper and lower parts of the fixture never rotate into the beam, which would block the X-rays from reaching the sample uninhibited. A key design parameter was to keep translation of the center of rotation minimal even during rotation, which is crucial for reconstructing tomography and HEDM data; reported tolerances report the center of rotation moves no more than 1 μm during application of more than 1000 N of load or during 90° of rotation. The sample can also be moved laterally in the three main axes of the sample frame of reference: along the beam direction (z) and in two perpendicular directions, vertically up and down (y) and horizontally left and right (x). Thus scanning multiple volumes becomes achievable.

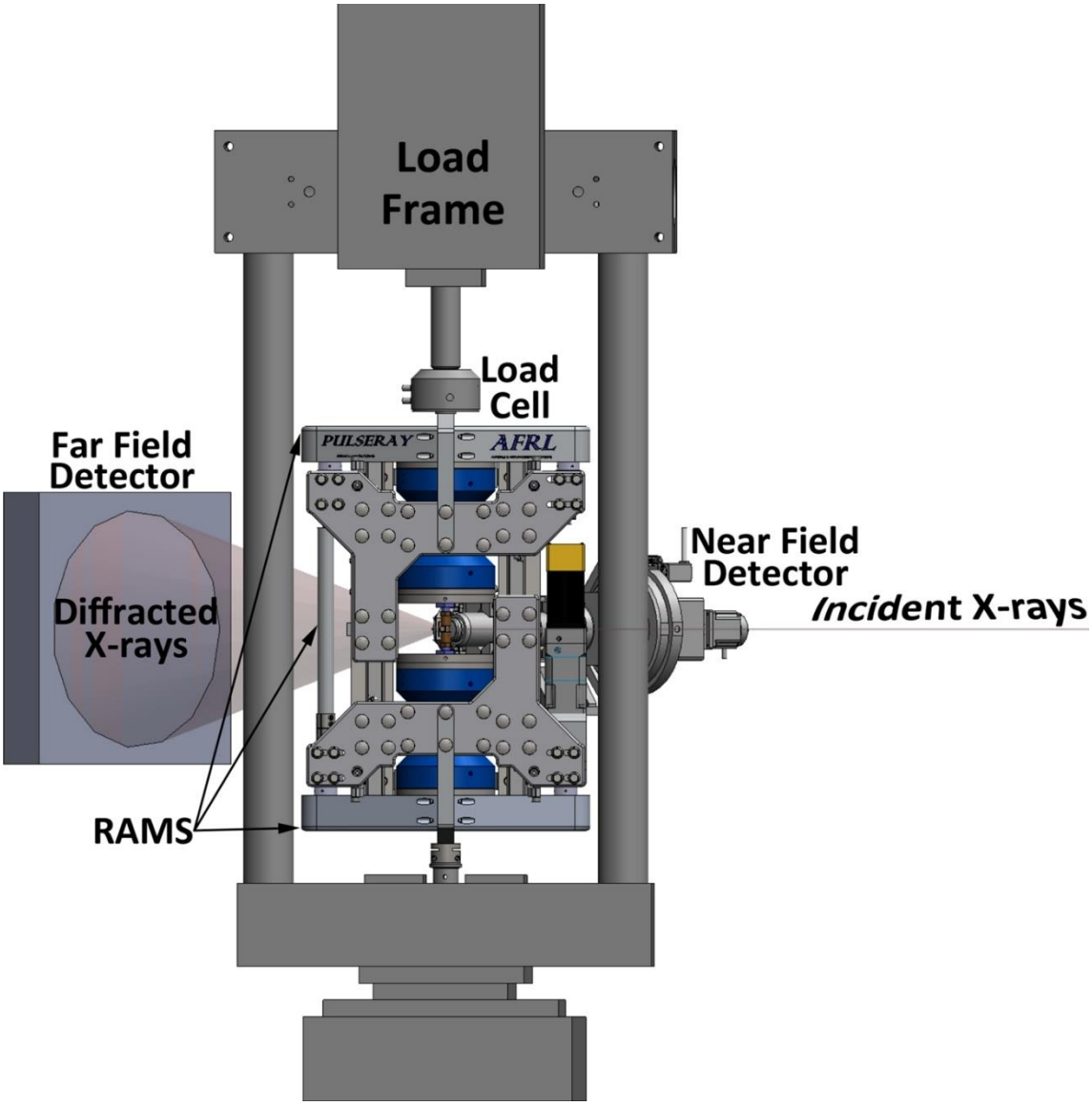

Figure 2.5: The Rotational and Axial Motion System designed by Shade et al. at the Air Force Research Laboratory, reproduced with permission from [41].

2.4 The idealization problem: moving beyond isotropic and homogeneous models to real materials

By combining synchrotron techniques like XCT and HEDM with mechanical loading, detailed relationships between microstructure and fracture characteristics can be obtained. Fatigue in metals has been studied using the combination of these techniques to great success [26,37,38,42–45], and work has been done on loose collections of brittle grains [46,47] as

well as porous ceramics and other brittle materials [48,49]. However, work remains to be done on fully dense brittle materials, where pores can neither deflect a growing crack away from the bulk nor halt its motion. Using this setup with the DCDC geometry, describing both the microstructure around a crack and the crack itself becomes possible. However, obtaining HEDM information on grain orientation and stress is not applicable to the homogeneous, isotropic materials previously used in DCDC studies, nor is the result novel, since the relationship between the DCDC crack in such a material and the load is already well-documented. Additionally, most materials used in real situations are not isotropic nor homogeneous; in order to apply insights about brittle fracture to applied materials, similarly complex materials must be studied.

Inhomogeneities and directional properties that vary throughout a material impact how, when, and where a crack will propagate [4,18,19]. With those factors described by prior knowledge of material properties and the sample-specific data obtained via XCT and HEDM, the growth of a crack through a sample can be related to specific material qualities and properties, which can assist in developing materials for specific applications and in more fully understanding when and how a material may fail.

Introducing inhomogeneity into a material has implications on these stress fields. In a polycrystal, each grain will have different overall stress and strain tensors than its neighbors and the bulk, due to the applied load being distributed differently upon grains of different orientations, size, and residual stress; furthermore, the stress and strain may vary within grains as a result of proximity to grain boundaries with grains with different properties or other phases [50–54]. Thus, the stress field from the crack will not present with perfectly symmetrical isosurfaces, impacting how much mixed-mode fracture occurs along the length of the crack front.

An expansion beyond a homogeneous, isotropic material is to use an isotropic matrix phase with a second, crystalline, phase suspended within it. As the two phases have different mechanical properties, including fracture toughness, the crack's path, while primarily through the matrix phase, will be influenced by the second phase. If the second phase has a lower fracture toughness than its surroundings, the crack may be attracted to its particles, since it is more energetically favorable to crack through them than the matrix. In the opposite

case, where the second phase has greater fracture toughness than the matrix, the crack may be deflected away from the particles when its path would otherwise pass through them [50,55,56].

A class of brittle materials satisfying this condition are glass-ceramics. Glass-ceramics are usually a mix of oxides, taken up past their melting points until the melt is homogeneous, then cooled such that the bulk of the material remains as an isotropic glass but second-phase particles precipitate out and remain suspended in the bulk, mixed throughout the solid [57–59]. Because of this method of production, they do not have to be fabricated out of two separate phases, which has implications on the residual stress around the second-phase particles.

Further extending study into anisotropic materials, polycrystals with no isotropic phase can be explored. When regular lattices are arranged as grains, the differences in orientation, grain size, and any residual stresses throughout the material create a rich interplay of forces that results in an uneven stress distribution throughout different regions and volumes of the material even when a single, static, stress is applied [60–62]. The changes in orientation and observed stress can change the local fracture toughness and may not only attract or deflect the crack near certain grains, as with the second-phase particles, but also determine whether a crack can pass through a grain (transgranular cracking) or will be forced to go around it, following grain boundaries (intergranular cracking) [50,63,64]. Furthermore, because of the stable cracking of the DCDC geometry, crack extension will eventually be arrested until application of further load, and gaining information on where the crack is arrested in relation to grain boundaries and grain orientations is important information in understanding local fracture toughness and crack stability.

While information on which particles were cracked, and the overall shape of the crack, including deviations from the ideal DCDC geometry's central, straight Mode I fracture surface, can be obtained using post-mortem fractography, looking at free surfaces after fracture does not provide information on the stress and strain states of individual particles in the region of fracture. Scanning a volume ahead of the crack tip using HEDM, however, can provide this information. Linking the stress and strain tensor components, along with orientation and size, to whether grains attracted or deflected the crack during growth, can

enrich understanding of the effect of localized fracture toughness and its connection to mechanical and physical parameters. Such information not only provides insight into the system at hand, but is also critical in developing models to predict fracture and other phenomena in brittle materials. The experiments presented in this thesis represent, to the author's knowledge, the first set of in-situ observations of the 3D nature of a growing crack and surrounding microstructure at multiple stages in fully dense brittle materials.

Bibliography

[1] Micro and macro phenomena of fracture, in: Fracture Mechanics with an Introduction to Micromechanics, Springer, 2006: pp. 59–135. https://doi.org/10.1007/b22134.
[2] The Griffith Concept, in: Fracture of Brittle Solids, 2nd ed., Cambridge University Press, 1993: pp. 1–15. https://doi.org/10.1017/CBO9780511623127.
[3] Linear fracture mechanics, in: Fracture Mechanics with an Introduction to Micromechanics, Springer, 2006: pp. 49–57. https://doi.org/10.1007/b22134.
[4] Continuum aspects of crack propagation I: linear elastic crack-tip field, in: Fracture of Brittle Solids, 2nd ed., Cambridge University Press, Cambridge, 1993: pp. 16–50. https://doi.org/10.1017/CBO9780511623127.
[5] A. Schlüter, A. Willenbücher, C. Kuhn, R. Müller, Phase field approximation of dynamic brittle fracture, *Comput Mech* 54 (2014) 1141–1161. https://doi.org/10.1007/s00466-014-1045-x.
[6] Unstable crack propagation: dynamic fracture, in: Fracture of Brittle Solids, 2nd ed., Cambridge University Press, 1993: pp. 86–105. https://doi.org/10.1017/CBO9780511623127.
[7] J. Delage, E. Saiz, N. Al Nasiri, Fracture behaviour of SiC/SiC ceramic matrix composite at room temperature, *J Eur Ceram Soc* 42 (2022) 3156–3167. https://doi.org/10.1016/j.jeurceramsoc.2022.01.060.
[8] P.L. Swanson, C.J. Fairbanks, B.R. Lawn, Y.-W. Mai, B.J. Hockey, Crack-interface grain bridging as a fracture resistance I, mechanism in ceramics: I, experimental study on alumina, *J Am Ceram Soc* 70 (1987) 279–289. https://doi.org/10.1111/j.1151-2916.1987.tb04982.x.
[9] S.S. Scherrer, J.B. Quinn, G.D. Quinn, J.R. Kelly, Failure analysis of ceramic clinical cases using qualitative fractography., *Int J Prosthodont* 19 (2006) 185–192.
[10] Ch. Janssen, Specimen for fracture mechanics studies on glass, *Rev Phys Appl* (Paris) 12 (1977) 803–803. https://doi.org/10.1051/rphysap:01977001205080300.
[11] M.Y. He, M.R. Turner, A.G. Evans, Analysis of the double cleavage drilled compression specimen for interface fracture energy measurements over a range of mode mixities, *Acta Metall et Mater* 43 (1995) 3453–3458. https://doi.org/10.1016/0956-7151(95)00036-U.
[12] T. Fett, G. Rizzi, J.P. Guin, J.M. López-Cepero, S.M. Wiederhorn, A fracture mechanics analysis of the double cleavage drilled compression test specimen, *Eng Fract Mech* 76 (2009) 921–934. https://doi.org/10.1016/j.engfracmech.2008.12.016.
[13] T.A. Plaisted, A.V. Amirkhizi, S. Nemat-Nasser, Compression-induced axial crack propagation in DCDC polymer samples: experiments and modeling, *Int J Fract* 141 (2006) 447–457. https://doi.org/10.1007/s10704-006-9006-9.
[14] G. Pallares, L. Ponson, A. Grimaldi, M. George, G. Prevot, M. Ciccotti, Crack opening profile in DCDC specimen, *Int J Fract* 156 (2009). https://doi.org/10.1007/s10704-009-9341-8.
[15] T.A. Michalske, W.L. Smith, E.P. Chen, Stress intensity calibration for the double cleavage drilled compression specimen, *Eng Fract Mech* 45 (1993) 637–642. https://doi.org/10.1016/0013-7944(93)90269-X.

[16] A. Kumar, B. Bourdin, G.A. Francfort, O. Lopez-Pamies, Revisiting nucleation in the phase-field approach to brittle fracture, *J Mech Phys Solids* 142 (2020) 104027. https://doi.org/10.1016/j.jmps.2020.104027.
[17] Q.Z. Wang, M. Ni, L.Z. Wu, R.Q. Huang, Scrutinized and revised stress intensity factor formulas for double cleavage drilled compression specimens, *Theor Appl Fract Mec* 96 (2018) 803–810. https://doi.org/10.1016/j.tafmec.2017.11.008.
[18] Crack initiation: flaws, in: Fracture of Brittle Solids, 2nd ed., Cambridge University Press, 1993: pp. 307–334. https://doi.org/10.1017/CBO9780511623127.
[19] Strength and reliability, in: Fracture of Brittle Solids, 2nd ed., Cambridge University Press, 1993: pp. 335–362. https://doi.org/10.1017/CBO9780511623127.
[20] Introduction, in: An Introduction to Synchrotron Radiation: Techniques and Applications, John Wiley and Sons, Ltd, 2011: pp. 1–14.
[21] S. Krinsky, Fundamentals of Hard X-ray Synchrotron Radiation Sources, in: D.M. Mills (Ed.) Third-Generation Hard X-Ray Synchrotron Sources: Source Properties, Optics, and Experimental Techniques, John Wiley and Sons, Ltd, 2002: pp. 1–40.
[22] Beamlines, in: An Introduction to Synchrotron Radiation: Techniques and Applications, John Wiley and Sons, Ltd, 2011: pp. 87–131.
[23] The Interaction of X-rays with Matter, in: An Introduction to Synchrotron Radiation: Techniques and Applications, John Wiley and Sons, Ltd, 2011.
[24] Imaging Techniques, in: An Introduction to Synchrotron Radiation: Techniques and Applications, John Wiley and Sons, Ltd, 2011: pp. 303–337.
[25] J. Baruchel, P. Cloetens, J. Härtwig, M. Schlenker, Imaging with Third-Generation Synchrotron X-rays, in: D.M. Mills (Ed.), Third-Generation Hard X-Ray Synchrotron Sources: Source Properties, Optics, and Experimental Techniques, John Wiley and Sons, Ltd, 2002: pp. 181–202.
[26] C. Xiao, J.-Y. Buffière, J.M. Létang, W. Ludwig, Investigation of wrinkle artifacts along metallic fatigue cracks in phase contrast synchrotron tomography via simulations and experiments, *Mater Charact* 194 (2022) 112431. https://doi.org/10.1016/j.matchar.2022.112431.
[27] Scattering Techniques, in: An Introduction to Synchrotron Radiation: Techniques and Applications, John Wiley and Sons, Ltd, 2011: pp. 133–221.
[28] Geometric Principles, in: Three-Dimensional X-Ray Diffraction Microscopy, Springer, n.d.: pp. 21–34.
[29] H. Sharma, R.M. Huizenga, S.E. Offerman, A fast methodology to determine the characteristics of thousands of grains using three-dimensional X-ray diffraction. I. Overlapping diffraction peaks and parameters of the experimental setup, *J Appl Cryst* 45 (2012) 693–704. https://doi.org/10.1107/S0021889812025563.
[30] H. Sharma, R.M. Huizenga, S.E. Offerman, A fast methodology to determine the characteristics of thousands of grains using three-dimensional X-ray diffraction. II. Volume, centre-of-mass position, crystallographic orientation and strain state of grains, *J Appl Cryst* 45 (2012) 705–718. https://doi.org/10.1107/S0021889812025599.
[31] K.E. Nygren, D.C. Pagan, J.V. Bernier, M.P. Miller, An algorithm for resolving intragranular orientation fields using coupled far-field and near-field high energy X-ray diffraction microscopy, *Mater Charact* 165 (2020) 110366. https://doi.org/10.1016/j.matchar.2020.110366.

[32] J.C. Schuren, P.A. Shade, J.V. Bernier, S.F. Li, B. Blank, J. Lind, P. Kenesei, U. Lienert, R.M. Suter, T.J. Turner, D.M. Dimiduk, J. Almer, New opportunities for quantitative tracking of polycrystal responses in three dimensions, *Curr Opin Solid St M* 19 (2015) 235–244. https://doi.org/10.1016/j.cossms.2014.11.003.
[33] Kinematics of Continua, in: An Introduction to Continuum Mechanics with Applications, Cambridge University Press, n.d.: pp. 61–114.
[34] P.A. Shade, W.D. Musinski, M. Obstalecki, D.C. Pagan, A.J. Beaudoin, J.V. Bernier, T.J. Turner, Exploring new links between crystal plasticity models and high-energy X-ray diffraction microscopy, *Curr Opin Solid St M* 23 (2019) 100763. https://doi.org/10.1016/j.cossms.2019.07.002.
[35] W. Li, H. Sharma, P. Kenesei, S. Ravi, H. Sehitoglu, A. Bucsek, Resolving intragranular stress fields in plastically deformed titanium using point-focused high-energy diffraction microscopy, *J Mater Res* 38 (2023) 165–178. https://doi.org/10.1557/s43578-022-00873-y.
[36] Constitutive Equations, in: An Introduction to Continuum Mechanics with Applications, Cambridge University Press, n.d.: pp. 178–209.
[37] D.P. Naragani, P.A. Shade, P. Kenesei, H. Sharma, M.D. Sangid, X-ray characterization of the micromechanical response ahead of a propagating small fatigue crack in a Ni-based superalloy, *Acta Mater* 179 (2019) 342–359. https://doi.org/10.1016/j.actamat.2019.08.005.
[38] J.P. Hanson, A. Bagri, J. Lind, P. Kenesei, R.M. Suter, S. Gradečak, M.J. Demkowicz, Crystallographic character of grain boundaries resistant to hydrogen-assisted fracture in Ni-base alloy 725, *Nat Commun* 9 (2018) 3386. https://doi.org/10.1038/s41467-018-05549-y.
[39] GRAINDEX and Related Analysis, in: Three-Dimensional X-Ray Diffraction Microscopy, Springer, n.d.: pp. 35–50.
[40] Y.-F. Shen, H. Liu, R.M. Suter, Voxel-based strain tensors from near-field High Energy Diffraction Microscopy, *Curr Opin Solid St M* Science 24 (2020) 100852. https://doi.org/10.1016/j.cossms.2020.100852.
[41] P.A. Shade, B. Blank, J.C. Schuren, T.J. Turner, P. Kenesei, K. Goetze, R.M. Suter, J.V. Bernier, S.F. Li, J. Lind, U. Lienert, J. Almer, A rotational and axial motion system load frame insert for in situ high energy x-ray studies, *Rev Sci Instrum* 86 (2015) 093902. https://doi.org/10.1063/1.4927855.
[42] W. Chen, J. Xu, C. Ding, D. Shan, B. Guo, T.G. Langdon, Fracture mechanism of electrically-assisted micro-tension in nanostructured titanium using synchrotron radiation X-ray tomography, *Scripta Mater* 222 (2023) 114997. https://doi.org/10.1016/j.scriptamat.2022.114997.
[43] D.J. Shadle, M.P. Miller, K.E. Nygren, Using real-time data analysis to conduct next-generation synchrotron fatigue studies, *Int J Fatigue* 164 (2022) 107113. https://doi.org/10.1016/j.ijfatigue.2022.107113.
[44] M. Herbig, A. King, P. Reischig, H. Proudhon, E.M. Lauridsen, J. Marrow, J.-Y. Buffière, W. Ludwig, 3-D growth of a short fatigue crack within a polycrystalline microstructure studied using combined diffraction and phase-contrast X-ray tomography, *Acta Mater* 59 (2011) 590–601. https://doi.org/10.1016/j.actamat.2010.09.063.
[45] S.E. Gustafson, D.C. Pagan, P.A. Shade, M.D. Sangid, Dynamic recovery observed in distinct grains within a polycrystalline nickel-based superalloy during cyclic high

temperature fatigue via high energy X-ray diffraction microscopy, *Scripta Mater* 192 (2021) 37–42. https://doi.org/10.1016/j.scriptamat.2020.10.004.
[46] M.B. Cil, K.A. Alshibli, P. Kenesei, 3D experimental measurement of lattice strain and fracture behavior of sand Particles using Synchrotron X-ray diffraction and tomography, *J Geotech Geoenviron* 143 (2017) 04017048. https://doi.org/10.1061/(ASCE)GT.1943-5606.0001737.
[47] Z.A. Jarrar, K.A. Alshibli, R.I. Al-Raoush, Three-dimensional evaluation of sand particle fracture using discrete-element method and synchrotron microcomputed tomography images, *J Geotech Geoenviron* 146 (2020) 06020007. https://doi.org/10.1061/(ASCE)GT.1943-5606.0002281.
[48] S.Y. Kim, M.L. Sesso, G.V. Franks, In-situ 4-point flexural testing and synchrotron micro X-ray computed tomography of 3D printed hierarchical-porous ultra-high temperature ceramic, *Addit Manuf* 54 (2022) 102728. https://doi.org/10.1016/j.addma.2022.102728.
[49] R.C. Hurley, Y. Tian, M.M. Thakur, J.-S. Park, P. Kenesei, H. Sharma, A. Gupta, K. Lee, Crystallographic texture, structure, and stress transmission in nugget sandstone examined with X-ray tomography and diffraction microscopy, *J Geophys Res – Sol Ea* 130 (2025) e2025JB031690. https://doi.org/10.1029/2025JB031690.
[50] Microstructure and Toughness, in: Fracture of Brittle Solids, 2nd ed., Cambridge University Press, 1993: pp. 194–248. https://doi.org/10.1017/CBO9780511623127.
[51] A. Hoenig, Near-tip behavior of a crack in a plane anisotropic elastic body, *Eng Fract Mech* 16 (1982) 393–403. https://doi.org/10.1016/0013-7944(82)90117-5.
[52] H. Laubie, F.-J. Ulm, Irwin′s conjecture: Crack shape adaptability in transversely isotropic solids, *J Mech Phys Solids* 68 (2014) 1–13. https://doi.org/10.1016/j.jmps.2014.03.004.
[53] L. Banks-Sills, I. Hershkovitz, P.A. Wawrzynek, R. Eliasi, A.R. Ingraffea, Methods for calculating stress intensity factors in anisotropic materials: Part I—z = 0 is a symmetric plane, *Eng Fract Mech* 72 (2005) 2328–2358. https://doi.org/10.1016/j.engfracmech.2004.12.007.
[54] T.-T. Nguyen, J. Réthoré, J. Yvonnet, M.-C. Baietto, Multi-phase-field modeling of anisotropic crack propagation for polycrystalline materials, *Comput Mech* 60 (2017) 289–314. https://doi.org/10.1007/s00466-017-1409-0.
[55] K.T. Faber, A.G. Evans, Crack deflection processes—I. Theory, *Acta Metall* 31 (1983) 565–576. https://doi.org/10.1016/0001-6160(83)90046-9.
[56] K.T. Faber, A.G. Evans, Crack deflection processes—II. Experiment, *Acta Metall* 31 (1983) 577–584. https://doi.org/10.1016/0001-6160(83)90047-0.
[57] F.C. Serbena, I. Mathias, C.E. Foerster, E.D. Zanotto, Crystallization toughening of a model glass-ceramic, *Acta Mater* 86 (2015) 216–228. https://doi.org/10.1016/j.actamat.2014.12.007.
[58] D.G. Wildgoose, A. Johnson, R.B. Winstanley, Glass/ceramic/refractory techniques, their development and introduction into dentistry: a historical literature review, *J Prosthet Dent* 91 (2004) 136–143. https://doi.org/10.1016/j.prosdent.2003.11.009.
[59] Q. Fu, G.H. Beall, C.M. Smith, J.T. Kohli, R.E. Youngman, B.R. Wheaton, A.J. Credle, O. Gulbiten, Strong, tough glass-ceramics for emerging markets, *Int J Appl Glass Sci* 7 (2016) 486–491. https://doi.org/10.1111/ijag.12247.

[60] B. Chen, J.N. Hu, Y.Q. Wang, S.Y. Zhang, S. Van Petegem, A.C.F. Cocks, D.J. Smith, P.E.J. Flewitt, Role of the misfit stress between grains in the Bauschinger effect for a polycrystalline material, *Acta Mater* 85 (2015) 229–242. https://doi.org/10.1016/j.actamat.2014.11.021.
[61] M. Kamaya, Y. Kawamura, T. Kitamura, Three-dimensional local stress analysis on grain boundaries in polycrystalline material, *Int J Solids Struct* 44 (2007) 3267–3277. https://doi.org/10.1016/j.ijsolstr.2006.09.020.
[62] N. Hansen, X. Huang, Microstructure and flow stress of polycrystals and single crystals, *Acta Mater* 46 (1998) 1827–1836. https://doi.org/10.1016/S1359-6454(97)00365-0.
[63] H.D. Espinosa, P.D. Zavattieri, A grain level model for the study of failure initiation and evolution in polycrystalline brittle materials. Part I: Theory and numerical implementation, *Mech Mater* 35 (2003) 333–364. https://doi.org/10.1016/S0167-6636(02)00285-5.
[64] T. Watanabe, S. Tsurekawa, Toughening of brittle materials by grain boundary engineering, *Mat Sci Eng A* 387–389 (2004) 447–455. https://doi.org/10.1016/j.msea.2004.01.140.

Chapter 3

BREAKING INTO PIECES: IN-SITU FRACTURE EXPERIMENTS PERFORMED ON A GLASS-CERAMIC

Sections of this chapter will be published in a forthcoming publication: **Gorske, S.F.**, Shanks, K., Voorhees, P., Faber, K.T. "3D brittle crack paths in an alkali-aluminosilicate glass-ceramic visualized in-situ using synchrotron X-rays and stable fracture geometry." In preparation.

3.1 Introduction

Glass-ceramics are an ideal class of materials on which to test the proposed experimental setup. The isotropic matrix, usually a silicate or aluminosilicate, resembles the previous DCDC tests on glasses and idealized models, while the presence of second-phase crystals can disrupt the strict Mode I crack of the ideal sample by introducing residual stresses and anisotropic lattices that can serve to deflect, attract, or arrest the crack's motion [1].

Glass-ceramics have found increasing use in applications requiring materials with greater strength and fracture toughness than typical glasses. For many glass-ceramics, the second-phase particles, which have different elastic moduli and fracture toughnesses than the surrounding matrix, create residual stress fields within the isotropic matrix as a result of thermal mismatch between the two phases. The first processing step is to bring the material past its melting temperature, then to cool it to and hold it at a temperature below the melting point but much higher than that which it is used at. Here, nucleation of the second phase particles is induced, and those particles grow through Ostwald ripening [2]. At temperatures under the liquidus but greater than the glass transition temperature, the material that will become the matrix is still soft, allowing the particles to grow without the hindrance of existing interfaces. Upon cooling, however, the difference in thermal expansion parameters between the matrix and the grains results in residual stress being distributed within the grains and the matrix [3–6].

Many second-phase crystals have larger thermal expansion coefficients than a typical glass, so if the matrix did not contain grains but rather empty cavities, those spaces would

not shrink as fast as isolated trevorite crystals. In order for the grains to remain bonded to the matrix, tensile stress needs to develop within the grains, while the matrix experiences tensile radial stresses and compressive tangential stresses. As a result, when a crack grows into the volume surrounding a particle, it will be deflected away from the particles, serving as an effective toughening mechanism [3,5]. In contrast, a crystalline phase with a lower thermal expansion coefficient than the matrix has less resistance to cracking and will attract the crack. Additionally, factors such as particle shape [5], density [1], and size [7] affect the overall toughening effect, all of which may be tuned through careful selection of precursor materials, which usually are a number of different oxide minerals [2].

Such crack deflections and reorientations are of interest to modelers of real materials. Many materials are composites and include particles, fibers, or other second-phase materials, and both composites and single-phase materials often have interior flaws which impact performance, and reliability. Understanding the paths cracks take between, around, and through particles, the locations of fastest and slowest growth, where the crack first appears, and any places where the crack might stop propagating, all under real loading conditions, will help modelers and developers of brittle materials to improve the understanding and implementation of materials for real-world applications.

For this first set of experiments, a system with a few measurable properties influencing crack growth was sought, both in order to reduce the number of variables that must be accounted for when creating a model, and to ensure the DCDC geometry would produce cracks as expected. Thus, a glass-ceramic with a cubic phase was chosen to minimize anisotropy and high aspect ratios in the crystals, with a goal to achieve equiaxed particles with minimum 10 μm diameter so they could be resolved in all directions using μ-CT. A system developed by the Pacific Northwest National Laboratory (PNNL) to mimic high-level waste satisfied these conditions, with cubic particles of trevorite, $NiFe_2O_4$, space group 227, in the spinel system, suspended in an alkali-aluminosilicate glassy matrix [8]. The system will be henceforth termed the trevorite glass-ceramic (TGC) in this thesis.

3.2 Materials and Methods

3.2.1 Materials

The heat-treated glassy precursors to the TGC were obtained from PNNL, including samples of Ni-1.5 and OL-02 oxide mixtures as described by Lonergan, et al. [8]. Shards of the glass mixtures in a ratio of 7 parts Ni-1.5 to 1 part OL-02 were mixed together, resulting in a material containing thirty different precursor oxides. Oxides present in greater than 1 wt% were: SiO_2 (39.69%), Na_2O (17.25%), Fe_2O_3 (14.90%), Al_2O_3 (8.45%), B_2O_3 (7.68%), ZrO_2 (3.90%), Li_2O (2.21%), NiO (1.32%), and MnO (1.07%), which together made up 96.47% of the material's weight. The shards were then placed in a 10 mL platinum crucible inside a CM Rapid Temp box furnace. The furnace was taken up to 1200 °C and held for 24 h, then lowered to 900 °C and held for 44 h before quenching to room temperature. Both temperature ramps were performed at a rate of 10 °C/min. The TGC was then removed from the crucible and examined for average grain size using optical microscopy. The grains generally had polyhedral shapes with defined facets (Figure 3.1a).

The visible grain areas were extracted by thresholding the images and analyzing the resultant particles with ImageJ, and the diameters were calculated with a square basis as an assumption. To verify that the grains were large enough for good-quality FF-HEDM and μ-CT data, for which a 10 μm diameter was the goal, an estimate for the average diameter was calculated based on Cuzzi and Olson's work [9]; while the equations used were designed for spheres, the grains present generally appeared to be equiaxed and thus were deemed acceptable to use. When using an estimate for monodispersed grains, the estimated diameter was 20.3 μm, while when using Cuzzi and Olson's inverted histogram method, which is weighted less by the large grains presenting with diameters of around 40 μm, the estimated average diameter was 14.2 μm.

The TGC samples were cut using a Buehler Isomet 5000 saw into dimensions of approximately 1.4 mm x 1.4 mm x 14 mm, within a tolerance of 0.03 mm. The bars were lightly polished on a Buehler Ecomet 3 polisher using 1200-grit silicon carbide paper to remove any irregularities from the saw, and the edges on the short faces, which would come into contact with the platens, were chamfered to remove any burrs on the corners. The hole for the DCDC geometry was then lasered into two of the opposing long faces for each sample

until the holes from both sides connected. The inner diameter of the intersecting cones was around 85 μm in diameter while the outer diameter on the sample faces was about 430 μm for an average hole diameter of around 250 μm.

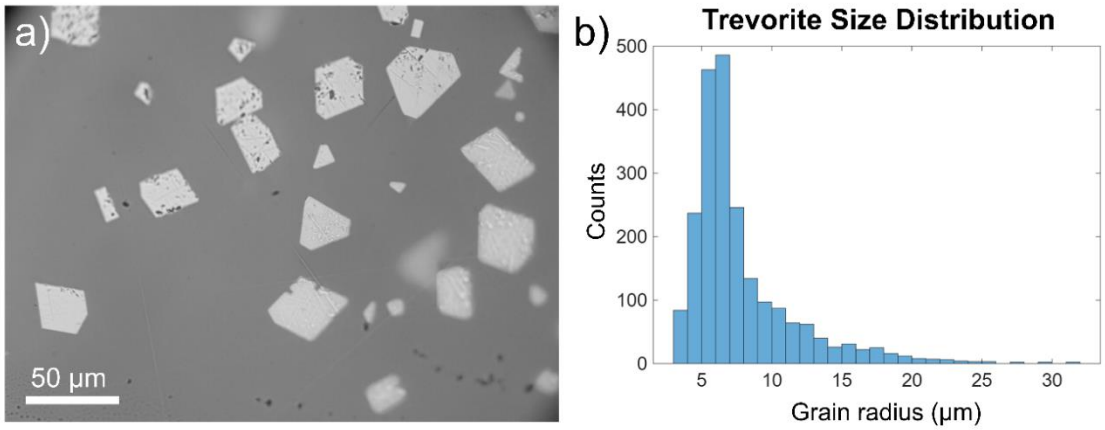

Figure 3.1: a) Optical micrograph of the polished trevorite glass-ceramic (TGC), showing faceted trevorite grains. b) Histogram of trevorite radii, as obtained from μ-CT, with mean 7.84 ± 3.83 μm.

3.2.2 Methods

Synchrotron experiments were performed at the Cornell High Energy Synchrotron Source at the ID3A Forming and Shaping Technology (FAST) beamline. A silicon (111) double-crystal monochromator was used to isolate 23.22 keV X-rays, with bandwidth $\Delta E/E = 0.002$, from the upstream undulator beam.

3.2.2.1 Loading

Compression testing was performed using the second-generation Rotational and Axial Motion System (RAMS2) [10]. The samples were loaded and centered in between hardened steel platens with 3 mm radius. Each sample's verticality was checked using live radiography and adjusted until it did not tilt in any direction. The entirety of the sample was able to be viewed by moving the load frame, allowing both the top and bottom cracks to be analyzed.

Loading was performed using displacement control. The loading direction was in the positive y direction when moving downward, such that the top of the sample was located at

more negative values of y. The load cell was lowered in manual steps of fractions of a micron while watching a live radiograph of the current location of the crack front. When extension was noticed, the load cell was moved away until the load on the sample had decreased by about 50 N. The displacement at that point was recorded and held during the following rotations and scans.

3.2.2.2 FF-HEDM

The FF-HEDM data were collected on two Dexela 2923 detectors located 0.576 m downstream of the sample. The detector distances and tilts were initially calibrated using an amorphous ceria sample, followed by a finer calibration using a polycrystalline ruby sample consisting of three strain-free grains of known orientation and location.

The beam size was set to a height of 25 μm and a width of 2.25 mm. A single 0.203 mm aluminum attenuator was inserted before the beam reached the sample to minimize detector pixel saturation. For each scan, 1440 frames were collected over a rotation from ω=0°-360° with an acquisition time of 0.25 s and a rotation step size $\Delta\omega$ of 0.25°. Scans were spaced 25 μm apart in the loading direction y.

Reconstruction of the results was performed using the HEXRD framework [11,12]. During initial reconstruction, summing all frames over 2θ produced a diffraction intensity pattern with strong peaks matching the expected material trevorite, with a strained average lattice parameter of 8.38 Å. An unstrained lattice parameter of 8.36 Å was used to calculate strain, following calculations presented in Section 3.3.1. Signals from the {111}, {220}, {311}, {222}, {400}, {422}, {333}, {511}, and {440} peaks were present with sufficient intensity to be used for reconstruction. Diffraction spots corresponding to rings in 2θ for the orientations {220}, {222}, and {400} were used for seeding of grain orientations. After initial reconstruction, grains with a goodness-of-fit parameter $\chi^2 < 0.001$ and a completeness > 0.8 were retained for further analysis.

Stress tensors were calculated from the strain tensors using the single-crystal elastic components of the stiffness tensor: C_{11} = 273.1 GPa, C_{12} = 160.7 GPa, C_{44} = 82.3 GPa [13].

3.2.2.3 μ-CT

μ-CT images were collected on a scintillator-coupled Retiga 4000DC detector, located 20.9 μm away from the sample, where the phase contrast was maximized. The beam size was set to a height of 1 mm and a width of 2.25 mm. A total of 720 images over a rotation angle of ω=0°-180° were acquired for each scan, with a rotation angle step size $\Delta\omega$ of 0.25° and an acquisition time of 1 s per image. Scans were spaced 0.8 mm apart in the loading direction *y*.

Reconstruction was performed using the CHESS Analysis Pipeline (CHAP) tomography package [14]. The final reconstructed data had voxel sizes of 1.48 x 1.48 x 1.48 μm3 and the locations in real space were recorded for registration.

3.2.2.3.1 Image Processing for Crack Detection

The crack measured only a few μm, and therefore only a few 2D pixels, in width at its maximum, and narrowed further the deeper it extended into the sample (Figure 3.2a,b). Eventually, it became narrower than the tomographic resolution, but the phase change at the interface still resulted in a change in X-ray absorption and was detected as a narrow, bright region due to fringing at the surfaces (Figure 3.2c). The narrowness of the crack meant that it could be difficult to distinguish from background noise in many regions (Figure 3.2b,c), and a custom image processing method was constructed to locate and measure the crack.

First, reconstruction artifacts, which presented as vertical lines, were removed by opening the image with a tall rectangular structural element, then the opened image was subtracted from the original in a top hat procedure (Figure 3.2d). Next, the trevorite grains were identified by thresholding the image; grains had intensities greater than 14% of the maximum image intensity (Figure 3.2e).

A modified median filter was then applied. First, the grain locations were replaced with random noise in the full image so the true background could be smoothed without interference from the bright grains. Opened and dilated versions of the images were created using a 3x3x3 cubic structural element and averaged to remove both dark and bright noise. Most of the denoised image, excepting the regions around the hole and the crack, was then treated with a 11x11x5 median filter to further smooth the matrix background. In the region

of the crack, defined as all those voxels directly above or below the hole, three types of voxel were identified: background, dark crack (wider), and bright crack (narrow). All voxels were characterized by their mean value in a 1x1x5 volume centered around the voxel of interest to strengthen the crack signal, which persists in subsequent slices, as well as their median values in 5x5x5 and 7x7x5 centered volumes. As the volumes increase in size around a crack point, both the number of background voxels and crack voxels should increase, but the former will increase faster; thus increasing thresholds (5.6%, 5.6%, 6.3% of the maximum intensity, respectively) were set for each volume that a point had to meet to qualify as a crack point. In contrast, a true background voxel might be below the threshold, and a larger volume will also increase the median value at that point, but fewer true crack points will be included since that data point will be more isolated compared to a group of crack points close to one another. Thus one threshold might be met, but the median values of the larger volumes near the average value of the background increase faster than in a volume including many crack points. The bright regions of the crack were identified similarly, although voxels and regions needed to be above the thresholds (7.7%, 7.7%, 7.0% of the maximum intensity, respectively) rather than below. Identified dark crack points were then set to the mean value of the 1x1x5 volume, decreased in intensity by 25%; bright points were similarly replaced then increased in intensity by 20%. All other points were set to the median value of a centered 11x11x5 volume to smooth out noisy signals. The previously suppressed grains were then added back in. Contrast was then enhanced for the top and bottom 1% of pixel values and normalized over the entire stack (Figure 3.2f).

Still, some noisiness remained after this pass. To remove it, the 2D binary images representing the potential locations of the crack were divided into their connected components. Shape filtering was applied to the binary images, first requiring the retained components to have a certain size. Additionally a certain amount of non-sphericity was required, as the crack was roughly linear, while small clusters of noise were more isolated and therefore spherical. A final requirement was for the long axis of the elliptical shape containing the component to be directed along an angle within some bound of the average crack orientation; the bounding value decreased as the crack progressed deeper into the sample and became more linear [15,16]. Finally, a stack of 100 slices was summed along the

direction of crack growth *y*, revealing the crack shape more fully, and for each image, pixels recorded as belonging to the crack in more than 12.5% of the other images were retained (Figure 3.2g,h). The points closest to the edges of the sample for each depth were then recorded to trace the outline of the crack front, since in the sample interior, the detected crack was often broken up into small sections due to proximity to grains that it jumped over, through, or around, leading to an inconsistent front appearance. Any points belonging to a slice with fewer than 100 total hits (0.005% area) were not included in the crack front trace due to remaining noise becoming stronger than the crack signal such that the true edges were difficult to discern. The crack edge points from the last five slices on either side were then used to connect a parabolic estimate for the crack front, which was expected to be curved [17]; the deepest point was then used as the value for crack length. Positive error was calculated as the difference between the parabolic depth and the deepest slice initially found, including those with fewer than 100 hits and averaged 52 μm. Negative error was the difference between the parabolic depth and the final confident edge point and averaged 15 μm.

3.2.2.3.2 Image Processing for Grain Analysis

The thresholded, binary images of the grains were retained after they were extracted from the structurally-filtered tomography images. A watershed algorithm was applied to separate grains which were clustered together after thresholding. ImageJ's 3D object counter was used on a sample volume under no load to better estimate grain sizes; after filtering out identified objects with a volume below 25 voxels^3 (radius of less than 3 μm), the average grain radius was found to be 7.84 ± 3.83 μm, in line with the original calculated diameter of 14-20 μm (Figure 3.1b). The number density of grains present was about 15,000 grains/mm^3, with a volume density of 4.1%.

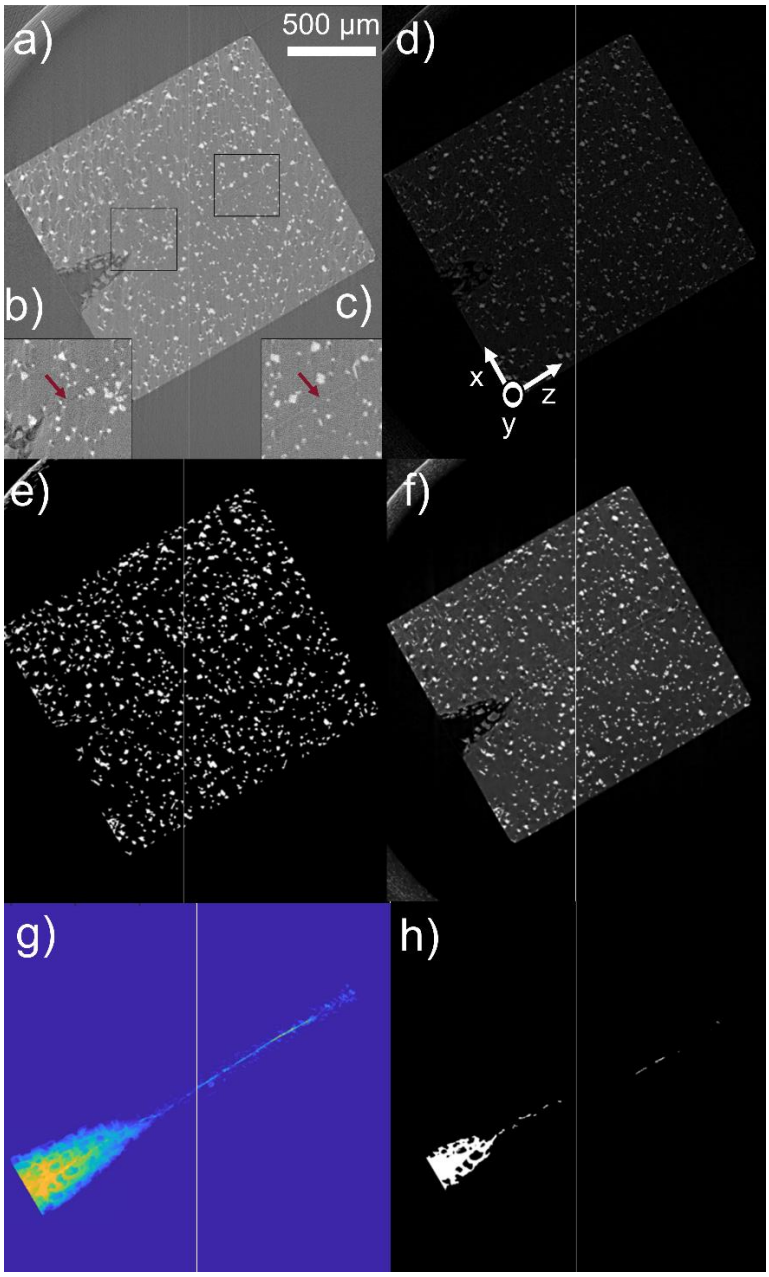

Figure 3.2: Steps in the image processing framework used to find the crack, on two sample locations, close to the hole and far. a) Reconstructed tomography slices showing b) the visible crack (dark line indicated by maroon arrow) and c) the crack when it was narrower than the tomographic resolution (bright line indicated by maroon arrow). d) Top hat image after opening with a rectangular structural element. e) Thresholded grains. f) Modified 3D median filter. g) Heat map showing relative frequency a location was marked as a crack point over 100 subsequent slices. h) Final crack points.

3.3 Results and Discussion

3.3.1 Tomography

3.3.1.1 Crack Extension

Initial pop-in of the crack was observed on both sides of the TGC sample at -498 N (Figure 3.3a). The top crack pop-in length was 0.691 mm, while the bottom side had a length of 0.655 mm. The bottom crack then extended further to 0.916 mm at a load of -523 N, while the top crack did not extend. Both sides then extended at -624 N, to 1.06 mm on the bottom and 1.02 mm on the top (Figure 3.3b). A final extension was observed at -690 N. The top of the crack extended to 1.45 mm and the bottom crack was initially estimated to extend to around 1.6 mm, but further extension occurred during the tomography scan, despite the load having been lowered to -650 N. While the bottom crack did narrow around the expected depth, it widened again a few tens of microns deeper and was detected to a depth of 2.11 mm (Figure 3.3c). Incidentally, tomography analysis revealed that during the scan, starting at around a depth of 1.6 mm and continuing to the bottom of the sample, part of one sample side had sheared off, reducing the local load-bearing area and increasing the local applied stress, which may have contributed to the crack's resumed growth. The sheared-off shard was not flat; while it was not found afterward, the remaining sample continued to taper inward toward the bottom face, causing the reduction in area to increase with sample depth, and therefore also increasing the applied load with depth. Immediately after the tomography scan at that load, the sample failed fully, which likely indicates that the bottom crack had reached an unstable point after the shearing event, as in some volume, the load distributed over the shrunken area would have exceeded that necessary to propagate the crack fully through the sample.

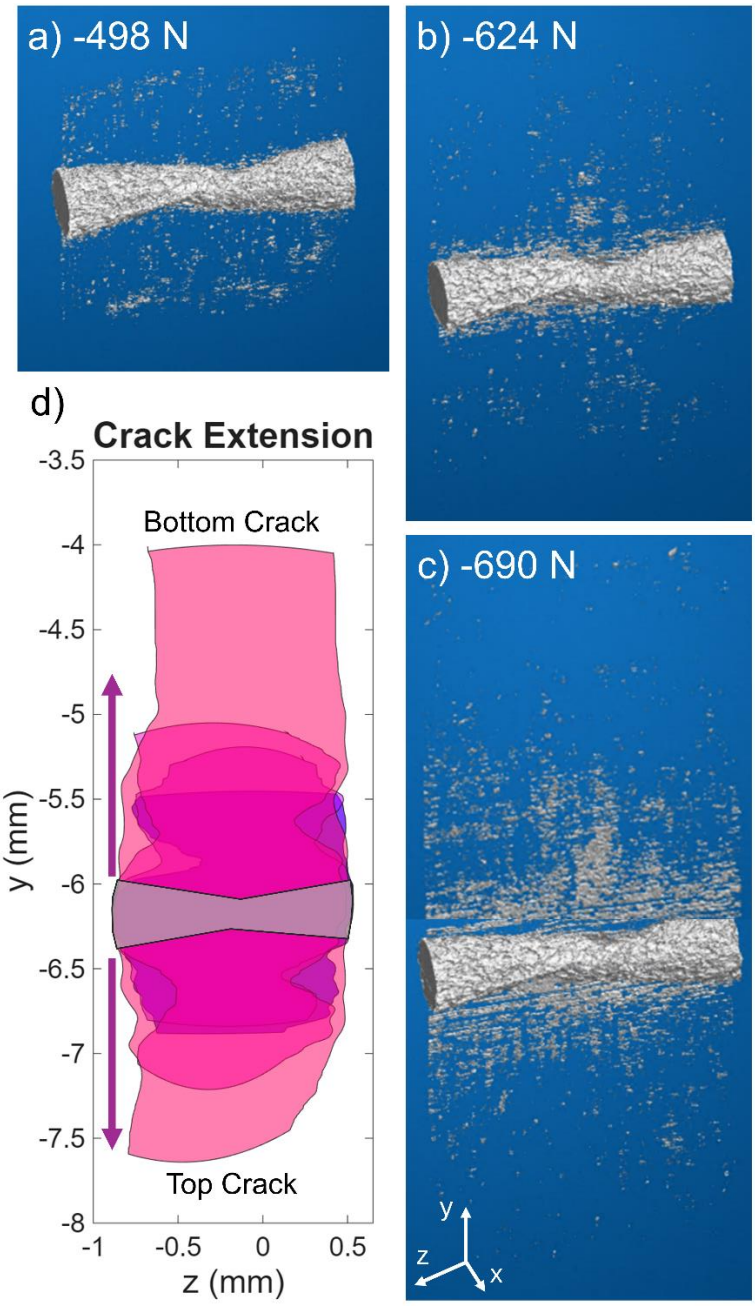

Figure 3.3: Crack extension in the TGC sample. a) Initial pop-in observed at -498 N. b) A regular extension event at -624 N. c) At -690 N, the top crack (more negative *y*) extended normally, while the bottom crack appeared to extend normally but underwent a secondary extension event and was eventually detected again deeper in the sample. d) All crack extensions overlaid, with darker colors corresponding to earlier extension events. The frame orientation is labeled in the bottom of c).

3.3.1.2 Fracture toughness

Using Equation 2.5 [18] with the load at extension and calculated crack lengths, the fracture toughness K_{Ic} can be calculated for all extensions for both the top and bottom cracks (Figure 3.4). Most values fall between 1.4 and 1.6 MPa$\sqrt{m}$. This range is similar to the fracture toughnesses of many other glass-ceramics with silicate-based matrices and low crystalline volume fractions studied in other experimental modes [19-22]. Additionally, the fracture toughness is higher than a pure glass, as expected [22,23]. Promisingly, the fact that these values correspond indicates that the DCDC experiments are successfully capturing crack extension similar to that seen in other experiments. Thus, the cracks described here are not irrelevant to fracture in other geometries and models or simply academic in nature.

The highest recorded fracture toughness corresponds to the top crack at -523 N, at which load the bottom crack extended but the top did not, resulting in its length being the same as the previous calculation. The fracture toughness is not reported for the final extension in the bottom crack, as the initial extension length was not obtained before the secondary extension event, and the extension which was recorded occurred in a volume where the cross-sectional area changed with depth, meaning a single stress value is invalid.

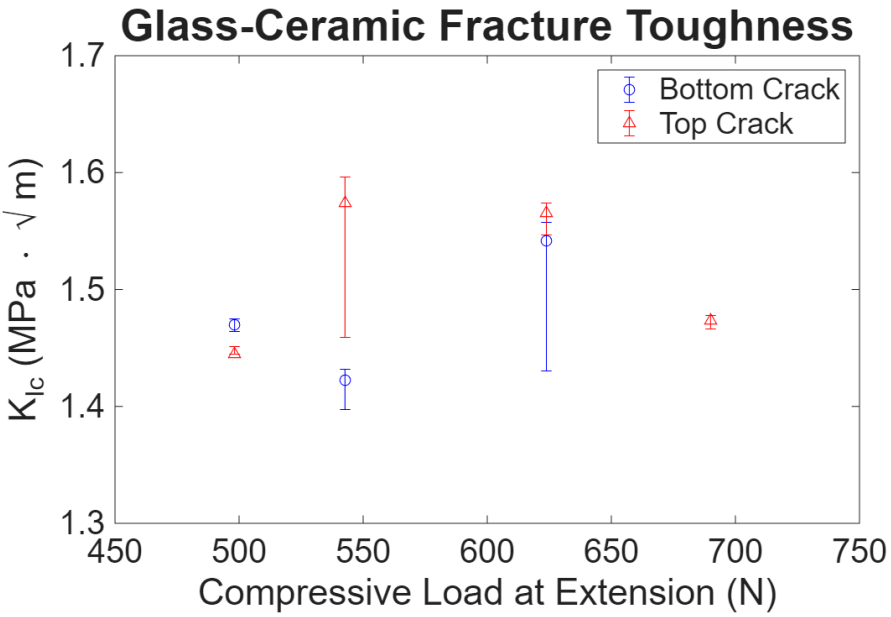

Figure 3.4: Fracture toughness in the DCDC TGC sample using Equation 2.5 [18].

3.3.2 Trevorite grain response

3.3.2.1 Stress response

Near-zero load analysis of the FF-HEDM results for the trevorite grains reveals a wide distribution of strains, and therefore stresses. Given the thermal history of the TGC sample and the mismatch in properties between the trevorite grains and the silicate matrix, residual stress is expected in the trevorite crystals, which have a larger thermal expansion coefficient than a typical glass.

The Selsing model (Equation 3.1) can be used to estimate residual stresses in a model glass ceramic system with evenly distributed, spherical, isotropic crystals in a volume fraction smaller than 10% [3,24]. While more idealized than the reality of the TGC system, the cubic, equiaxed nature of the grains allows this model to be used as an initial estimate for the residual stresses present in the TGC sample before loading.

$$\sigma_T = \frac{\Delta\alpha \cdot \Delta T}{(1+\nu_M)/2E_M + (1-2\nu_T)/E_T} \qquad \text{Equation 3.1}$$

$\Delta\alpha$ = difference in thermal expansion coefficients

ΔT = difference between glass transition temperature and room temperature

ν = Poisson's Ratio

E = elastic modulus

Average values for the elastic constants and the thermal expansion coefficient of trevorite can be obtained from geological studies [13], while the matrix properties can be estimated from average properties of alkali-alumino-silicate glasses [23,25]. The glass-transition temperature of the glassy phase can be estimated from the liquidus temperature [8] and a simplified relationship (T_g/T_l = 2/3) between the two [26]. All values are reported in Table 3.1.

Table 3.1: Estimated properties of trevorite and the silicate matrix for use in Equation 3.1.

	Matrix	Trevorite
Elastic modulus E	70 GPa	183 GPa
Poisson's ratio ν	0.25	0.33
Thermal expansion coefficient α	60×10^{-7} °C $^{-1}$	25.8×10^{-6} °C $^{-1}$
Glass-transition temperature T_g	—	780 °C

The resultant estimated residual stress in the trevorite particles is 1386 MPa. Since these particles are not pure trevorite but likely have many substitutions [27], and since they are

anisotropic, are not perfectly spherical, and have a range of sizes, the crystals had a spread in stress, especially as load was applied, and the average could also vary from this value. However, since the true value of the unstrained lattice parameter is unknown for this specific formulation, it has been set to a value of 8.36 Å, for which the average stress in the trevorite crystals across all of the *x*, *y*, and *z* directions was 1465 MPa and nearly all stresses in all directions were tensile in nature (Figure 3.5). This lattice parameter represents an increase of 0.25% from the nominal unstrained lattice parameter of 8.339 Å [13].

While the load in the matrix is unknown due to FF-HEDM not providing data on amorphous materials, the radial stress around glass-ceramic particles with residual stress is known to be related to the stress in the particles, dropping off as r^{-3} with distance from each particle [3].

The FF-HEDM results for the stress and strain in the trevorite crystals at the different loads for which data were collected are presented as raincloud plots in Figure 3.5. While the stresses in all directions had similar values at near-zero load, the stresses in the *y* direction decreased with applied load (Figure 3.5a-b), indicating they took on some of the overall compressive stress on the sample, while the stresses in *x* and *z* increased slightly in accordance with expected transverse stresses for samples under compressive load (Figure 3.5c-f). While most of the grains had values clustered around the averages in each direction, indicated by the width of the quartiles in the box plots and the shape of the histograms, there were a number of outliers both with greater and lesser magnitude in both stress and strain at all loads in all directions.

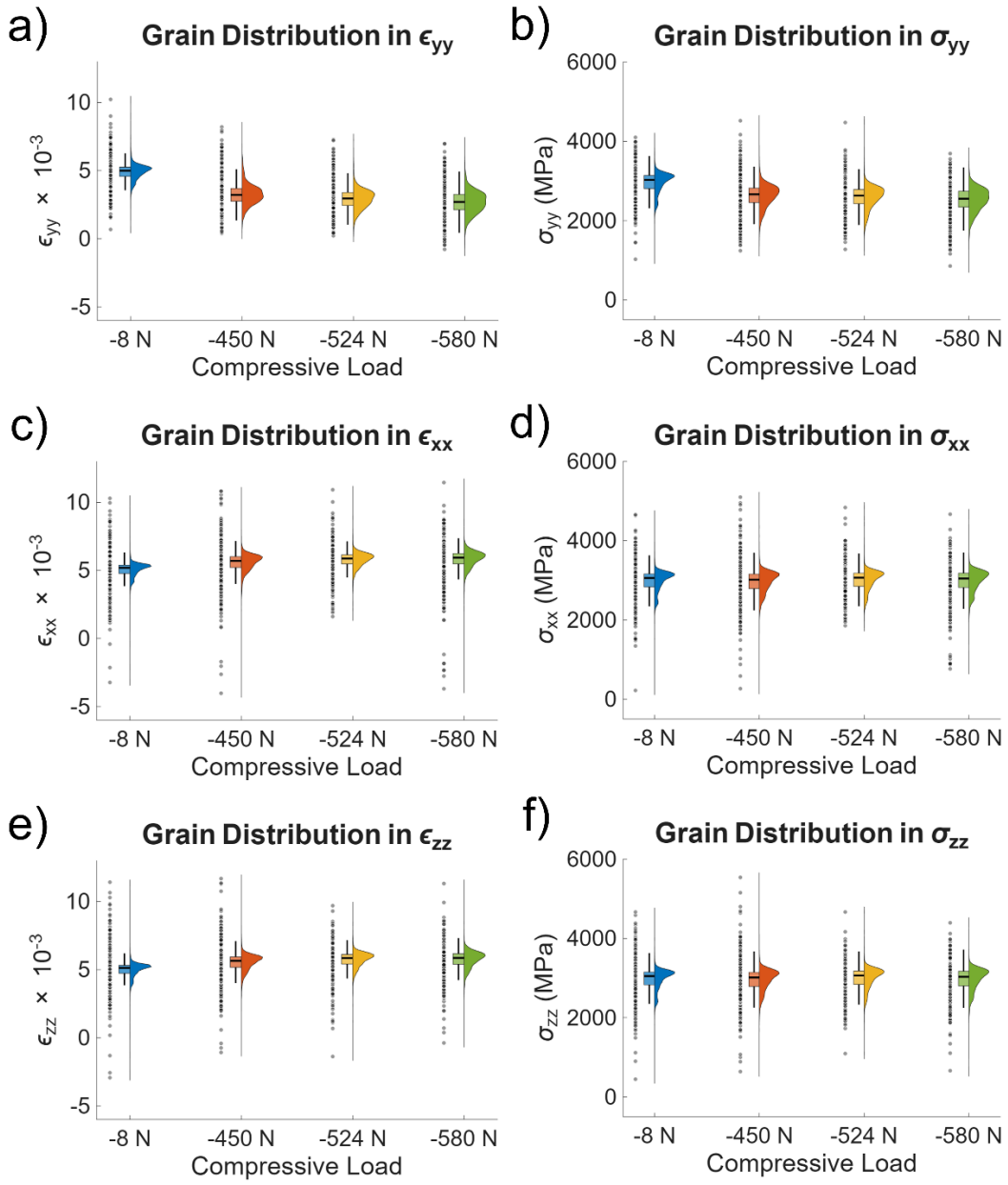

Figure 3.5: Strains and stresses in the trevorite crystals in the TGC sample, depicted as rainclouds plots. For each set of data collected, the data points are plotted on the left, a boxplot showing the quartiles and median value of each dataset is presented in the center, and a histogram is plotted on the right showing the relative frequencies of values. a-b) Strain and stress in the loading (*y*) direction, respectively, showing a decrease in average value with load. c-d) Strain and stress in the *x* direction, oriented perpendicular to the hole axis. e-f) Strain and stress in the *z* direction, oriented along the hole axis.

While the overall stresses are informative for demonstrating that the trevorite crystals, and not just the matrix, were impacted by the overall applied load on the sample, stress is additionally known to be impacted by the crack front, as a Mode I crack in the DCDC geometry has a tensile region ahead of the crack tip working to open it upon an increase in load. As the FF-HEDM scans were collected near the estimated crack front, the stresses at a given load can be subdivided into smaller volumes and analyzed. Figure 3.6 depicts the average stresses in each 0.25 mm-tall volume as a function of distance for the crack, for datasets collected at both the top and bottom crack front at two different loads. The grains near the crack, that is, directly above or below any part of the hole, are differentiated from those in the rest of the sample bulk.

For all datasets except for that of the top crack front at -450 N (Figure 3.6a-b), the stress values for grains near the crack plane were more tensile than those in the sample bulk in both the *x* and *y* directions until a distance of about 0.3 mm away from the crack tip, when the two populations coincided. Notably, the early top crack with the lowered stress values, after popping-in at -498 N, did not extend until a load of -624 N was reached, compared to the extension at -523 N experienced by the bottom crack (Figure 3.6d). Despite similar pop-in lengths, the increase in tensile stress as a result of the crack was suppressed for the top crack, with the populations ahead of and away from the crack having similar values, in contrast to the bottom half of the sample, where grains ahead of the crack experienced more tensile stress (Figure 3.6c-d). The average values for σ_{xx} and σ_{yy} for all grains in the top half of the sample at that load were also on average lower than those at similar distances from the crack in the bottom half of the sample, indicating a greater sample resistance to cracking in that region. When the top crack did extend, it moved about 0.3 mm further into the sample, stopping before a region with a large increase in σ_{yy} for both populations (Figure 3.6b) but a depression in σ_{xx} for the grains ahead of the crack (Figure 3.6a). While these trends may have changed somewhat at the higher load, the lowered tensile stress in that volume in the *x* direction indicates that higher loads were necessary to induce further tensile stress and to reach a sufficient crack-opening stress for propagation. As a result, the fracture toughness should be higher in that region than in the opposing crack.

At -580 N, the stresses in the crack plane were greater in magnitude than those in the sample bulk in both *x* and *y* at nearly all distances, indicating the effect of the crack tip on the region (Figure 3.6e-h). While both cracks extended during the next extension event, the bottom crack experienced the secondary extension discussed in Section 3.3.1.1 and grew to a greater length. Similarly to the grains at -450 N, the stresses in both *x* and *y* for the crack which grew longer (Figure 3.6g-h) were higher on average than those near the crack which grew to a shorter length (Figure 3.6e-f), again indicating a reduction in resistance to the crack for regions with higher tensile stresses, where less applied load was required to exceed the stresses required for crack extension, decreasing fracture toughness.

The difference in local average stresses and fracture toughness could be a result of several different factors. During quenching, the sample cooled faster in some regions than in others, likely causing a difference in residual stress, and therefore in the stress field encountered by the crack. Additionally, due to the number of oxides present in the initial melt which can substitute into the trevorite lattice, and the potential for uneven distribution of ions, the lattice parameter for each grain might vary, resulting in a different actual strain on the lattice than reported. Furthermore, while the grains are generally evenly distributed, there might be some volumes with a higher or lower average grain diameter, which also would affect the stress distribution.

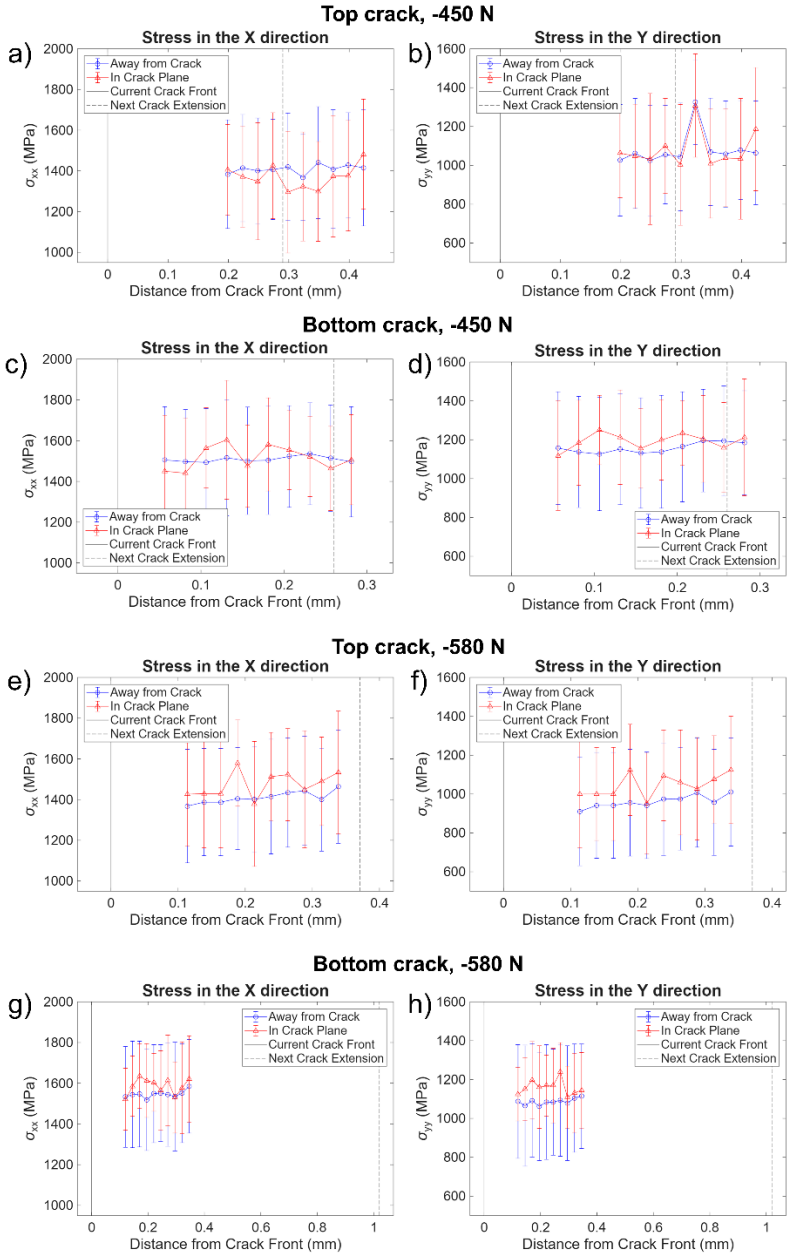

Figure 3.6: Stresses in the trevorite crystals with distance from the crack front, for both the top and bottom cracks at two different loading states. a-b) In the top crack at -450 N, which did not grow until -624 N, σ_{xx} and σ_{yy} for grains ahead of the crack are not larger than for grains away from the crack, and their values are depressed when compared to those in the bottom crack (c-d), which grew at -523 N. e-f) In the top crack at -580 N, the stresses are again on average lower than those on the bottom (g-h), which grew to a greater length in the next group of extension events.

3.3.2.2 Fracture response

For particles with a thermal expansion coefficient greater than that of the matrix, a growing crack will be deflected away from the particles rather than attracted to them [5,7]. Thus, the crack is expected to diverge away from the trevorite particles in the TGC system. This was indeed the case for most of the particles in the studied sample; however, certain particles were also cracked through in a transgranular manner, and others appeared to bridge the crack, at least partially. The three types of particle-crack interaction are shown in a tomography slice in Figure 3.7a, along with the same slice before the crack propagated (Figure 3.7b) to verify transgranularity. Grains which deflected the crack will be termed intergranular henceforth for ease of description and comparison, although this type of crack is really inter-granular-matrix rather than truly existing between two grains on a grain boundary.

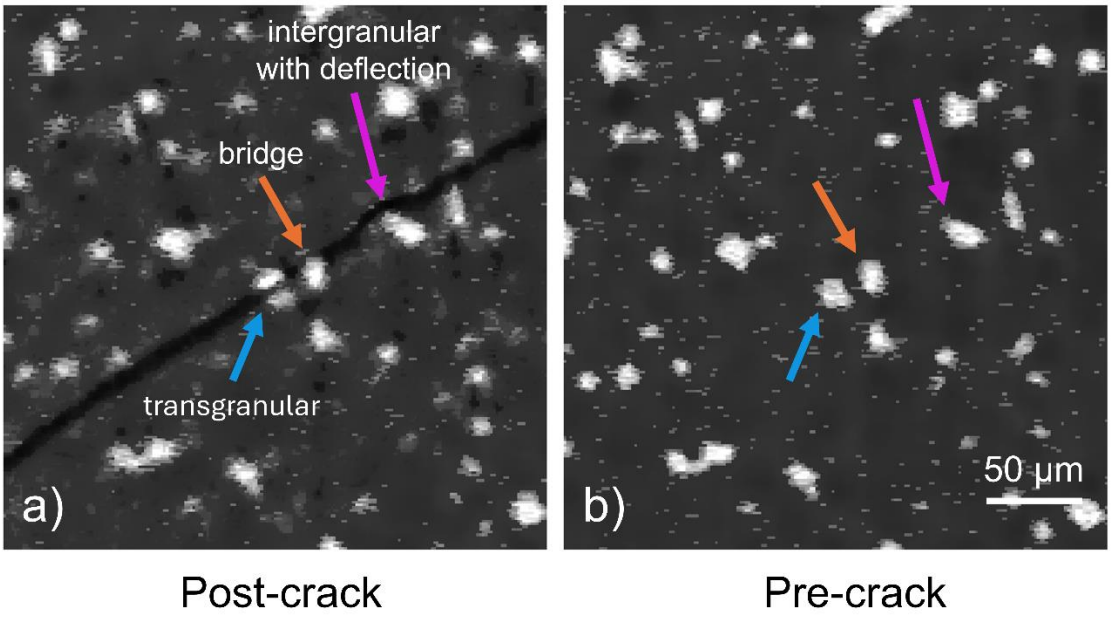

Figure 3.7: Types of grains which interacted with the crack. a) A tomographic slice showing transgranular grain, a grain which bridged the crack, and an intergranular grain, which the crack had to deflect to go around. b) The same slice from before the crack propagated, verifying that the transgranular grain was originally a single grain.

The different populations of grains can be examined to determine what factors led to them cracking in the manner that they did. Figure 3.8 shows FF-HEDM data for orientation and mechanical state collected at near-zero load for the grains in the 500-μm tall volume around the hole to examine whether any of these properties is predictive for whether the crack propagated through or around a grain.

Figure 3.8a shows the orientation of the grains projected along the *y*-direction, along which the crack propagated, and thus the planes perpendicular to it. The orientations for all grains in the volume are shown to emphasize the random nature of grain orientation. Intergranular, transgranular, and bridging grains are highlighted, with all the populations mixed. While the crack does seem not to have moved transgranularly through grains with a near-<100> normal, nor did grains with a near-<111> normal, grains which the crack was deflected around occupy orientations across the fundamental region, limiting those traits in being predictive factors for crack motion. Figure 3.8b then shows the orientation of lattice planes on which the crack moved transgranularly, or did not move, either by deflection or by bridging. Again, there is little trend for any one population to explain why a crack might move onto or avoid a particular plane; the absence of data points near the {100} directions belonging to any of the populations simply indicates a lack of encounters on that plane family, since it did not move to or avoid those planes.

Next, Figure 3.8c shows the granular strain, in the *x* (crack opening) and *y* (loading) directions, while Figure 3.8d displays stress in the same directions. The other grains in the region of the crack (above or below the hole) are also shown. Once again, the populations are mixed in with one another as well as the overall population, and the presence of outliers only serves to show that a particular value or ratio of values is not sufficient to predict the way a crack will grow as it nears a grain.

This makes sense, as from a purely theoretical standpoint, all the grains, regardless of orientation, should lead to crack deflection. Even though they did display a range of residual stresses at near-zero load, those stresses were still tensile in nature, indicating the assumptions made about their properties in comparison to the matrix are reasonable, and again, should lead to crack deflection. Thus, additional factors resulting from the

arrangement of grains in the sample, the grain or sample geometry, or other experimental conditions must be affecting the crack.

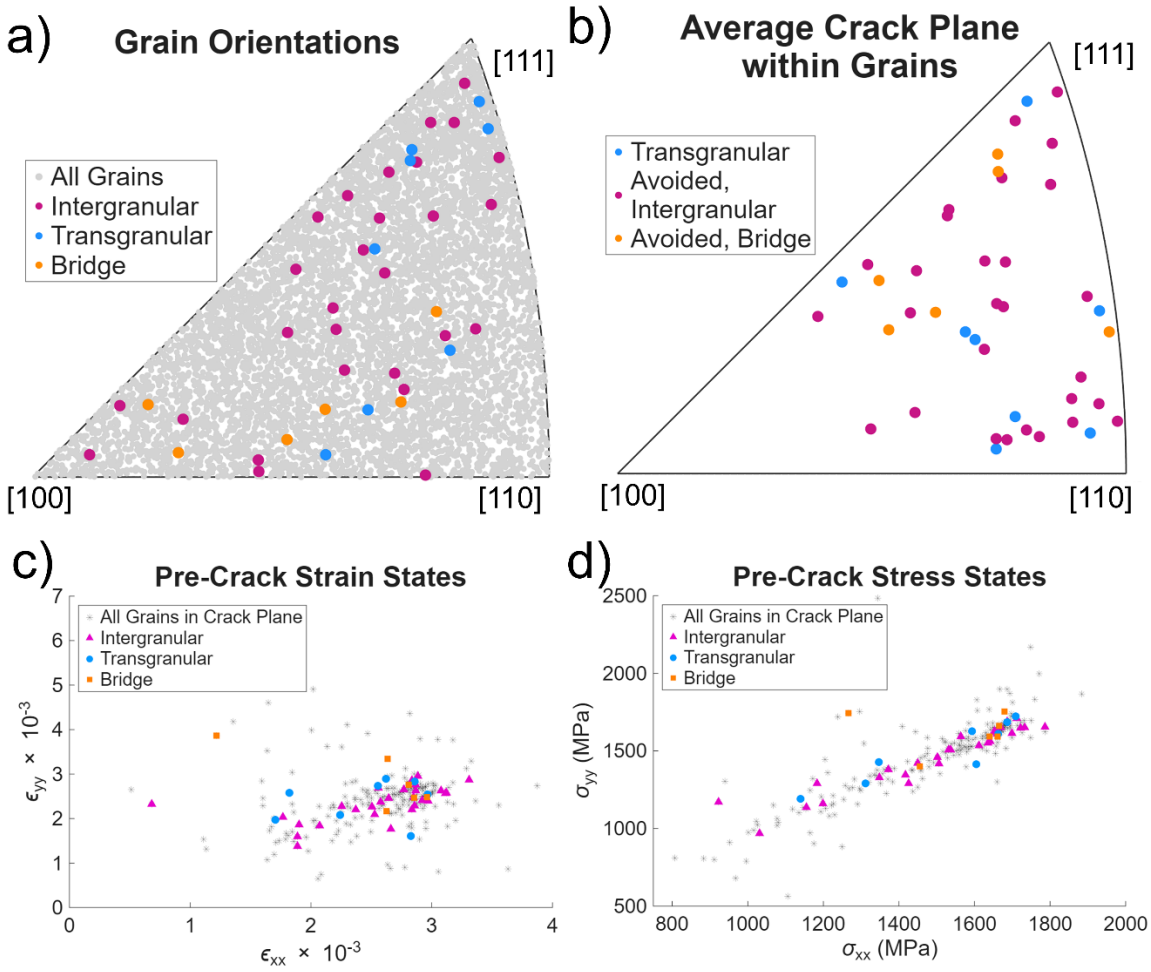

Figure 3.8: FF-HEDM data for intergranular, transgranular, and bridging grain populations at near-zero load. a) The orientation of the lattice planes perpendicular to the crack's direction of motion. While the transgranular and bridging grains show some trend, intergranular grains overlap with those values. b) The orientation of the lattice plane on which transgranular cracks moved, along with the orientation of the crack if it had not been deflected in intergranular grains or stopped by bridging grains. c-d) Strain and stress states, respectively, in the *x* (crack opening) and *y* (loading) directions, for grains of the three populations compared to all grains in the crack plane.

3.3.2.3 Crack deflection

In the absence of any predictive quality in the grains themselves, the relation between the crack and the grains is of potential use. Fracture toughness is related to the strain field, which itself is related to angle relative to the crack tip [5,28]. Thus, while a deflection may lead the crack to grow in a more favorable location than through a grain with high fracture toughness and residual stress, it can also be true that a deflection may be less favorable than the transgranular crack at certain angles. Figure 3.9a shows the angles of deflection for grains which did deflect the crack, as well as the theoretical angles at which it would have had to deflect to go around the grains it ultimately passed through transgranularly or which it bypassed entirely, leading to a bridge. The method of angle calculation was to average the absolute values of the deflection angle at the grain's maximum cross-section to the nearby straight section of the crack. Figure 3.9b reproduces the tomography slices of Figure 3.7a with angles labeled. The transgranular and bridging grain are at their maximum cross sectional area, while the intergranular grain is not; at its maximum area, its facets coincided with the labeled angles. From Figure 3.9a, the crack moves intergranularly when the angle of deflection, averaged from the absolute values on either side of the grain, is less than about 0.45 radians, or 25.8°. Required deflections greater than that value are avoided, with the crack moving straight through the impinging grain instead. Greater deflections usually coincide with larger grains, which more regularly cross over the central crack plane (Figure 3.9c), but are also dependent on the centroids being close to the average crack plane, such that large grains located about one radius away from the crack plane can still crack intergranularly. Figure 3.9c also shows that the angle of deflection is not dependent on grain orientation; instead, it is mainly impacted by the grain geometry.

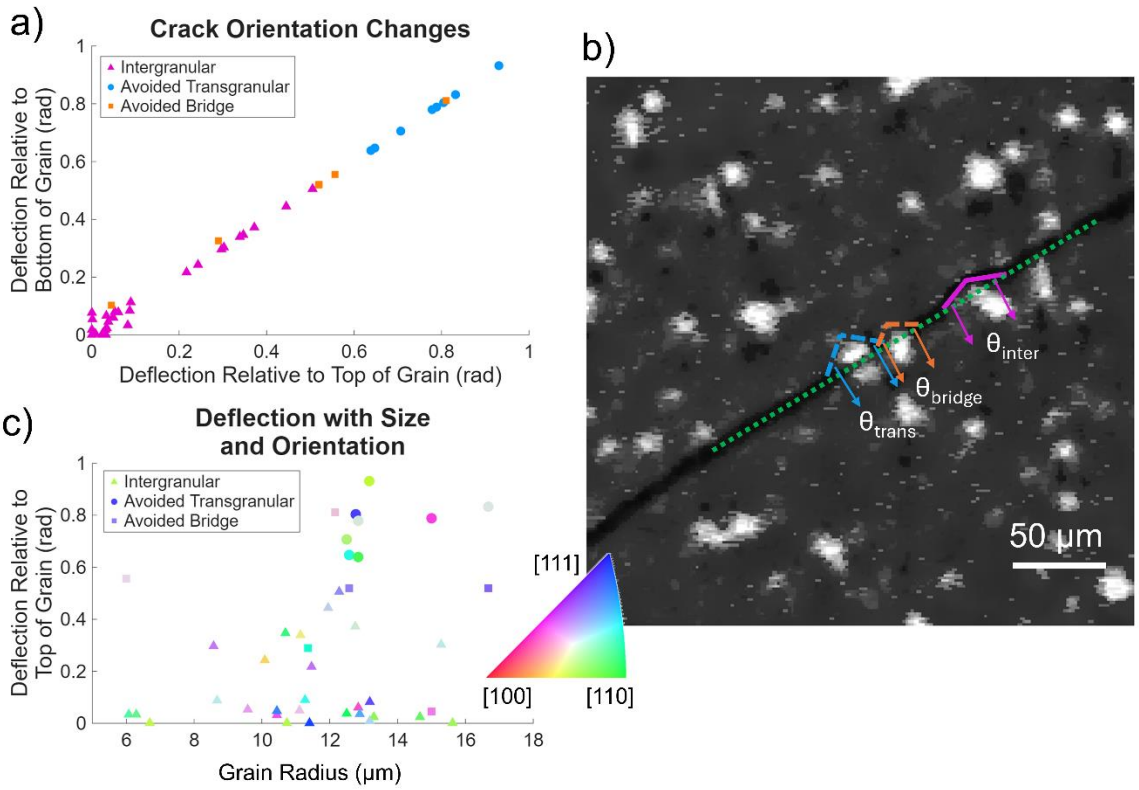

Figure 3.9: Crack deflection and grain type. a) Intergranular grains deflect the crack up to a maximum of 0.45 radians, while the crack would have to theoretically deflect at larger angles to go around grains which eventually cracked transgranularly or acted as bridges. b) The tomographic slice of Figure 3.7a reproduces with deflection angles labeled. c) Deflection angle as a function of grain radius and colored by the orientation of Figure 3.8a in standard inverse pole figure colors (inset).

A point of note in Figure 3.9a is that there are two grains which bridged the crack with angles smaller than 0.45 radians. Figure 3.10 shows these grains in detail, demonstrating that both have a high aspect ratio in contrast to the mostly equiaxed grains in the majority of the sample. Figure 3.10a-e shows the grain with the theoretical deflection of about 0.25 radians in successive slices spaced 3 μm apart, showing that the visible edge was oriented roughly parallel to the crack. The grain was tilted in the *y* direction, causing the cross-section to move across the crack plane with increasing depth. While the crack could move intergranularly around one side, the deflection to continue around it would increase as the cross-section

moved away from the crack plane. As a result, the crack actually moved intergranularly when one of the faces coincided with the crack plane (Figure 3.10a,e), but moved transgranularly in the center of the grain, with minimal deflection (Figure 3.10c). At intermediate stages, as the crack transitioned to transgranular and back, it bridged the crack (Figure 3.10b,d).

The other bridging grain, with a theoretical deflection of less than 0.1 radians, also had a high aspect ratio, but was oriented perpendicular to the crack plane (Figure 3.10f), acting like a reinforcing fiber working to hold the sample together, which has been observed in other glass-ceramics with high aspect ratio crystals, such as lithium disilicate-based glass-ceramics [29,30].

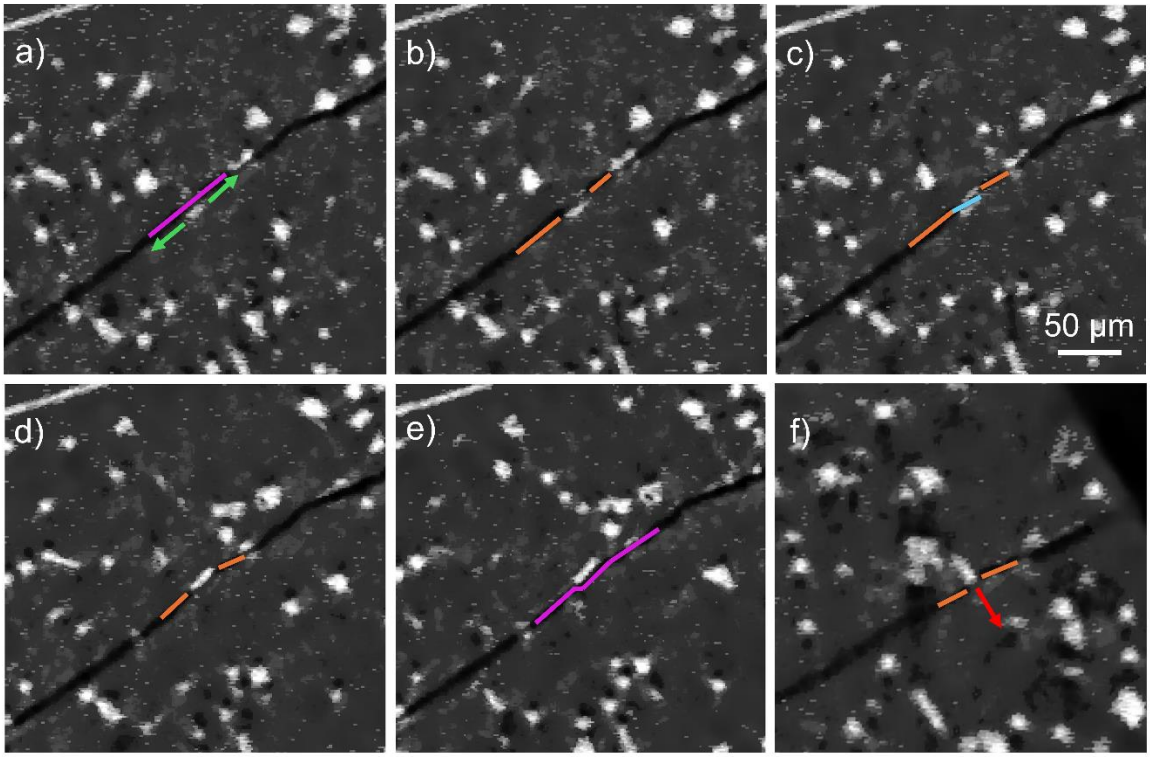

Figure 3.10: Two high aspect ratio grains bridging the crack in different ways. a-e) A grain oriented parallel to the crack plane, that transitions from intergranular cracking, through bridging, to transgranular cracking, and back again at different crack depths. f) A grain oriented perpendicular to the crack plane, acting as a reinforcing fiber.

Intergranularly-cracked grains with relatively large (>0.4 radians) deflection angles can also be considered. Notably, for one such grain, it is found to be directly opposite two different, smaller grains located at different depths, both of which have a smaller deflection angle (Figure 3.11b,c). The crack moves between these two grains in true intergranular fashion, with the smaller deflection around the two smaller grains serving as a favorable cracking location offsetting any potential hindrance by the larger deflection around the larger grain.

Figure 3.11 also demonstrates the tendency of the crack to remain straight in the absence of grains, a phenomenon seen in other materials primarily cracking in a Mode I fashion [16]. Figure 3.11a shows the crack 6 μm before the appearance of the top face of the large grain in Figure 3.11b,c), where it is nearly entirely straight. In Figure 3.11d, 6 μm deeper along the crack beyond the large grain's bottom face, the deflection has almost straightened out again, demonstrating its tendency to return to straight in the isotropic matrix, where there are no lattice planes on which for it to persist or facets around which it deflects.

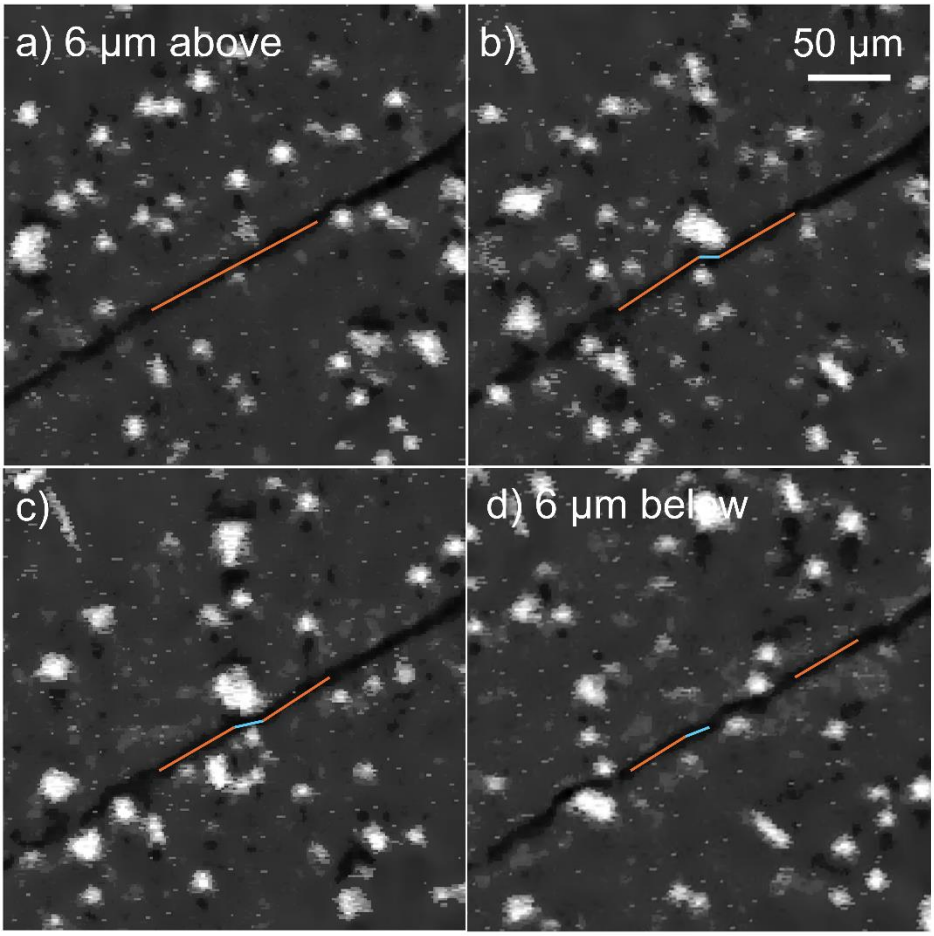

Figure 3.11: Crack deflection as a function of sample depth. a) Closer to the hole and 6 µm above the top edge of the large grain in b) and c), the crack is straight in the absence of local grains. b) The crack deflects between two grains. c) The large grain above the crack is the same as in b) while the smaller one below is a different grain located underneath the small grain in b), and the crack has continued to deflect. d) 6 µm below the bottom edge of the large grain in b) and c), the kink remaining from the deflection has almost straightened out.

3.4 Conclusion

The system of synchrotron X-ray HEDM and µ-CT is demonstrated to work admirably to reveal both the crack and the microstructure in the TGC sample. By combining the stable fracture of the DCDC geometry and the precise loading of RAMS-II, we were able to induce, grow, and pause cracks in the sample, allowing for investigation of the microstructure and

the crack shape at multiple loading iterations. General expectations for the glass-ceramic were met, with the higher thermal expansivity of the trevorite grains compared to the matrix creating residual stresses that tended to deflect the crack, but only at deflection angles smaller than 0.45 radians. As a result, crack bridging, especially by grains of high aspect ratio, and transgranular cracking were also observed, dependent largely on deflection angle. The number of observations of different types of cracking should serve as useful information for modelers seeking to verify their work and to incorporate multiple material responses into their models.

Additionally, stress variations in grains ahead of the crack were revealed using FF-HEDM. Two cracks in the same sample of about the same length may grow at different loads and to different lengths upon application of load based on the accumulation of local stresses, with higher tensile stresses ahead of the crack before propagation leading to a lowered fracture toughness as less load is needed to reach the critical point for crack extension.

Further investigation into glass-ceramics with non-cubic crystalline phases and higher aspect ratios would serve as a useful extension to this work and to future, more advanced models, especially with the results regarding crack bridging. In particular, lithium disilicate-based glass-ceramics are broadly used in many applications [1,2], making such results highly relevant, and the behavior of the lenticular crystalline phase would present a different set of insights to those presented here that could help elucidate key similarities and differences between different classes of glass-ceramics and dual-phase systems.

Acknowledgments

This work was sponsored by the US Office of Naval Research Grant No. N00014-21-1-2784. SFG was also supported by the US National Science Foundation Graduate Research Fellowship No. 2139433. Additionally, the authors would like to thank Dr. Paul Shade and the Air Force Research Laboratory for the generous use of RAMS2. This work is based on research conducted at the Center for High-Energy X-ray Sciences (CHEXS), which is supported by the National Science Foundation (BIO, ENG and MPS Directorates) under award DMR-2342336.

Bibliography

[1] Y. Jiang, C. Zhang, J. Xu, J. Xu, X.-Q. Zhan, N. Ma, F.-C. Tsai, An overview of dental glass–ceramics: From material design to the manufacturing process, *Int J Ceram Eng Sci* 6 (2024) e10224. https://doi.org/10.1002/ces2.10224.
[2] G.H. Beall, Design and properties of glass-ceramics, *Annu Rev Mater Sci* 22 (1992) 91–119. https://doi.org/10.1146/annurev.ms.22.080192.000515.
[3] F.C. Serbena, E.D. Zanotto, Internal residual stresses in glass-ceramics: A review, *J Non-Cryst Solids* 358 (2012) 975–984. https://doi.org/10.1016/j.jnoncrysol.2012.01.040.
[4] A.G. Evans, Microfracture from thermal expansion anisotropy—I. Single phase systems, *Acta Metall* 26 (1978) 1845–1853. https://doi.org/10.1016/0001-6160(78)90097-4.
[5] K.T. Faber, A.G. Evans, Crack deflection processes—I. Theory, *Acta Metall* 31 (1983) 565–576. https://doi.org/10.1016/0001-6160(83)90046-9.
[6] K.T. Faber, A.G. Evans, Crack deflection processes—II. Experiment, *Acta Metall* 31 (1983) 577–584. https://doi.org/10.1016/0001-6160(83)90047-0.
[7] R.W. Davidge, T.J. Green, The strength of two-phase ceramic/glass materials, *J Mater Sc*i 3 (1968) 629–634. https://doi.org/10.1007/BF00757910.
[8] C.E. Lonergan, J. Rice, C. Skidmore, M.J. Schweiger, P. Hrma, The effects of mixing multi-component HLW glasses on spinel crystal size, *J Nucl Mater* 558 (2022) 153318. https://doi.org/10.1016/j.jnucmat.2021.153318.
[9] J.N. Cuzzi, D.M. Olson, Recovering 3D particle size distributions from 2D sections, *Meteorit Planet Sci* 52 (2017) 532–545. https://doi.org/10.1111/maps.12812.
[10] P.A. Shade, B. Blank, J.C. Schuren, T.J. Turner, P. Kenesei, K. Goetze, R.M. Suter, J.V. Bernier, S.F. Li, J. Lind, U. Lienert, J. Almer, A rotational and axial motion system load frame insert for in situ high energy x-ray studies, *Rev Sci Instrum* 86 (2015) 093902. https://doi.org/10.1063/1.4927855.
[11] K.E. Nygren, D.C. Pagan, J.V. Bernier, M.P. Miller, An algorithm for resolving intragranular orientation fields using coupled far-field and near-field high energy X-ray diffraction microscopy, *Mater Charact* 165 (2020) 110366. https://doi.org/10.1016/j.matchar.2020.110366.
[12] J. Bernier, P. Avery, S. Soderlind, D. Boyce, B. Major, S. Zack, K. Nygren, P. Shade, HEXRD/hexrd: Release 0.9.6, (2024). https://doi.org/10.5281/zenodo.12095606.
[13] R.C. Liebermann, Pressure and temperature dependence of the elastic properties of polycrystalline trevorite (NiFe2O4), *Phys Earth Planet In* 6 (1972) 360–365. https://doi.org/10.1016/0031-9201(72)90059-3.
[14] Chess Analysis Pipeline (CHAP) — CHESS Analysis Pipeline, (n.d.). https://chesscomputing.github.io/ChessAnalysisPipeline/ (accessed April 15, 2026).
[15] J.K. Kurihara, T. Tomimatsu, Y.F. Liu, S.Q. Guo, Y. Kagawa, Mode I fracture toughness of SiC particle-dispersed ZrB2 matrix composite measured using DCDC specimen, *Ceram Int* 36 (2010) 381–384. https://doi.org/10.1016/j.ceramint.2009.07.031.
[16] B. Cotterell, On brittle fracture paths, *Int J Fract* 1 (1965) 96–103. https://doi.org/10.1007/BF00186747.

[17] T. Fett, G. Rizzi, J.P. Guin, J.M. López-Cepero, S.M. Wiederhorn, A fracture mechanics analysis of the double cleavage drilled compression test specimen, *Eng Fract Mech* 76 (2009) 921–934. https://doi.org/10.1016/j.engfracmech.2008.12.016.
[18] Q.Z. Wang, M. Ni, L.Z. Wu, R.Q. Huang, Scrutinized and revised stress intensity factor formulas for double cleavage drilled compression specimens, *Theor Appl Fract Mec* 96 (2018) 803–810. https://doi.org/10.1016/j.tafmec.2017.11.008.
[19] L. Sant'Ana Gallo, F. Célarié, J. Bettini, A.C.M. Rodrigues, T. Rouxel, E.D. Zanotto, Fracture toughness and hardness of transparent MgO–Al2O3–SiO2 glass-ceramics, *Ceram Int* 48 (2022) 9906–9917. https://doi.org/10.1016/j.ceramint.2021.12.195.
[20] B. Deng, J. Luo, J.T. Harris, C.M. Smith, M.E. McKenzie, Molecular dynamics simulations on fracture toughness of Al2O3-SiO2 glass-ceramics, *Scripta Mater* (2019) 277–280. https://doi.org/10.1016/j.scriptamat.2018.11.034.
[21] K.S. Jodha, N. Kaur, S.M. Salazar Marocho, J.J. Mecholsky, S.T. Lirette, Y. Duan, J.A. Griggs, Relationship between fracture toughness and fractal dimensional increment in two types of dental glass-ceramics with different fracture surface roughness, *Dent Mater* 38 (2022) 1977–1988. https://doi.org/10.1016/j.dental.2022.11.011.
[22] M. Tiegel, R. Hosseinabadi, S. Kuhn, A. Herrmann, C. Rüssel, Young′s modulus, Vickers hardness and indentation fracture toughness of alumino silicate glasses, *Ceram Int* 41 (2015) 7267–7275. https://doi.org/10.1016/j.ceramint.2015.01.144.
[23] T. Rouxel, S. Yoshida, The fracture toughness of inorganic glasses, *J Amer Ceram Int* 100 (2017) 4374–4396. https://doi.org/10.1111/jace.15108.
[24] J. Selsing, Internal Stresses in Ceramics, *J Amer Ceram Int* 44 (1961) 419–419. https://doi.org/10.1111/j.1151-2916.1961.tb15475.x.
[25] S.M. Salman, S.N. Salama, Thermal expansion data of some alkali aluminosilicate glasses and their respective glass-ceramics, *Thermochim Acta* 90 (1985) 261–276. https://doi.org/10.1016/0040-6031(85)87104-5.
[26] S. Sakka, J.D. Mackenzie, Relation between apparent glass transition temperature and liquids temperature for inorganic glasses, *J Non-Cryst Solids* 6 (1971) 145–162. https://doi.org/10.1016/0022-3093(71)90053-6.
[27]S.A. de Waal, Nickel minerals from Barberton, South Africa: V. trevorite, redescribed, *Am Mineral* 57 (1972) 1524–1527.
[28] Continuum aspects of crack propagation I: linear elastic crack-tip field, in: Fracture of Brittle Solids, 2nd ed., Cambridge University Press, Cambridge, 1993: pp. 16–50. https://doi.org/10.1017/CBO9780511623127.
[29] K. Suputtamongkol, K.J. Anusavice, J.J. Mecholsky, Cyclic contact fatigue behavior of baria-silicate glass-ceramics as a function of crystal aspect ratio, *J Eur Ceram Soc* 42 (2022) 2441–2448. https://doi.org/10.1016/j.jeurceramsoc.2022.01.012.
[30] E. Apel, J. Deubener, A. Bernard, M. Höland, R. Müller, H. Kappert, V. Rheinberger, W. Höland, Phenomena and mechanisms of crack propagation in glass-ceramics, *J Mech Behav Biomed* 1 (2008) 313–325. https://doi.org/10.1016/j.jmbbm.2007.11.005.

Chapter 4

BREAKING UP: IN-SITU FRACTURE EXPERIMENTS PERFORMED ON POLYCRYSTALLINE ALUMINUM OXYNITRIDE

Sections of this chapter were previously published in: **Gorske, S.F.**, Park, J-S., Kenesei, P., Sharma, H., Almer, J., Voorhees, P., Faber, K.T. "In-situ visualization of a growing brittle crack in aluminum oxynitride using synchrotron X-rays and the double-cleavage drilled compression geometry". *Acta Materialia*, vol. 312, 2026, 122213. https://doi.org/10.1016/j.actamat.2026.122213

4.1 Introduction

When a crack grows through a fully dense, polycrystalline material, the orientations of the constituent grains have a significant impact on quantities like fracture toughness and stress-strain response [1–4]. Additionally, the grain boundaries will have a fracture toughness of their own. Altogether, this means that the energetic description of the material's interior is much more complex than in an isotropic material or matrix, such that predicting where the energy of the crack will be minimized as it grows is difficult, as is understanding what factors impacted crack growth during its lifetime. While sequential focused-ion beam studies on fractured polycrystalline materials can bear some indication of where a crack grew transgranularly (through a grain) or intergranularly (around a grain on a grain boundary), the local strain within grains and the velocity of the crack on or off particular slip planes is largely unknown.

Outside of brittle materials, synchrotron studies of polycrystalline metals undergoing fatigue fracture have allowed for three-dimensional mapping of a crack and its relationship with grains over many loading states and crack lengths [5–10]. Studies of this type have elucidated crack tip phenomena, such as the differing stresses required for the crack to intersect grains at certain orientations and the pathways it might take along certain slip planes within that grain, as well as when intergranular fracture along grain boundaries may be energetically preferred [11–13]. As the crack interacts with grain boundaries and changing

crystallographic orientation, the fracture toughness will consequently deviate from the numerically modeled and experimentally calculated average.

Aluminum oxynitride (AlON, $Al_{23-X/3}O_{27+X}N_{5-x}$) is a polycrystalline ceramic chosen for these experiments [14,15]. As a material with properties useful to industrial and military applications including optics and impact defense, understanding its crack propagation is relevant to many fields. Its equiaxed grains can be grown to be much larger than the crack tip radius, the crack opening width, and the synchrotron techniques' voxel resolution, but smaller by an order of magnitude or more than the DCDC sample's dimensions, such that the crack is bound to encounter grains from a variety of impingement angles and distances from the nearest grain boundary. It is also a face-centered cubic material, so its high crystal symmetry limits the span of orientations each grain can take, allowing for greater ease of computation and comparison. Crucially, the AlON under study also has extremely low porosity, allowing us to investigate its bulk fracture behavior. Two samples will be investigated in this study, demonstrating how changes in the microstructure from sample to sample are a major effect in crack growth.

4.2 Materials and Methods

4.2.1 Materials

AlON pieces were sourced from and machined within 0.2 mm accuracy into bars of dimensions 1.4 × 1.4 × 16 mm^3 by Surmet Corporation (Figure 4.1a). The cross-sectional diagonal was therefore under 2 mm and fits within the synchrotron beam width of 2.1 mm, obviating the need for stitching of tomographic volumes to cover the entire sample cross-section. The drilled holes had surface diameter of 0.42 mm (Figure 4.1b) and deviated from the ideal DCDC geometry, as the holes narrowed conically toward the center of the sample (Figure 4.1c). Additionally, the edges of the faces in contact with the compression platens were lightly chamfered using 1200-grit SiC grinding media to eliminate any unevenness. Two samples, termed Sample 1 and Sample 4 upon receipt from Surmet, were tested. These samples were selected randomly from the number provided; Samples 2 and 3 were not tested. The majority of the grains in both samples were equiaxed and had radii in the range of 50-150 μm, distributed uniformly throughout the volume.

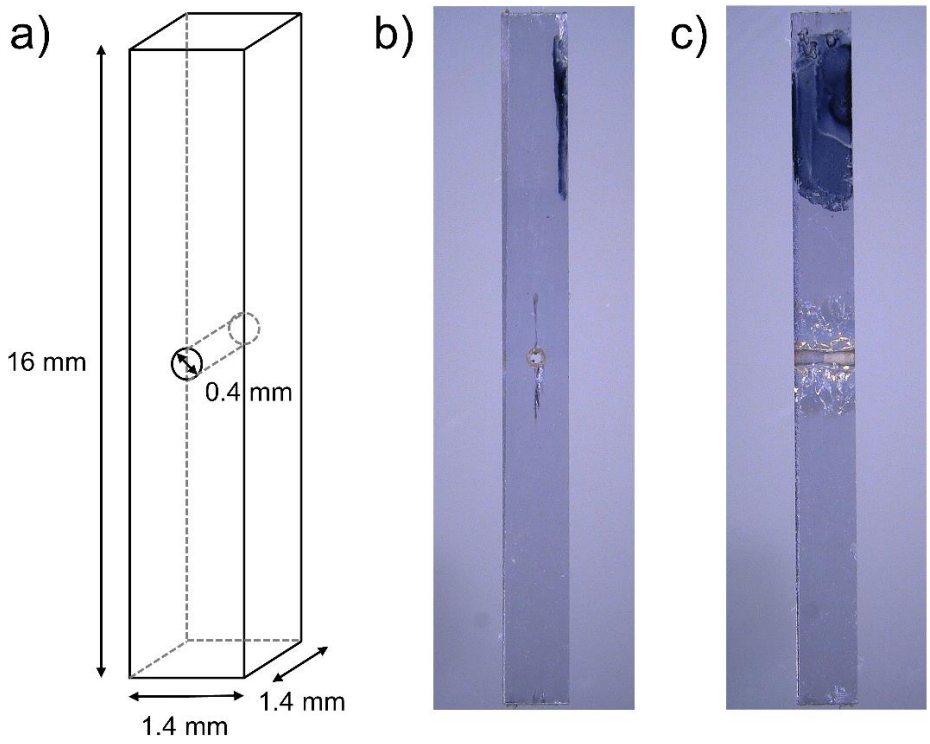

Figure 4.1: The double-cleavage drilled compression geometry. a) Schematic with dimensions used in this experiment b-c) post-experiment optical micrographs of Sample 1 showing the shape and location of the crack, via projections respectively parallel to and perpendicular to the drilled hole; black Sharpie indicates the side investigated during the experiment.

4.2.2 Methods

Synchrotron measurements were performed at the 1-ID beamline of the Advanced Photon Source (APS) at Argonne National Laboratory (ANL). For all measurements, the X-ray beam was tuned to the Hf K-edge (energy of 65.351 keV, wavelength of 0.18971 Å, bandwidth $\Delta E/E \sim 10^{-3}$).

4.2.2.1 Loading

Samples were compressed using the 3rd-generation Rotational and Axial Motion System (RAMS-III) designed by Shade et al. at the Air Force Research Laboratory [16]. A set of steel platens of area 3.2 mm x 3.2 mm were used. In this setup, the maximum allowable

compression loading limit was -2 kN. The reference frame for measurements is depicted in Figure 4.2, where *y* is the loading direction, *z* is directed along the beam, *x* is orthogonal to *y* and *z*, and RAMS-III is rotated about the *y* direction. The sample was mounted and aligned using radiography to ensure its central axis coincided with the loading (*y*) direction. Loading was manually controlled in displacement mode with steps of 0.2 μm, roughly every 2 seconds; displacement at this scale was crucial to prevent large displacement changes, correlating to large increases in load which might lead to catastrophic failure. A live radiograph of the sample, aligned so that the beam was parallel to the hole direction, was monitored to watch for signs of crack pop-in or extension. Whenever this happened, or when the sample load magnitude decreased upon further compression, loading was stopped. The magnitude of the applied load was then manually decreased by 50-100 N to prevent further extension during X-ray measurements, then the load frame was switched over to load control as scanning and rotation commenced.

4.2.2.2 FF-HEDM

FF-HEDM measurements were taken with a single panel GE 41RT amorphous-Si detector (2048 x 2048 pixels, 0.2 mm/pixel) located 1.4 m downstream from the sample (Figure 4.2a). A box beam of dimensions 2.1 mm (*x*) x 0.1 mm (*y*) was used for all volumes probed. Diffraction patterns were recorded 360° in ω with frames in intervals of $\Delta\omega$=0.25° for a total of 1440 frames per scan. The Microstructure Imaging for Diffraction Analysis Software (MIDAS) was used to identify the orientation, center of mass (COM), size, and elastic strain tensor (ε) of the constituent grains in the illuminated volume [17-19]. Diffraction spots from the {311}, {400}, {422}, {511}, and {440} peaks were present in sufficient number and intensity to be used for characterization of individual grains. When the ratio of number of observed diffraction spots to the theoretical number present in a complete Bragg pattern for that orientation (termed completeness) exceeded 80%, the grain was retained for further analysis. The anisotropic cubic stiffness tensor of a single AlON crystal (C_{11} = 334.8 GPa, C_{12} = 164.4 GPa, C_{44} = 178.6 GPa [20]) was used to generate the stress tensors from the corresponding strain tensors.

FF-HEDM scans at near-zero load were used to calculate the unstrained lattice parameter. The grains in Sample 1 had a mean lattice parameter of 7.9486 Å at -5 N load and those in Sample 4 had a value of 7.9461 Å at -30 N load. Both values are within Surmet's reported range of lattice parameters for AlON, which can vary depending on the ratio of oxygen to nitrogen in its formula [14], so this difference in lattice parameters ($\Delta a/a \sim 2 \times 10^{-4}$) is unsurprising for two samples from different batches. Using the average lattice parameter between these two samples as a baseline resulted in the estimated residual stress at zero load to be on the order of ±100 MPa in all directions, so the strains in each sample were computed using their respective values for the unloaded lattice parameter a0.

4.2.2.3 NF-HEDM

NF-HEDM measurements were taken with an in-house designed detector (2048 x 2048 pixels, 1.48 mm/pixel) with a QImage Retiga 4000DC CCD camera positioned sequentially at two distances, 8.56 mm and 11.56 mm away from the center of the sample, and a focused beam 1 μm (y) x 2 mm (x) [21,22] (Figure 4.2b). For each scan, the sample was rotated 180° with $\Delta\omega$=0.25°, generating 720 diffraction images per detector distance. The scans were spaced μm apart so as to cover a larger volume; between scans, the grain boundaries can be reasonably interpolated due to the much larger relative size of the AlON grains. The MIDAS software was also used to process the data; using the grain orientations from the corresponding far-field scans as a seed, the software assigned each 5 x 5 x 5 μm^3 voxel a most-likely orientation and a confidence value.

4.2.2.4 μ-CT

The μ-CT measurements were taken with an in-house designed detector (1920 x 1200 pixels, 1.172 mm/pixel) which utilized a PointGrey Grasshopper3 CMOS camera (Figure 4.2c). The beam was 2.1 mm x 1 mm, and radiographs were acquired at 0.2° $\Delta\omega$ steps from 0 to 360° with 0.077 s exposure for 1800 total frames. Ten bright-field images and ten dark-field images were acquired for normalization. In-house software was then used to reconstruct the volume with the GRIDREC algorithm implemented in MIDAS [23] resulting in a tiff image with 1024 layers and voxel size 1.17 x 1.17 x 1.17 μm^3. Features with dimensions

greater than 5 μm in a given direction could be clearly rendered, with smaller features becoming semi-visible until they were smaller than the voxel size.

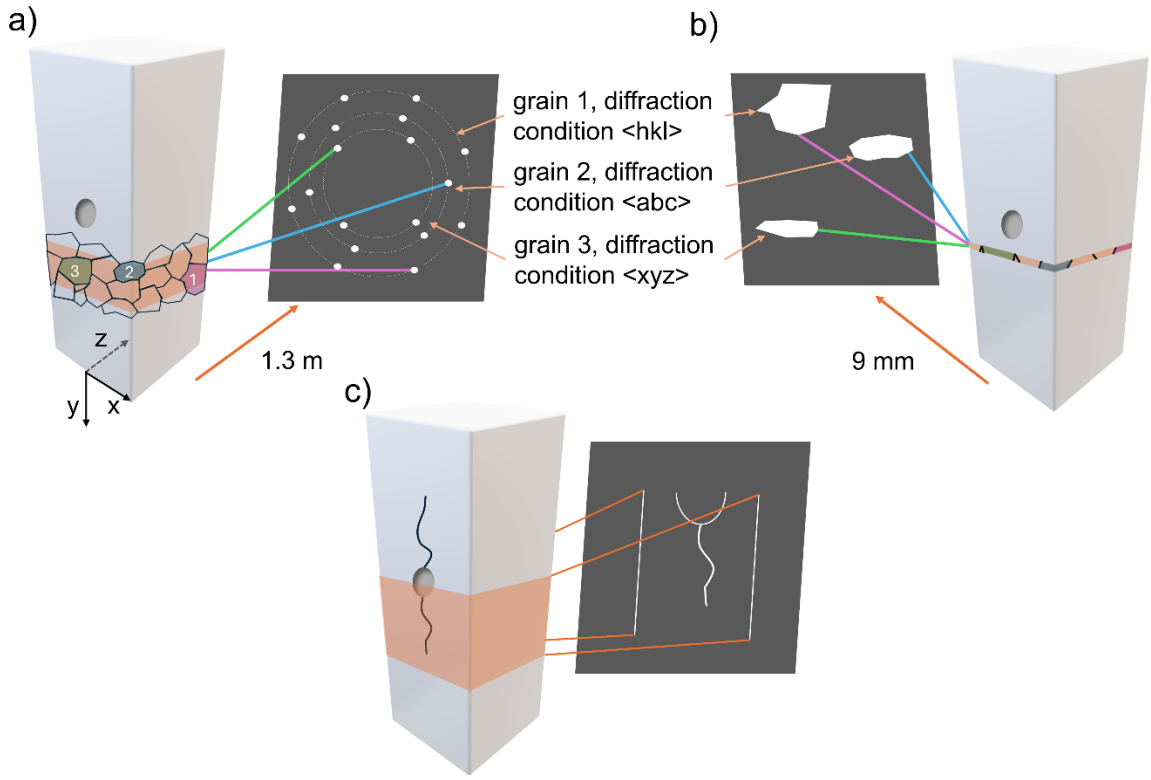

Figure 4.2: Visualization of synchrotron X-ray HEDM and μ-CT performed at Beamline 1-ID with frame directions: a) FF-HEDM, with reference frame marked. b) NF-HEDM. c) μ-CT.

4.2.2.4.1 Crack detection program

Post-processing of the tomography images started with the application of a non-local means filter [24] throughout the entire volume, with the region size chosen automatically by the ImageJ software, to decrease background noise. Next, a median filter extending two pixels in each direction away from the central voxel was applied for further smoothing and suppression of any remaining ring artifacts. Finally, a second non-local means filter was applied to each layer of the image stack individually, without input from the rest of the volume. After these steps, a custom crack detection program was used to determine the

location and width of the crack structure as well as the approximate location and error bounds of the crack tip.

The first part of the program used slices of the tomographic volume perpendicular to the direction of loading, specified as the y-axis. Figure 4.3 displays representative slices of studied AlON samples with the coordinate system labeled. The primary method of detecting the crack was marking locations on the 2D slice where, along a 1D intensity line, a sinusoidal shift in intensity marked a phase change (in this case, air to solid and vice versa). As air absorbs fewer X-rays than a solid, a drop in image intensity corresponds to a decrease in absorption, and thus the potential presence of a crack. Because of the phase contrast, the intensity should also peak above the background before the phase change, creating the sinusoid-like intensity profile. The clearest indication of a crack is when an intensity drop (defined as 125% of the standard deviation below the mean after testing multiple values) is bounded on either side by an intensity peak (75% of the standard deviation above the mean), representing the double phase-change from solid to air and back. In order not to exclude features that did not exactly meet these criteria, two additional markers deviating from ideal were included in the algorithm: a single peak beside a 150% standard deviation absorption drop, as well as a 200% standard deviation decrease in intensity without any peaks. Further, the crack opening behind the crack front was at maximum less than ten pixels, or 11.7 μm wide, and grew narrower closer to the crack tip. As a result, the distance between the two phase changes grew increasingly smaller and the two sinusoids could be indistinguishable. Thus, locations lacking an intensity drop and only possessing an intensity peak can also indicate the presence of the crack. However, since some bright artifacts were also present, as well as the peaks to either side of the already-marked crack locations, bright sections were only included in the crack pixel count when directly below previously marked crack spots.

After identifying these features, further filtering was implemented to reduce the presence of both false negatives and false positives. First, points identified as possibly belonging within the crack via the previous procedure were assigned to groups with the same (x,z) pixel location in different slices in the stack and sorted by height (y) within the tomographic volume, then the distance between consecutive marked points was computed. If fewer than one-third of the slices between the lowest and highest y-slice at that location contained an

identified point, or if those slices were separated by less than 5 pixels, the location was considered spurious due to excess noise, and all points were removed from consideration as being part of the crack front. For locations with sufficient density of marked points, any gaps smaller than 10 pixels were deemed to be false negatives and filled in as part of the crack front. If the gap was larger, the marked locations on either side were treated as individual crack segments and subjected to the earlier considerations. By applying these arguments, an additional benefit was gained: the appearance of the crack front became self-similar for differing threshold values during the initial marking algorithm, thus eliminating much of the subjective nature of those values. Figure 4.4 displays the same tomographic slices as Figure 4.3 with the identified crack marked in blue.

4.2.2.4.2 Uncertainty in the crack length

Due to the narrow nature of brittle cracks, the singularity at the crack tip, and the limits of the tomographic resolution, the true extent of the crack tip is not visible directly in the tomography images. It was estimated by assuming the crack to narrow parabolically toward the crack tip [25] and measuring the crack width in a region until the resolution limit blurred the feature's existence; this occurred at around 3 pixels or 3.5 μm wide. Even at wider locations, the true width could be obscured by the presence of the phase-contrast wrinkle artifacts [26], so the measured width at every depth was not used in the calculation. Instead, the deepest point at which the crack had a specific width was used to fit the parabola (Figure 4.5), since even with uncertainty the crack never became that width again, indicating that it was indeed narrowing. The resultant parabola indicated that the true crack tip was 45-60 μm ahead of the final point used in fitting the curve. This roughly corresponded to the depth at which the crack detection program described in Section 2.2.4.1 identified the crack's presence. Further assuming that the crack could be up to 1 μm wider than measured due to the pixel resolution being much larger than the crack width near the tip showed that if this is the case, the crack tip could be up to 30 μm further ahead of the point identified by the crack detection program. The uncertainty in the depth of the crack tip as used in Equation 2.5 and Figure 4.4 was thus set to be 50 μm shorter than measured, indicating the distance from the

last detected point to the last point with good resolution, to 25 μm longer than measured, the approximate distance that the crack tip might be away from the last detected point.

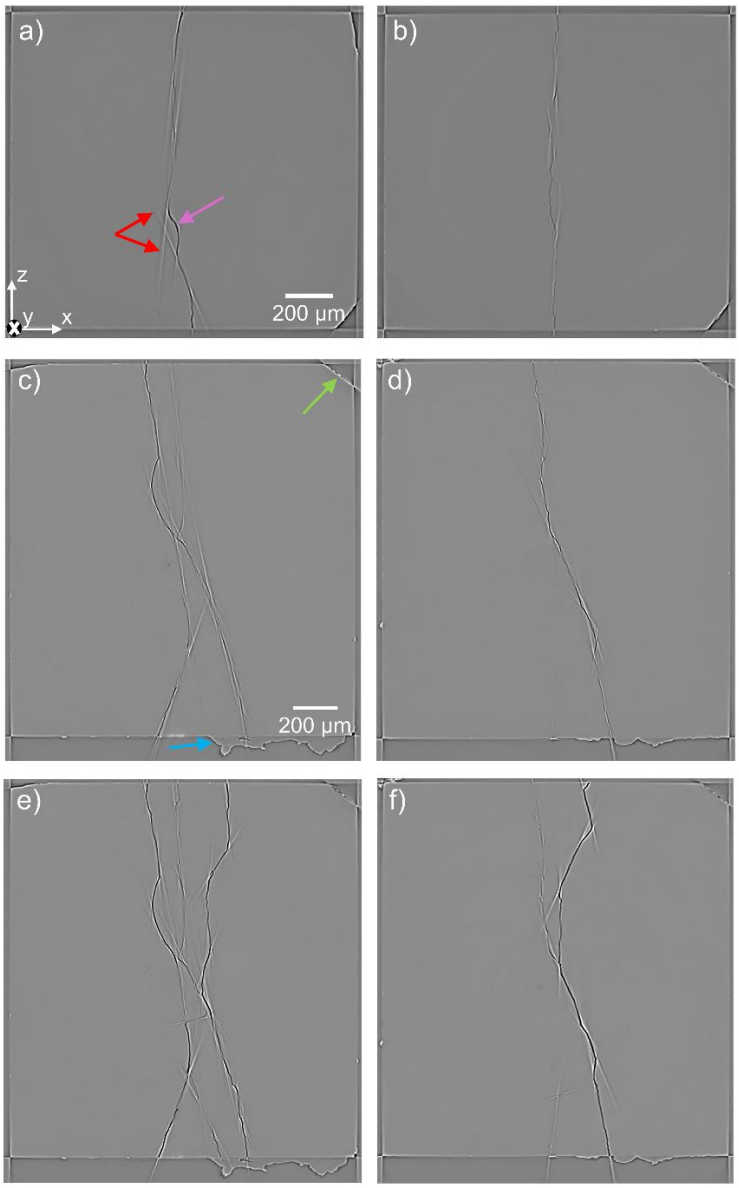

Figure 4.3: 2D crack trace in aluminum oxynitride viewed with µ-CT, where the loading direction y points into the page. Example features of note are marked, including the crack (purple), artifacts (red), machining errors (green), and debris from laser-cutting the hole (blue). a,b) The crack directly below the hole and 386 µm away from the hole, respectively, in Sample 1 at -1900 N. c) The crack directly below the hole in Sample 4 at -1450 N. d) The crack directly below the hole in Sample 4 at -1750 N. e) The crack 397 µm away from the hole in Sample 4 at -1450 N. f) The crack 394 µm away from the hole in Sample 4 at -1750 N.

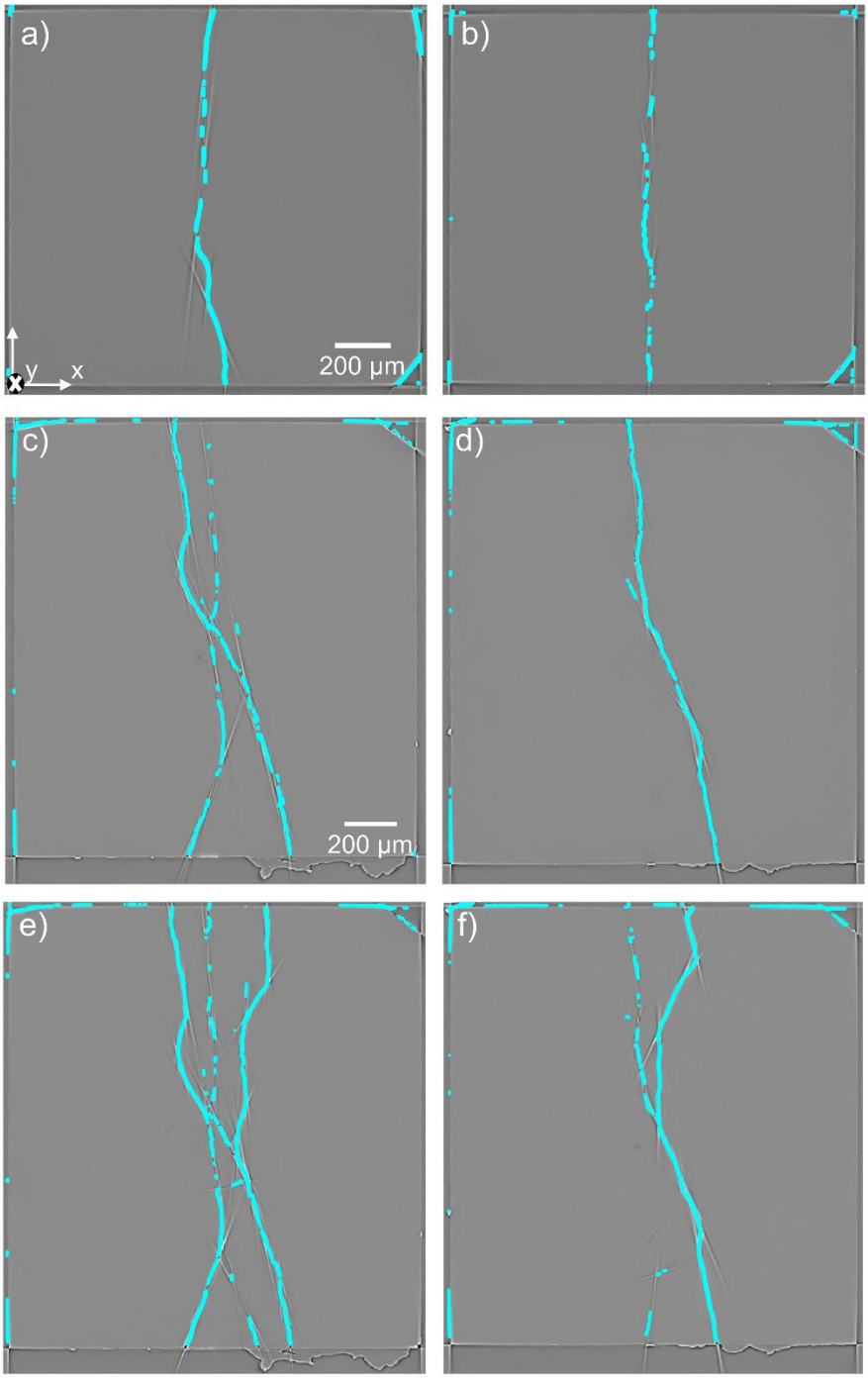

Figure 4.4: The crack detection program applied to the tomographic images of Figure 4.3.

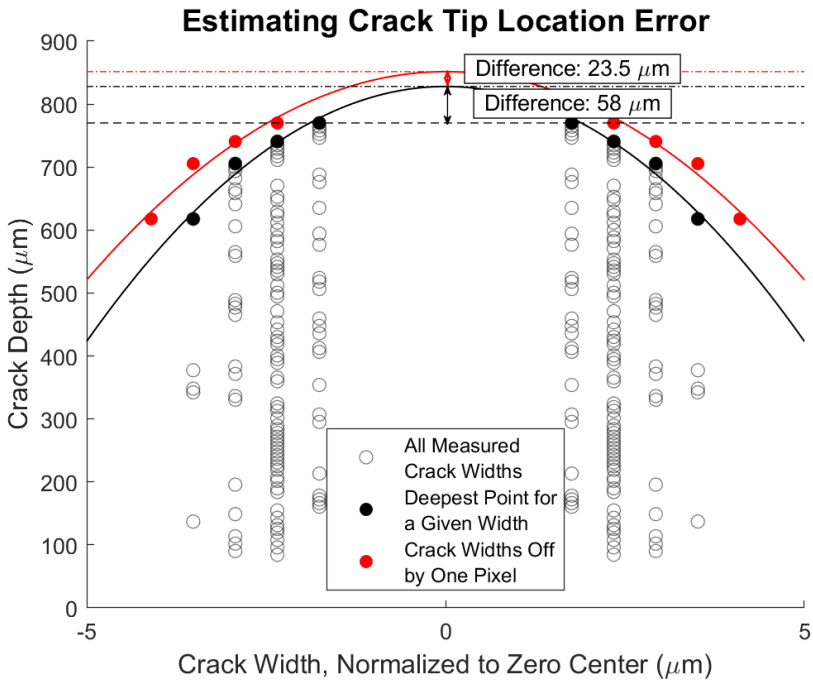

Figure 4.5: Measured crack widths at a sample location with the fitted parabola to the selected best points (black) and the wider points (red). Relevant distances between the intercept of the best points parabola (approximately the deepest point marked by the crack detection program), the deepest point with good resolution, and the intercept of the parabola with 1 pixel uncertainty, are labeled. The average differences when compared at multiple sample locations were 25 and 50 μm.

4.3 Results

4.3.1 FF-HEDM strain tensors

Upon loading, the randomly oriented AlON grains displayed individual strain states, the magnitudes of which varied slightly between different sections of the grain if its volume was captured in multiple FF-HEDM scans. Average strains were generally compressive in the direction of applied load (Figure 4.6a-b), in accordance with the compressive load, while the strains in the orthogonal directions trended more tensile, and had smaller magnitudes (Figure 4.6c-f). With increased loading, the magnitudes of the compressive and tensile strains increased along each primary axis in the reference frame, and the width of the range of the

strains tended to increase as well, as a result of each grain having a unique response to the system load.

Additionally, the stress field displayed a dependence on crack location. For grains located under the hole and near the plane of the crack, the stresses in *x* and *z* followed roughly the same trend as those further away on the edges of the sample. In the *y* direction, however, the stress was lower in magnitude for those grains in the path of the crack for approximately 700-800 μm before converging in Sample 1, and 700-1100 μm for Sample 4 (Figure 4.7).

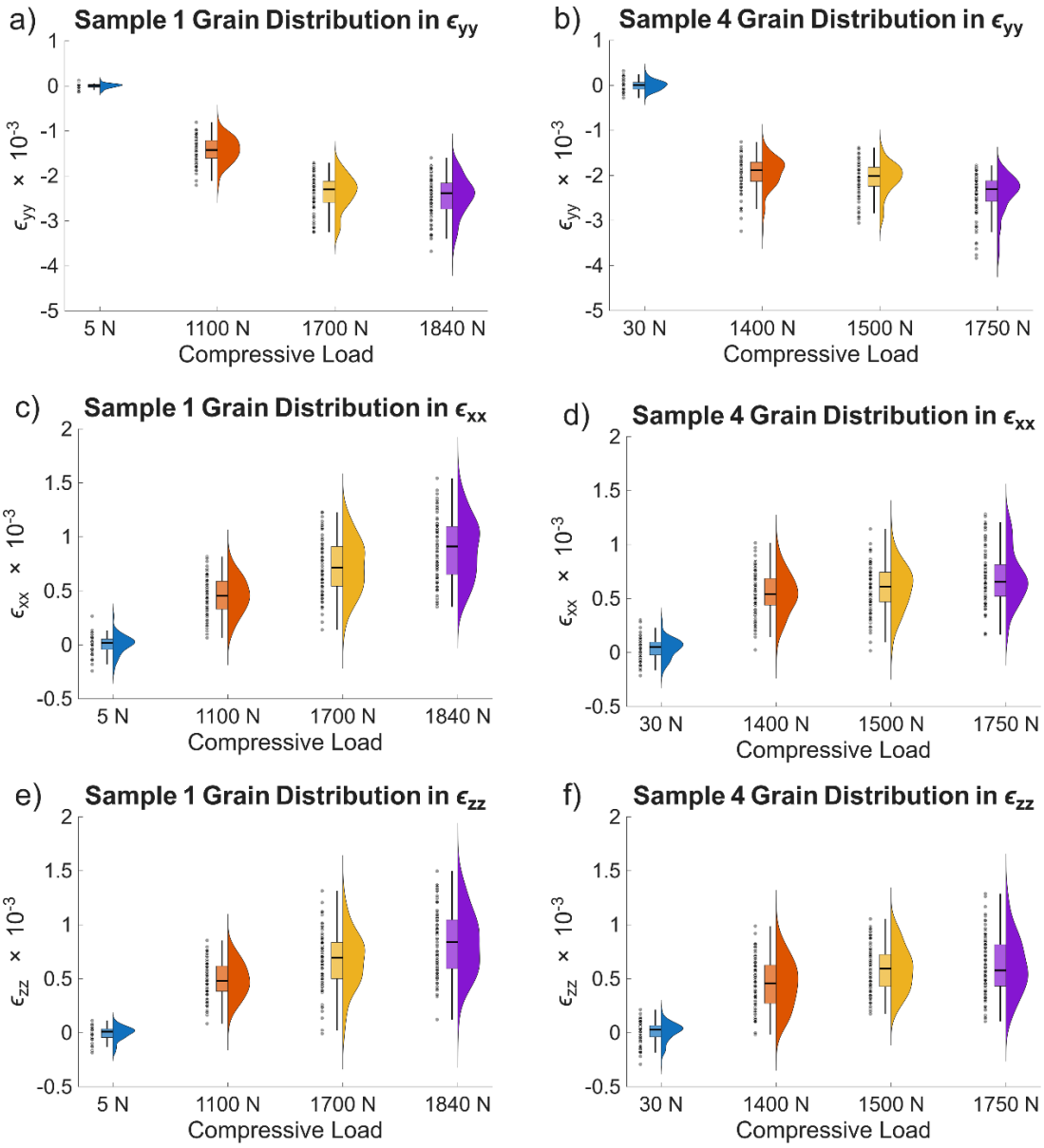

Figure 4.6: Raincloud plots for the strain tensor component at multiple load steps for grains illuminated via FF-HEDM. For each load step, the individual strain values are plotted beside the box plot and density plot to highlight the median value, interquartile range, and distribution. Left (a,c,e): Sample 1 and Right (b,d,f): Sample 4. a-b) ϵ_{yy}, where y is the direction of loading, c-d) ϵ_{xx}, where x is perpendicular to the hole in the sample, and e-f) ϵ_{zz}, where z is directed along the hole.

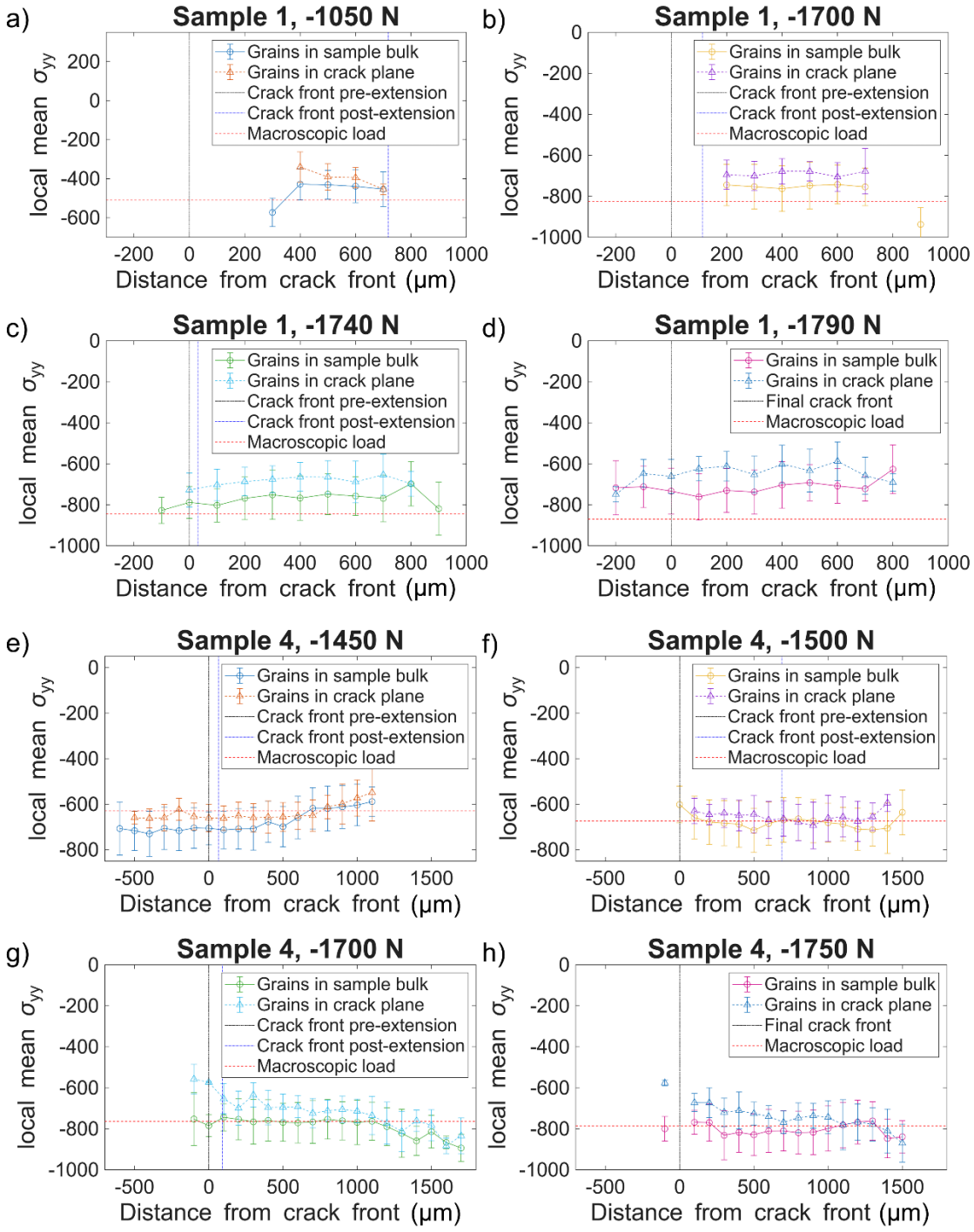

Figure 4.7: The average stresses, determined via FF-HEDM, in the loading (y) direction as a function of distance from the crack front, compared to the macroscopic applied load and with future crack extensions shown. a-d) Sample 1. e-h) Sample 4.

4.3.2 Crack extension

First pop-in on both the upper and lower side of the hole was achieved at -1160 N in Sample 1 and -1536 N in Sample 4 (Figure 4.8a,c,e). After segmentation of the tomography (Figure 4.8b,d), the initial pop-in event in Sample 1 was measured to be about 81 μm at its deepest point, approximately the diameter of a single grain. Sample 4 experienced a larger amount of extension at pop-in, which ended at about 1314 μm at its deepest point, greater than an order of magnitude more than Sample 1. A smaller event may have preceded and been subsumed by this extension, but this was unclear as it was not captured via μ-CT.

In Sample 1, the crack popped in approximately parallel to the hole's center line, with some deviation near the center of the sample (Figure 4.3a). As the crack extended further, while it continued to have some regions where it deviated from the center line, the two-dimensional projection became even more linear (Figure 4.3b), in accordance with expectations laid out in literature for both the DCDC geometry [27] and brittle, microscopically anisotropic materials with macroscopic isotropy [28]. In Sample 4, the popped-in crack was more complex, spanning from the outer edge of the hole on one face towards the center, where it branched into two crack fronts which reached to the edges of the hole on the other side (Figure 4.3c). Further, as the load was increased, another branch popped in at the hole, next to the unbranched section of the original crack, forming close to an X shape with diagonals stretching from the outer edges of the hole on one face to the opposite edges on the other face (Figure 4.3d). Closer to the crack tip, the earlier stages of the crack coalesced into a single crack front, with the 2D projection again much straighter than that just below the hole (Figure 4.3e). However, when the new branch popped in at the hole, it continued to extend until it surpassed the former crack tip, becoming the new singular crack front (Figure 4.3f).

Crack progression continued irregularly in Samples 1 and 4; instead of achieving a stable velocity or growing proportionally to the applied load, the crack in both samples continued to act similarly to the initial growth event. The crack essentially popped-in to each new section in jumps ranging from ~50 μm to over 1 mm, similar to the variance in initial pop-in lengths, and often the extension was localized and may have only extended through a few grains along the crack front at a time. As noted for pop-in, the smallest jumps are around the

same size as the smallest grain diameter, indicating that the crack in each region of extension moves across or around one or more discrete grains before being pinned at grain boundaries. The new extent of the crack and the load at which extension occurred is visualized in Figure 4.8e.

In general, the greatest extension occurred near the center of the sample, similar to the U-shaped curve predicted by Fett et al. [29] and seen by Nielsen et al. in a DCDC polymethylmethacrylate sample [30]. However, the shape of the crack front was far more irregular than modeled by those authors, varied between both samples, and was not self-similar with each further extension (Figure 4.8a,c).

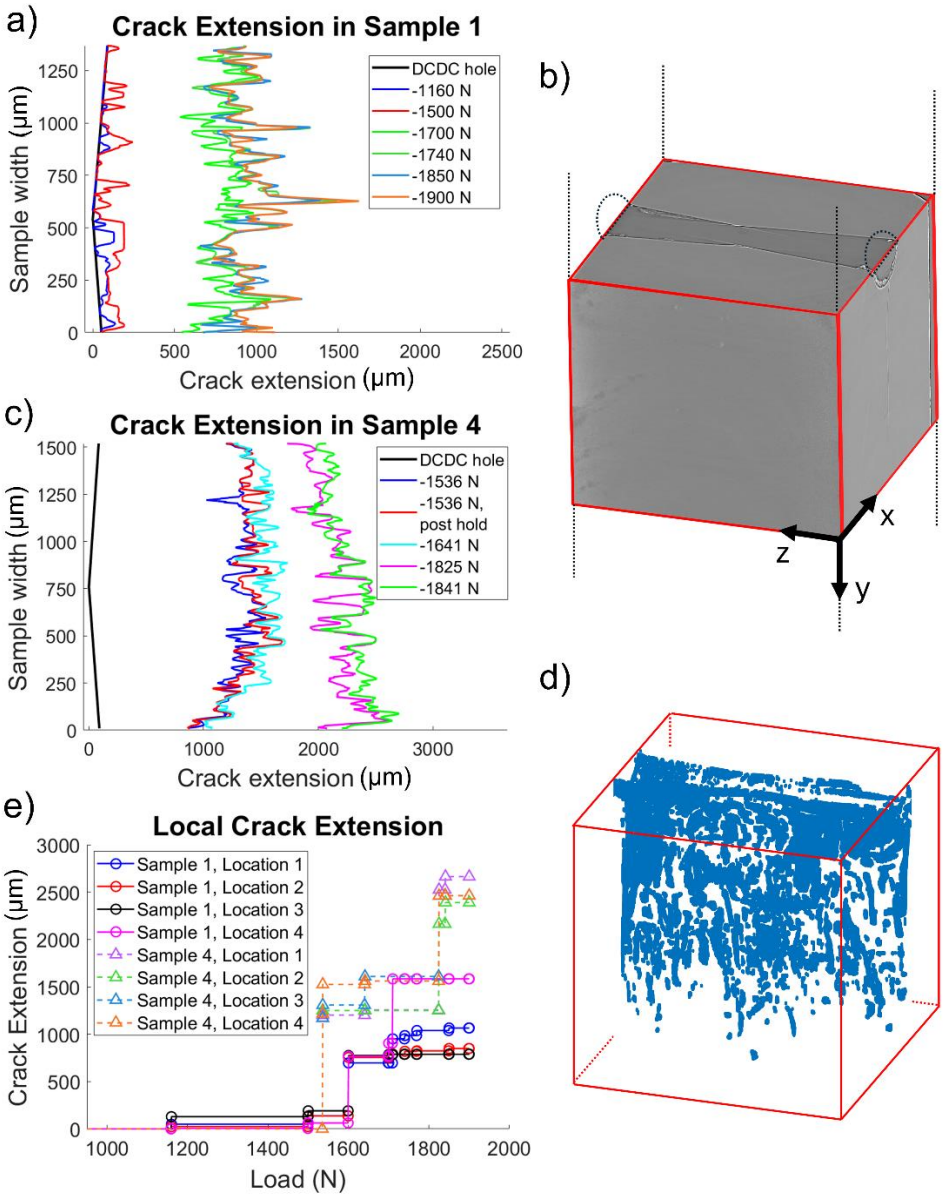

Figure 4.8: Visualization of crack extension. The crack front extended in discrete events as loading increased in both a) Sample 1 and c) Sample 4, although the crack front was not self-similar at each new extent. b) A representative tomographic volume from Sample 1 displaying the hole of the DCDC geometry. d) The pointwise segmented crack from the volume in b) corresponding to the crack front in Sample 1 at -1900 N as seen in a). e) Crack extension as a function of macroscopic load in Samples 1 and 4 at multiple locations along the crack front, showing that the crack front progressed irregularly.

Samples 1 and 4 were loaded to a maximum of -1900 N. The crack grew to a maximum length of 1.71 mm in Sample 1 and 2.51 mm in Sample 4 at the deepest point. As the cracks grew, the opening width at the hole also grew larger. In Sample 1, the opening width at pop-in was smaller than the reliable tomographic resolution and was visible only from the presence of phase-contrast artifacts [26] and can be assumed to be much smaller than 5 μm, but at -1900 N the crack spanned at least 7 μm at its widest. For Sample 4, the opening width after pop-in at -1536 N spanned about 4.7 μm and widened slightly to 5.9 μm at -1900 N.

4.3.3 Intergranular vs transgranular fracture

Grain maps from the limited regions with both FF-HEDM and NF-HEDM are registered with tomographic reconstructions, such that tracking which grains the crack went around or through, and their associated local crystallographic orientation and stress state, is achievable (Figure 4.9a-b). For areas where NF-HEDM confidence was low in between two grains (less than 80%), the crack was considered as being intergranular if it passed through those regions. AlON tends to crack transgranularly [14,31], so grain boundaries are not expected to impact the crack's path significantly, and while face-centered cubic structure, in general and in AlON, often has {111} slip planes [32], the crack was not observed on those planes in particular (Figure 4.9c-d). The average crack plane and its normal were calculated using singular value decomposition on the segmented crack points proximal to that grain.

Grains which were cracked transgranularly or which neighbored an intergranular section of the crack were not clustered around preferred orientations, and the two populations did not display any different trends in orientation (Figure 4.10a). Additionally, the average plane of the crack in those grains did not correspond to any notable cubic slip planes or clusters of planes, indicating there were no preferred or prohibited crack planes (Figure 4.10b). Further, the grains which were cracked transgranularly and those bypassed by intergranular fracture also did not have any differing trends in strain or stress response (as observed before crack extension) when compared to each other or the entire population of grains (Figure 4.10c-d). The stress magnitudes across the crack and in other directions also did not display any

correlation to the grain orientations in the full population of grains or the intergranular and transgranular populations (Figure 4.10e-f).

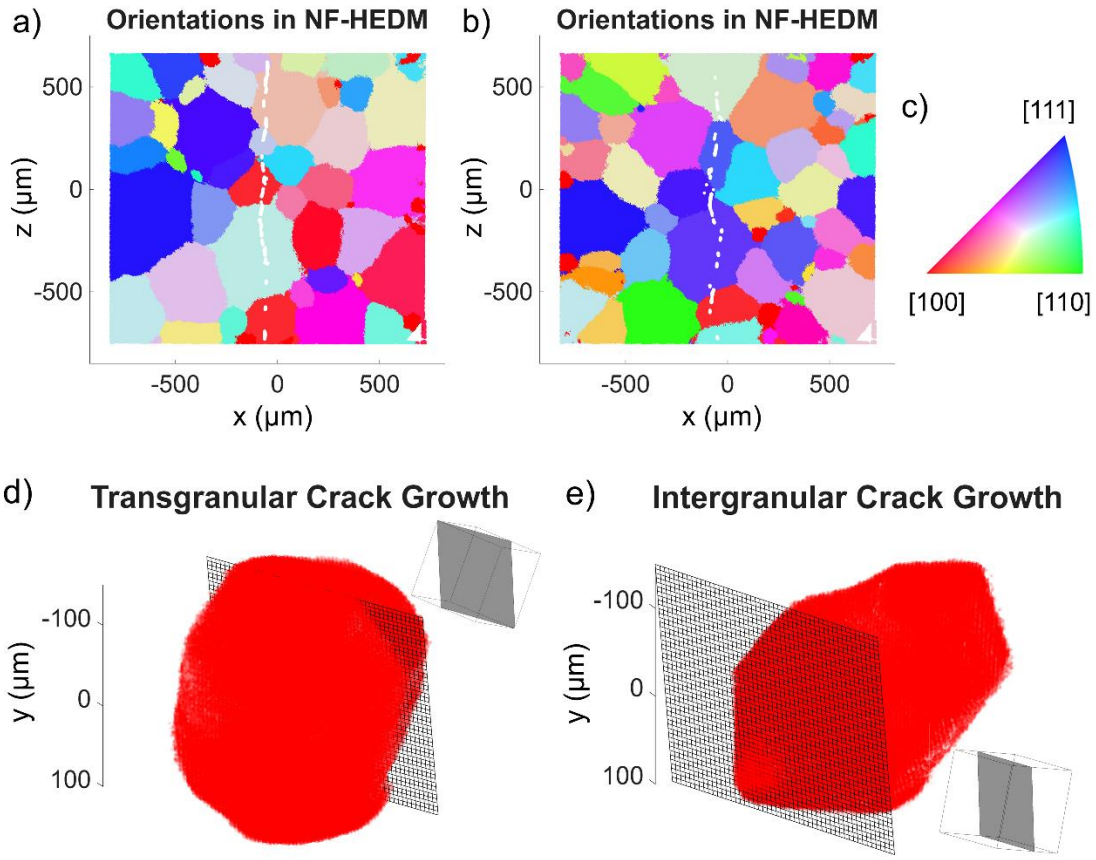

Figure 4.9: Registration of μ-CT and NF-HEDM in Sample 1. a-b) NF-HEDM reconstructed microstructures in x-z slices, 389 μm and 589 μm away from the bottom of the hole respectively. Grain orientations are shown in standard inverse pole figure coloring (c), and the crack extracted from tomography is superimposed in white. NF-HEDM data was collected at -1160 N load, before the crack extended through the region. d) 3D model of a grain which was cracked transgranularly and e) one around which the crack grew intergranularly, with the average crack plane (black mesh) superimposed; insets show the orientation of the crack plane with respect to the grain's unit lattice.

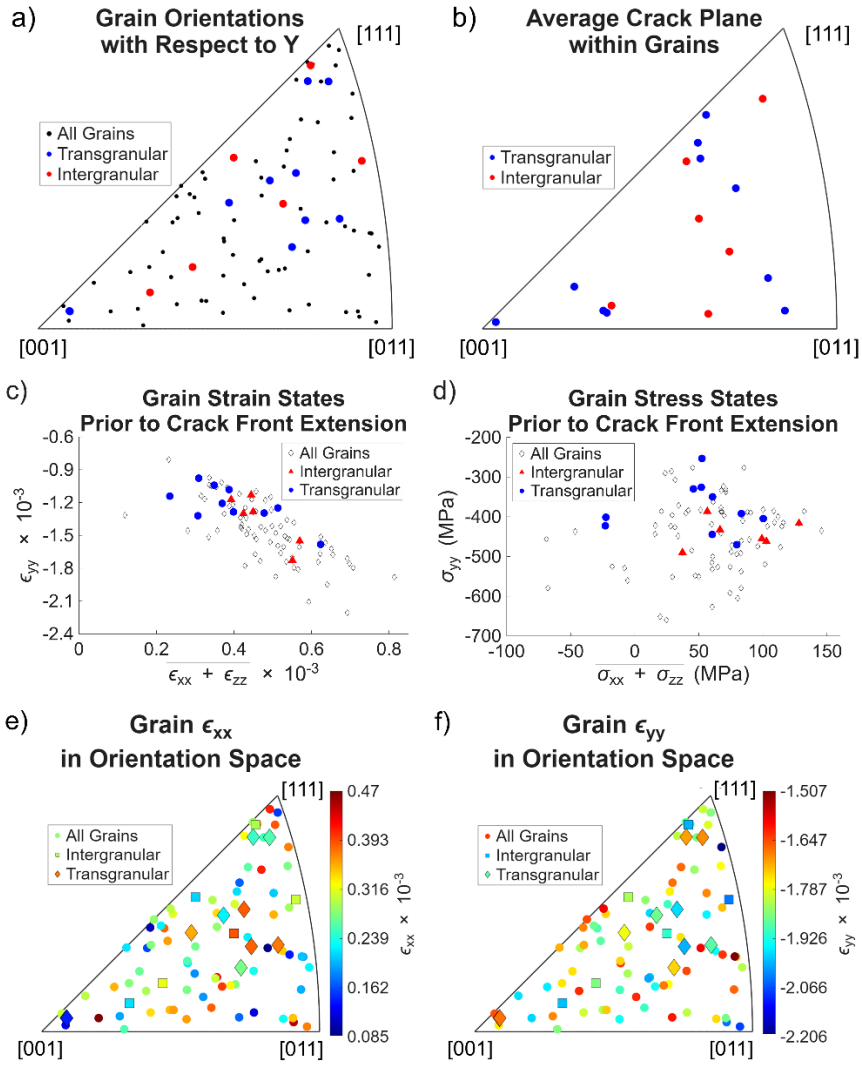

Figure 4.10: FF-HEDM data corresponding to the NF-HEDM volume in Figure 4.9, with the grains through which the crack moved (transgranular) and those which it moved around (intergranular) marked. a) Inverse pole figure for the grain orientation component with respect to the loading direction. b) Orientation distribution of the direction normal to the average plane of the crack within each grain's unit lattice, as visualized in 7c-d). c-d) Distribution of the strain and stress states, respectively, with the component in the loading direction *y* plotted against the average of the two transverse components. e) Distribution of the stress component in *x*, approximately perpendicular to the crack (colors), vs the orientation map in a). f) Distribution of the stress component in *y* (in the loading direction) vs the orientation in a).

4.4 Discussion

4.4.1 Fracture toughness

In Sample 1, crack extension only occurred with increased load beyond the load at previous extension, in accordance with the DCDC geometry expectation. However, the crack did not extend with every increase in load, instead becoming arrested even as the load increased by hundreds of Newtons. Sample 4 behaved similarly after pop-in for its first few extensions, although the initial crack had some branching and the lengthier initial pop-in indicates some initial instability. Further, the second pop-in event and subsequent new location of the crack tip (Figure 4.3e-f) indicates that it became more favorable to pop-in a new crack front rather than extend the original front segment further.

Prior to the second pop-in, a localized gradient in σ_{yy} was observed ahead of the crack front (Figure 4.7g). Before the new pop-in, the compressive stress experienced by the volume just ahead of the crack decreased when compared to the volume away from the crack, while at distances far from the crack, the magnitude was greater than the applied load. While the limited number of discrete extension events precludes a definitive statistical correlation, this observation suggests that localized stress heterogeneities play a role in intermittent crack propagation as the stresses acting to open and extend the crack become disrupted [33].

We are currently working to explore such considerations in anisotropic and polycrystalline media using dedicated phase-field models, as well as to relate stress development and crack motion to differently oriented lattice planes and grain boundaries. These local microstructural changes can provide further barriers to unimpeded growth as the energy needed to extend cracks in these regions changes due to the anisotropic elastic constants. In a related work to this thesis, when systematically studying crack behavior at grain boundaries based on FF-HEDM data as a function of the five grain boundary degrees of freedom, both the misorientation and the plane normal direction are identified as important for crack pinning [34].

The large crack extension events such as at the initial and secondary pop-ins in Sample 4 and the jump at -1600 N in Sample 1 indicate that there are also regions where crack growth is relatively uninhibited. In an isotropic sample with invariant fracture toughness, the incremental increase in load needed to induce cracking in the next region grows

proportionally with crack length [35]. Here in the anisotropic samples, that load requirement is additionally affected by the local fracture toughness, and the necessary load may be increased (leading to the crack becoming arrested as greater loading is needed to extend it) or reduced (causing longer extension events). If the crack front was arrested at a region with higher fracture toughness, and subsequently grows after the load is increased, it may enter a region where the necessary load to extend the crack has already been exceeded, and thus it will proceed until reaching another stopping point. The changing fracture toughnesses in differently oriented grains can be seen in the work of Guo et al. in [32], where the average measured fracture toughness range is reported as well as the fracture toughnesses measured for two individual grains, which are both outside that average.

From the literature, the fracture toughness (K_{Ic}) of AlON has an average value of 2.09 ± 0.06 MPa $\sqrt{\text{m}}$ [31] using the single-edge pre-cracked beam geometry in air. Other methods, including the single-edge pre-notched beam geometry [36] and Berkovich nanoindentation [32], result in average values ranging from 2.4 to 3 MPa $\sqrt{\text{m}}$; however, outliers from the latter had values measured as low as 1.4 MPa $\sqrt{\text{m}}$. These values are reported against those from this work, obtained using Equation 2.5 [37].

Crack extension in Sample 1 occurred at higher loads relative to crack length than Sample 4 for all growth events, and thus had higher fracture toughness values, which fell within the range reported from the single-edge pre-notched beam geometry and Berkovich nanoindentation. This effect may be partially explained by the fact that the compressive y stress ahead of the crack in Sample 1 was in general lower in magnitude than the applied stress, and thus higher loads were needed to reach the equivalent stress for local extension (Figure 4.7). Meanwhile, the fracture toughness of Sample 4 was in the lower range obtained from the single-edge pre-cracked beam geometry (Figure 4.11). The earliest extension events in Sample 1 were not included, as the relative length of the crack front did not satisfy the $\beta \leq \alpha$ condition required in Equation 1.

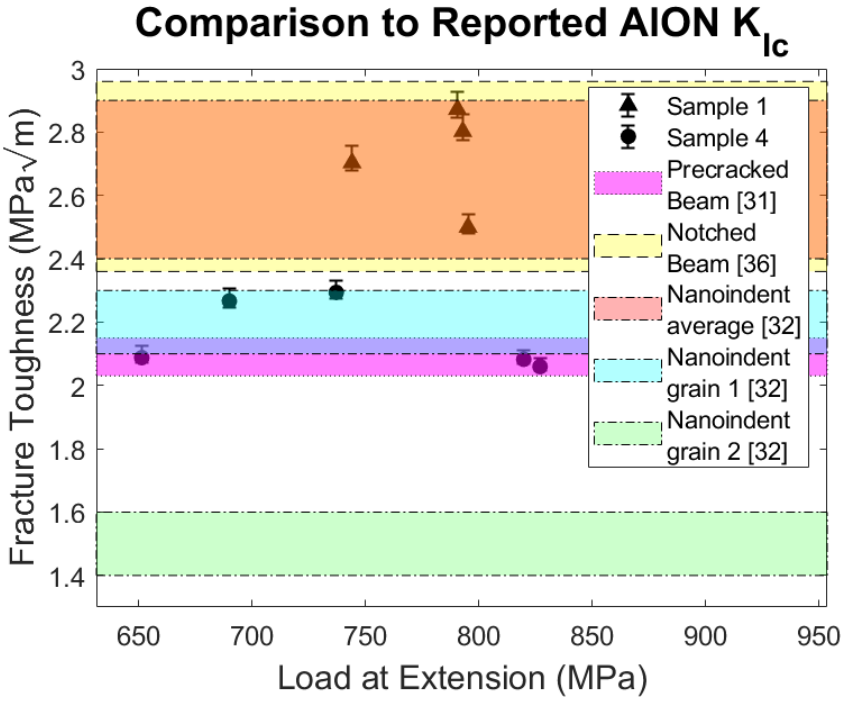

Figure 4.11: The calculated fracture toughness using Equation 2.5 from reference [37] compared to the isotropic fracture toughness of aluminum oxynitride (AlON), using the maximum crack length, and the RAMS load at which crack extension occurred. Data points from Samples 1 and 4 are plotted against the reported ranges of AlON from the precracked beam test [31], the average range and two individual grain ranges from Berkovich nanoindentation [32], and the notched beam test of reference [36] and one of the individual grain measurements [32].

4.4.2 Intragranular strain variation

Individual AlON grains have not only different fracture toughnesses varying with orientation [32] but also a spread in that measurement, indicating that the strain field varies within grains and further complicating the microstructure with which the growing crack front interacts. This is corroborated by the fact that for grains with diameters larger than the 100 μm height of the FF-HEDM scans, the average reported strain tensor could vary by $1\text{-}3\times10^{-4}$ in different regions that were illuminated by the beam. Additionally, within many grains mapped via NF-HEDM, the completeness value can vary, indicating regions of greater and lesser agreement with the expected diffraction pattern. The altered confidence could be a

result of variations in the chemical composition of AlON, especially in the local ratio of oxygen to nitrogen, which is correlated with lattice parameter [14]. Narrow twinned regions with widths on the order of a few microns have also been reported in AlON [38], and might provide a source of lowered confidence.

Taken together, the variation in average strain tensor and diffraction pattern for different sub-granular regions indicates that the imposed macroscopic load is distributed unevenly among grains as a result of the grains' anisotropy and differing size and orientation. Cocke et al. have performed analysis based on the samples in this work, aiming to recover the intragranular strain fields and spatially resolved macrostress state from the grain-averaged data, with simulations demonstrating high stress variance spatially within grains [39].

4.4.3 Microstructural effects on crack behavior

While it appears that the orientation, stress, and strain of the grains ahead of the crack has little effect on whether the crack moves transgranularly or intergranularly, this is not to say that there is no effect of these variables on the crack itself. As already shown, grain orientation can have a major effect on the local fracture toughness, and the stress and strain states of adjacent grains necessarily impact each other, all of which taken together play a major role in where the crack front stops after extending.

As noted earlier, in the literature AlON does tend to crack transgranularly, indicating that the grain boundaries do not have such a lower fracture toughness compared to the grains that they would sharply alter the crack path. While the crack did change orientation as it grew, angular changes were usually gradual, smooth, and occurred over a range of tens to hundreds of microns, that is, over the range of grain sizes in the AlON studied. With few persistent orientation changes in the form of a sharp angle beyond those angles inherited from the shape of the popped-in crack, or deflections of entire grain-size segments of the crack, the crack often retained much the same orientation when entering a grain below its position instead of having its path altered to go around a grain. Partly, this may be the case due to the size of the grains. Creating surface area around a grain with a diameter of 100 μm or more would be energetically costly, and the crack's arrest and persistent shape upon further extension shows that it is generally more favorable for the energy to be released by

eventual extension rather than immediate deflection to a grain boundary not in the vicinity of the crack. While grains which were adjacent to intergranular cracks generally had larger radii, there were also transgranularly-cracked grains with similar radii, so radius alone is not an indicator of whether a grain will be cleaved by fracture. However, a more salient point is that most of the intergranularly-cracked grains were more distant from the center of the sample than the transgranularly-cracked grains, and notably, the intergranular grains' radii were larger than that distance, indicating that those grains did not cross the center plane of the sample, while the transgranular grains did, and were thus closer to the direct path of the crack (Figure 4.12).

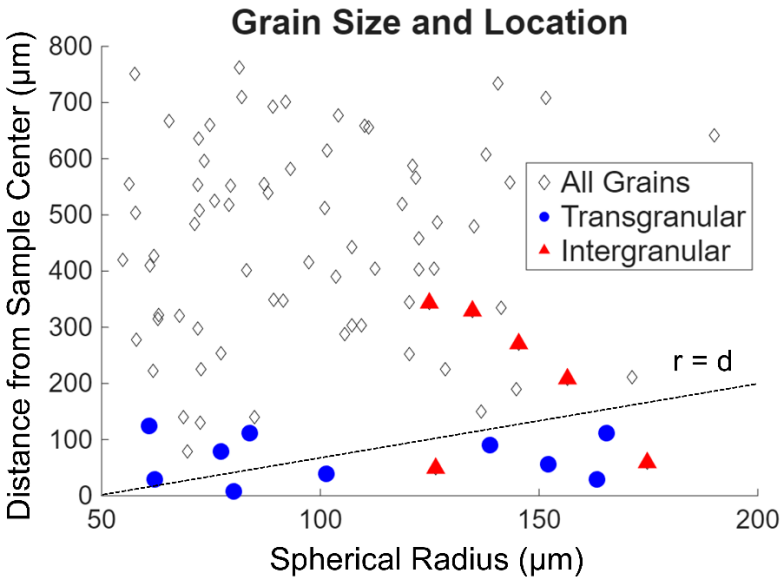

Figure 4.12: Radius of AlON grains versus the distance between their centers of mass and the center plane of the DCDC sample, with unity marked.

In addition to the gradual changes related to grain boundaries, there are smaller deflections present; most of these orientation changes occur over a range of a few to ten or so microns, and then straighten out again. Based on the fact that the crack does not sharply change its orientation to go around large grains, these deflections are presumed to occur near grain boundaries the crack is already growing near. Additional causes of deflection include rare pores, which have a fracture toughness of zero and are therefore preferential to pass through (Figure 4.13). Finally, the crack occasionally changes direction within grains,

potentially corresponding to stacking twinning faults not detected as a change in grain orientation by the techniques used, but also likely as part of the gradual angular changes induced by the microstructure ahead of the crack. Previous work has identified deflections when encountering both grain and twin boundaries, which often result in the crack kinking over the span of a few microns or less before continuing to grow in much the same direction and orientation as previously [38]. Some jaggedness and kinking are indeed visible in the crack in the tomography images (Figure 4.13), although at the scale of a micron or smaller this effect is at the spatial resolution limit and the size of the kink is subject to error. A similar effect can be seen at a grain boundary in Sample 1 (Figure 4.14), although the overall angle of the crack does not change overmuch. Notably, the crack plane is nearly parallel to the {100} direction in the first grain's unit lattice, which might have served as an attractive plane on which the crack could propagate. The degree of change between two different atomic arrangements could result in the crack being impeded from remaining on a single plane through both grains but the considerations above, the crack's tendency to become straighter as it extends deeper, and its speed when extending might have contributed to the crack maintaining a similar angle in both grains.

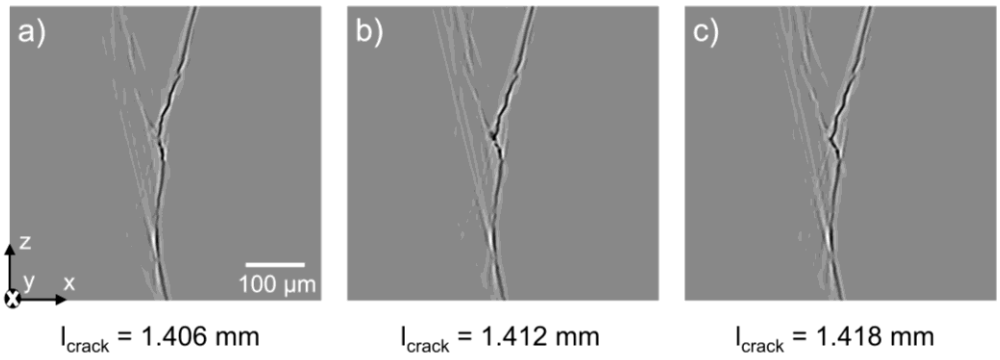

Figure 4.13: A pore interacting with the crack front (dark line) in Sample 4. The white streaks on the left side are wrinkle artifacts. a) Above the pore in the loading direction y, the crack has a mostly smooth curve with some jagged edges. b) The crack deflects to intersect the pore. c) After leaving the pore, the crack retains the sharp kink. Also visible near the deflection are changes in the crack direction between two orientations which are smaller than the diameter of a single grain, potentially indicating the crack is crossing twinning faults or other crystal discontinuities.

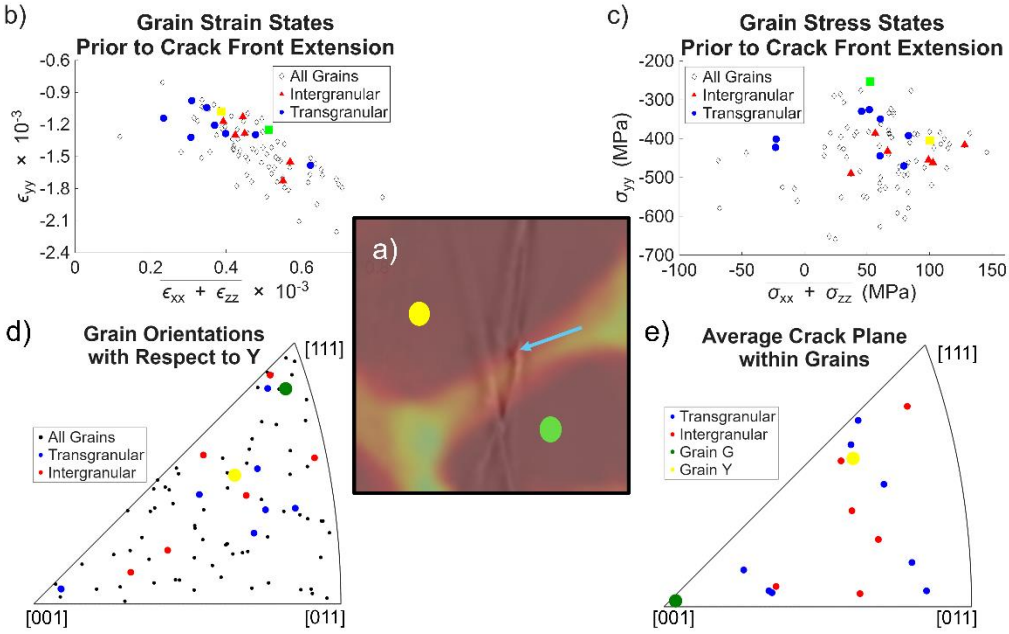

Figure 4.14: A kink at a grain boundary in Sample 1. a) Grain Y (yellow) and grain G (green) are both intersected transgranularly by the crack, but at the grain boundary, the crack gains a sharp kink (blue arrow). b-c) The values of strain and stress from Figure 4.10c-d), with the values for grains Y and G highlighted. d) The orientations of grains Y and G highlighted within the distribution from Figure 4.10a). e) The orientation of the crack normal within grains Y and G highlighted within the distribution from Figure 4.10b).

4.5 Conclusions

We have demonstrated that visualizing brittle fracture of a polycrystalline ceramic at multiple extension steps is possible using the DCDC geometry and the precise loading of RAMS-III fixture at the Advanced Photon Source. The information presented here demonstrates that this study's 3D, in-situ monitoring of a growing crack is superior to 2D and postmortem studies in capturing microstructural and stress-induced changes, including retardations in the crack's growth. We have shown that a 3D, growing crack can be complex, with an uneven crack front impacted by the microstructure ahead of the crack tip, the grain orientation, and the position of grain boundaries. Additionally, the high tomographic resolution of the crack's shape throughout the material and the registry of that shape to NF-HEDM scans are valuable pieces of information for phase-field modelers and others

performing computations seeking to describe the exact mechanisms affecting the crack's shape, length, and growth rate.

For AlON specifically, we have shown that the crack front extends in multiple pop-in-like events which may span a distance equivalent to a single grain along the crack front or many grains along its entire length. Further, additional pop-in events at the hole are possible, which may create a new crack front in a more favorable region for extending, and it may eventually surpass the original crack front. While the crack grows both intergranularly along grain boundaries and transgranularly with no preferred lattice planes, it may experience deflections in its orientation at grain boundaries and potentially at twinning faults. However, the grains through which the crack grew transgranularly and those beside which it grew intergranularly have no distinguishable or differing trends in orientation or stress state; rather, the grain only grew along grain boundaries when it was proximal to them while extending. Instead, the greater factor controlling growth is the changing fracture toughness of the region ahead of the crack as it encounters grains of different orientations. In regions of greater fracture toughness, the extension of the crack front is arrested until the load is increased sufficiently, after which it grows through regions of lower fracture toughness until its motion is again halted.

The information gathered from this work is extremely pertinent to building and verifying the above-mentioned phase-field models. Current collaborations have already produced results demonstrating crack pinning as observed in these experiments, and related pinning to the degrees of freedom of grain boundaries [34]. By selecting grain boundaries with singularity exponents that lead to crack pinning and computing the singularity in the stress for a crack tip at various grain boundaries, a corresponding increase in resistance to crack propagation is observed. In the future, we will be applying these insights to the experimental dataset to evaluate the performance of the model.

Future experimental work could be performed on anisotropic brittle materials with smaller grains in order to increase the number of grain boundaries, orientations, and stress states with which the crack interacts. By using materials with different crystal structures and degrees of anisotropy, trends not present in AlON might be uncovered. Further, recently-developed 2D scanning FF-HEDM using a point-focused beam, rather than the 1D scanning

performed here [40], could be used to resolve intragranular strain fields and better reveal the nature of the strain tensor ahead of the crack as well as any local changes within a grain which might cause it to kink or change orientation.

Acknowledgments

This work was sponsored by the US Office of Naval Research Grant No. N00014-21-1-2784. SFG was also supported by the US National Science Foundation Graduate Research Fellowship No. 2139433. Additionally, the authors would like to thank Dr. Paul Shade and the Air Force Research Laboratory for the generous use of RAMS-III. This research was performed on APS beam time award from the Advanced Photon Source, a U.S. Department of Energy (DOE) Office of Science user facility operated for the DOE Office of Science by Argonne National Laboratory under Contract No. DE-AC02-06CH11357.

Bibliography

[1] R.W. Armstrong, The influence of polycrystal grain size on several mechanical properties of materials, *Metall Trans* 1 (1970) 1169–1176. https://doi.org/10.1007/BF02900227.
[2] H.D. Espinosa, P.D. Zavattieri, A grain level model for the study of failure initiation and evolution in polycrystalline brittle materials. Part I: Theory and numerical implementation, *Mech Mater* 35 (2003) 333–364. https://doi.org/10.1016/S0167-6636(02)00285-5.
[3] N. Hansen, X. Huang, Microstructure and flow stress of polycrystals and single crystals, *Acta Mater* 46 (1998) 1827–1836. https://doi.org/10.1016/S1359-6454(97)00365-0.
[4] B. Chen, J.N. Hu, Y.Q. Wang, S.Y. Zhang, S. Van Petegem, A.C.F. Cocks, D.J. Smith, P.E.J. Flewitt, Role of the misfit stress between grains in the Bauschinger effect for a polycrystalline material, *Acta Mater* 85 (2015) 229–242. https://doi.org/10.1016/j.actamat.2014.11.021.
[5] T.J. Stannard, J.J. Williams, S.S. Singh, A.S. Sundaram Singaravelu, X. Xiao, N. Chawla, 3D time-resolved observations of corrosion and corrosion-fatigue crack initiation and growth in peak-aged Al 7075 using synchrotron X-ray tomography, *Corros Sci* 138 (2018) 340–352. https://doi.org/10.1016/j.corsci.2018.04.029.
[6] S.E. Gustafson, D.C. Pagan, P.A. Shade, M.D. Sangid, Dynamic recovery observed in distinct grains within a polycrystalline nickel-based superalloy during cyclic high temperature fatigue via high energy X-ray diffraction microscopy, *Scripta Mater* 192 (2021) 37–42. https://doi.org/10.1016/j.scriptamat.2020.10.004.
[7] J.V. Gordon, R.E. Lim, M.J. Wilkin, D.C. Pagan, R.A. Lebensohn, A.D. Rollett, Evaluating the grain-scale deformation behavior of a single-phase FCC high entropy alloy using synchrotron high energy diffraction microscopy, *Acta Mater* 215 (2021) 117120. https://doi.org/10.1016/j.actamat.2021.117120.
[8] W. Chen, J. Xu, C. Ding, D. Shan, B. Guo, T.G. Langdon, Fracture mechanism of electrically-assisted micro-tension in nanostructured titanium using synchrotron radiation X-ray tomography, *Scripta Mater* 222 (2023) 114997. https://doi.org/10.1016/j.scriptamat.2022.114997.
[9] H.R. Sandgren, Y. Zhai, D.A. Lados, P.A. Shade, J.C. Schuren, M.A. Groeber, P. Kenesei, A.G. Gavras, Characterization of fatigue crack growth behavior in LENS fabricated Ti-6Al-4V using high-energy synchrotron x-ray microtomography, *Addit Manuf* 12 (2016) 132–141. https://doi.org/10.1016/j.addma.2016.09.002.
[10] D.P. Naragani, P.A. Shade, P. Kenesei, H. Sharma, M.D. Sangid, X-ray characterization of the micromechanical response ahead of a propagating small fatigue crack in a Ni-based superalloy, *Acta Mater* 179 (2019) 342–359. https://doi.org/10.1016/j.actamat.2019.08.005.
[11] A.D. Spear, S.F. Li, J.F. Lind, R.M. Suter, A.R. Ingraffea, Three-dimensional characterization of microstructurally small fatigue-crack evolution using quantitative fractography combined with post-mortem X-ray tomography and high-energy X-ray diffraction microscopy, *Acta Mater* 76 (2014) 413–424. https://doi.org/10.1016/j.actamat.2014.05.021.

[12] M. Herbig, A. King, P. Reischig, H. Proudhon, E.M. Lauridsen, J. Marrow, J.-Y. Buffière, W. Ludwig, 3-D growth of a short fatigue crack within a polycrystalline microstructure studied using combined diffraction and phase-contrast X-ray tomography, *Acta Mater* 59 (2011) 590–601. https://doi.org/10.1016/j.actamat.2010.09.063.
[13] M.B. Cil, K.A. Alshibli, P. Kenesei, 3D Experimental Measurement of Lattice Strain and Fracture Behavior of Sand Particles Using Synchrotron X-Ray Diffraction and Tomography, *J Geotech Geoenviron* 143 (2017) 04017048. https://doi.org/10.1061/(ASCE)GT.1943-5606.0001737.
[14] J.W. McCauley, P. Patel, M. Chen, G. Gilde, E. Strassburger, B. Paliwal, K.T. Ramesh, D.P. Dandekar, AlON: A brief history of its emergence and evolution, *J Eur Ceram Soc* 29 (2009) 223–236. https://doi.org/10.1016/j.jeurceramsoc.2008.03.046.
[15] N.D. Corbin, Aluminum oxynitride spinel: A review, *J Eur Ceram Soc* 5 (1989) 143–154. https://doi.org/10.1016/0955-2219(89)90030-7.
[16] P.A. Shade, B. Blank, J.C. Schuren, T.J. Turner, P. Kenesei, K. Goetze, R.M. Suter, J.V. Bernier, S.F. Li, J. Lind, U. Lienert, J. Almer, A rotational and axial motion system load frame insert for in situ high energy x-ray studies, *Rev Sci Instrum* 86 (2015) 093902. https://doi.org/10.1063/1.4927855.
[17] H. Sharma, R.M. Huizenga, S.E. Offerman, A fast methodology to determine the characteristics of thousands of grains using three-dimensional X-ray diffraction. I. Overlapping diffraction peaks and parameters of the experimental setup, *J Appl Cryst* 45 (2012) 693–704. https://doi.org/10.1107/S0021889812025563.
[18] H. Sharma, R.M. Huizenga, S.E. Offerman, A fast methodology to determine the characteristics of thousands of grains using three-dimensional X-ray diffraction. II. Volume, centre-of-mass position, crystallographic orientation and strain state of grains, *J Appl Cryst* 45 (2012) 705–718. https://doi.org/10.1107/S0021889812025599.
[19] H. Sharma, marinerhemant/MIDAS, (2025). https://github.com/marinerhemant/MIDAS (accessed January 12, 2026).
[20] S. Satapathy, M. Ahart, D. Dandekar, R.J. Hemley, B. Schuster, P. Khoma, Single-Crystal Elastic Properties of Aluminum Oxynitride (AlON) from Brillouin Scattering, *J Amer Ceram Soc* 99 (2016) 1383–1389. https://doi.org/10.1111/jace.14065.
[21] S.D. Shastri, J. Almer, C. Ribbing, B. Cederström, High-energy X-ray optics with silicon saw-tooth refractive lenses, *J Synchrotron Rad* 14 (2007) 204–211. https://doi.org/10.1107/S0909049507003962.
[22] S.D. Shastri, P. Kenesei, A. Mashayekhi, P.A. Shade, Focusing with saw-tooth refractive lenses at a high-energy X-ray beamline, *J Synchrotron Rad* 27 (2020) 590–598. https://doi.org/10.1107/S1600577520003665.
[23] B.A. Dowd, G.H. Campbell, R.B. Marr, V.V. Nagarkar, S.V. Tipnis, L. Axe, D.P. Siddons, Developments in synchrotron x-ray computed microtomography at the National Synchrotron Light Source, in: Developments in X-Ray Tomography II, SPIE, 1999: pp. 224–236. https://doi.org/10.1117/12.363725.
[24] A. Buades, B. Coll, J.-M. Morel, Non-local means denoising, *Image Processing On Line* 1 (2011) 208–212. https://doi.org/10.5201/ipol.2011.bcm_nlm.
[25] Continuum aspects of crack propagation I: linear elastic crack-tip field, in: Fracture of Brittle Solids, 2nd ed., Cambridge University Press, Cambridge, 1993: pp. 16–50. https://doi.org/10.1017/CBO9780511623127.

[26] C. Xiao, J.-Y. Buffière, J.M. Létang, W. Ludwig, Investigation of wrinkle artifacts along metallic fatigue cracks in phase contrast synchrotron tomography via simulations and experiments, *Mater Charact* 194 (2022) 112431. https://doi.org/10.1016/j.matchar.2022.112431.
[27] J.K. Kurihara, T. Tomimatsu, Y.F. Liu, S.Q. Guo, Y. Kagawa, Mode I fracture toughness of SiC particle-dispersed ZrB2 matrix composite measured using DCDC specimen, *Ceram Int* 36 (2010) 381–384. https://doi.org/10.1016/j.ceramint.2009.07.031.
[28] B. Cotterell, On brittle fracture paths, *Int J Fract* 1 (1965) 96–103. https://doi.org/10.1007/BF00186747.
[29] T. Fett, G. Rizzi, J.P. Guin, J.M. López-Cepero, S.M. Wiederhorn, A fracture mechanics analysis of the double cleavage drilled compression test specimen, *Eng Fract Mech* 76 (2009) 921–934. https://doi.org/10.1016/j.engfracmech.2008.12.016.
[30] C. Nielsen, A.V. Amirkhizi, S. Nemat-Nasser, The effect of geometry on fracture strength measurement using DCDC samples, *Eng Fract Mech* 91 (2012) 1–13. https://doi.org/10.1016/j.engfracmech.2012.04.030.
[31] J.A. Salem, Crack Growth Testing of an Aluminum Oxynitride (AlON) for International Space Station Kick Panes, 2017. https://ntrs.nasa.gov/citations/20170001289 (accessed May 31, 2025).
[32] J.J. Guo, K. Wang, T. Fujita, J.W. McCauley, J.P. Singh, M.W. Chen, Nanoindentation characterization of deformation and failure of aluminum oxynitride, *Acta Mater 59* (2011) 1671–1679. https://doi.org/10.1016/j.actamat.2010.11.034.
[33] T.A. Michalske, W.L. Smith, E.P. Chen, Stress intensity calibration for the double cleavage drilled compression specimen, *Eng Fract Mech* 45 (1993) 637–642. https://doi.org/10.1016/0013-7944(93)90269-X.
[34] M. Ramesh, Phase-Field Modeling of Fracture in Heterogeneous Materials: A Microstructure Sensitive Approach, Northwestern University, 2025.
[35] M.Y. He, M.R. Turner, A.G. Evans, Analysis of the double cleavage drilled compression specimen for interface fracture energy measurements over a range of mode mixities, *Acta Metall Mater* 43 (1995) 3453–3458. https://doi.org/10.1016/0956-7151(95)00036-U.
[36] H.X. Willems, P.F. Van Hal, G. De With, R. Metselaar, Mechanical properties of γ-aluminium oxynitride, *J Mater Sci* 28 (1993) 6185–6189. https://doi.org/10.1007/BF00365041.
[37] Q.Z. Wang, M. Ni, L.Z. Wu, R.Q. Huang, Scrutinized and revised stress intensity factor formulas for double cleavage drilled compression specimens, *Theor Appl Fract Mec* 96 (2018) 803–810. https://doi.org/10.1016/j.tafmec.2017.11.008.
[38] M. Ding, T. Wang, B. Maerz, S. Robertson, Z. Sun, L. Fan, Y. Shi, H. Wu, Formation of twins in AlON material and its effects on the Vickers hardness and fracture toughness, *Ceram Int* 45 (2019) 21127–21135. https://doi.org/10.1016/j.ceramint.2019.07.089.
[39] C.K. Cocke, A. Akerson, S.F. Gorske, K.T. Faber, K. Bhattacharya, On recovering intragranular strain fields from grain-averaged strains obtained by high-energy X-ray diffraction microscopy, *Math Mech Solids* 31 (2026) 122–139. https://doi.org/10.1177/10812865251376693.
[40] W. Li, H. Sharma, P. Kenesei, S. Ravi, H. Sehitoglu, A. Bucsek, Resolving intragranular stress fields in plastically deformed titanium using point-focused high-energy

diffraction microscopy, *J Mater Res* 38 (2023) 165–178. https://doi.org/10.1557/s43578-022-00873-y.

Chapter 5

BREAKING FREE: EXTENDING THE ALUMINUM OXYNITRIDE EXPERIMENTS WITH TESSELLATED DATA

Sections of this chapter will be published in a forthcoming publication: **Gorske, S.F.**, Bhattacharya, K., Voorhees, P., Faber, K.T. "Grain ensemble effects on brittle crack propagation using Voronoi-Laguerre tessellations verified against real microstructures." In preparation.

5.1 Introduction

In the DCDC AlON samples of Chapter 4, neither the grain orientations nor the grain-averaged stresses are sure indicators of whether a crack will pass transgranularly through the grain or bypass it intergranularly. However, these parameters still have an impact on the sample's fracture toughness, and as seen in the two samples examined in the previous chapter, that value can change within and between samples as the grain configuration changes (Figure 4.11). As fracture toughness is calculated partly with the length of a crack, the grains just ahead of a crack after its motion has been arrested are a primary factor in obtaining that value. Determining how the grains in the volume ahead of the crack differ from those which the grain passed through unhindered should reveal more information on how the arrangement of grains of different sizes and orientations impacts the stress and strain states in those volumes, as well as the energy needed for the crack to progress through that region.

However, obtaining NF-HEDM maps of grain volumes and boundaries throughout an entire sample is not feasible. In the setup used for the AlON samples at Beamline 1-ID at the APS, a single NF-HEDM scan takes around 18 minutes, and the step size between scans was 5 μm. In contrast, one FF-HEDM scan takes around 7 minutes, and the beam size was 100 μm. In order to collect data at multiple stages of fracture, a balance must be struck between the number of scans performed and the time data collection takes. As a result, NF-HEDM

data does not cover the entirety of most regions of interest, and the grain structure cannot be exactly determined everywhere.

Fortunately, FF-HEDM data contains some of the same information as NF-HEDM, primarily grain orientation, center-of-mass, and approximate spherical radius. In many experiments, NF-HEDM is not performed at all, and tessellations are created using FF-HEDM to be used as approximate grain maps [1–4]. When examining suites of grains for average volumetric properties, this can often be a sufficient and efficient experimental design.

When considering transgranular versus intergranular fracture, as well as the question of which grains and grain boundaries arrested a crack's motion, however, the location of those grain boundaries must be accounted for. As such, using a tessellation as a grain map requires a more robust and experimentally-verified method to recreate the grain structure. The first part of this chapter will be concerned with testing various FF-HEDM tessellation creation methods against NF-HEDM ground truth maps, both from the AlON samples described in Chapter 4. Following the selection of one method, the second part of the chapter will examine what the tessellations reveal about the crack's interaction with AlON grains beyond the results of the previous chapter.

5.2 Methods: Creating and verifying HEDM tessellations

5.2.1 Mathematical basis: Voronoi and Laguerre-Voronoi tessellations

The simplest form of tessellation is a Voronoi tessellation, requiring only a set of points to be used as centroids for the tessellated structure within the region of interest. The tessellation is formally defined in Equation 5.1 [5].

$$\widehat{V_i} = \{\boldsymbol{x} \in W \mid |\boldsymbol{x} - \boldsymbol{z_i}| \leq |\boldsymbol{x} - \boldsymbol{z_j}| \text{ for } j = 1, \dots, k, j \neq i\} \quad \text{Equation 5.1}$$

$\{\boldsymbol{z_i}\}_{i=1}^{k}$ = centroids W = discrete set of points in volume of interest

Essentially, the tessellation can be created by assigning each discrete point in the volume of interest to the set for which the centroid is closer to that point than any other set's centroid. When the given centroids are well-dispersed in the volume, and when the sets (or grains, in

this case) are known to have similar volumes, this approximation can work well to define the division of the larger volume into grains; however, it is limited when greater variability and irregularity is present in the grains' sizes and shapes [2,6]. Accordingly, a Laguerre-Voronoi tessellation can be defined (Equation 5.2), which minimizes a value known as the power-distance, d_L (Equation 5.3) instead of $|\boldsymbol{x} - \boldsymbol{z_j}|$ [2]. By introducing a weight which decreases the power-distance more for larger values of the weight, the size of the set assigned to grains with larger weights is thereby larger, making the power-distance an effective proxy for grain size. The weight in the power-distance is sometimes interpreted as being related to the square of the radius of the set [2].

$$\widehat{V_i} = \{\boldsymbol{x} \in W \mid d_L(\boldsymbol{x}, \boldsymbol{z_i}, w_i) \leq d_L(\boldsymbol{x}, \boldsymbol{z_j}, w_j) \text{ for } j = 1, \ldots, k, j \neq i\} \quad \text{Equation 5.2}$$

$$d_L(\boldsymbol{x}, \boldsymbol{z_i}, w_i) = |\boldsymbol{x} - \boldsymbol{z_i}|^2 - w_i \quad \text{Equation 5.3}$$

5.2.2 Using FF-HEDM data in the Laguerre-Voronoi tessellation

The FF-HEDM data provides for every grain in the interrogated volume both the centers-of-mass and radii (calculated for a sphere of equivalent volume to the grain volume illuminated by the X-ray beam). When both NF-HEDM and FF-HEDM datasets exist for a given volume, a tessellation using the FF-HEDM information can be registered against the NF-HEDM grain map to determine its accuracy. In the AlON Sample 1, described in Chapter 4, three coincident NF-HEDM and FF-HEDM datasets (Table 5.1) were collected and used to optimize the tessellation methods described in the following sections. Two metrics were used to examine the tessellations: the first was the number of total points assigned to the same grain between the tessellation and the ground truth, while the second was the number of points with a NF-HEDM confidence value greater than 80% which matched between the two datasets. This second metric was used because near grain boundaries, the confidence level drops, and the observed boundary is much less clean than an actual grain boundary in AlON, which is expected to be near-planar. Thus, the percentage of matching points is expected to be low in those regions where the assigned grain may not be correct anyway, which could skew results. Figure 5.1a shows a sample NF-HEDM grain map, with the points

with 80% or greater confidence shown in Figure 5.1b, showing much clearer grain shapes but without clear grain boundaries.

Table 5.1: Description of the FF-HEDM and NF-HEDM volumes used for tessellation optimization.

	Load (N)	FF-HEDM volume	NF-HEDM volume	Percentage of points with >80% confidence
Volume 1	-1100	A×300 μm	A×250 μm	65.73%
Volume 2	-1700	A×500 μm	A×300 μm	54.72%
Volume 3	-1740	A×700 μm	A×105 μm	68.17%

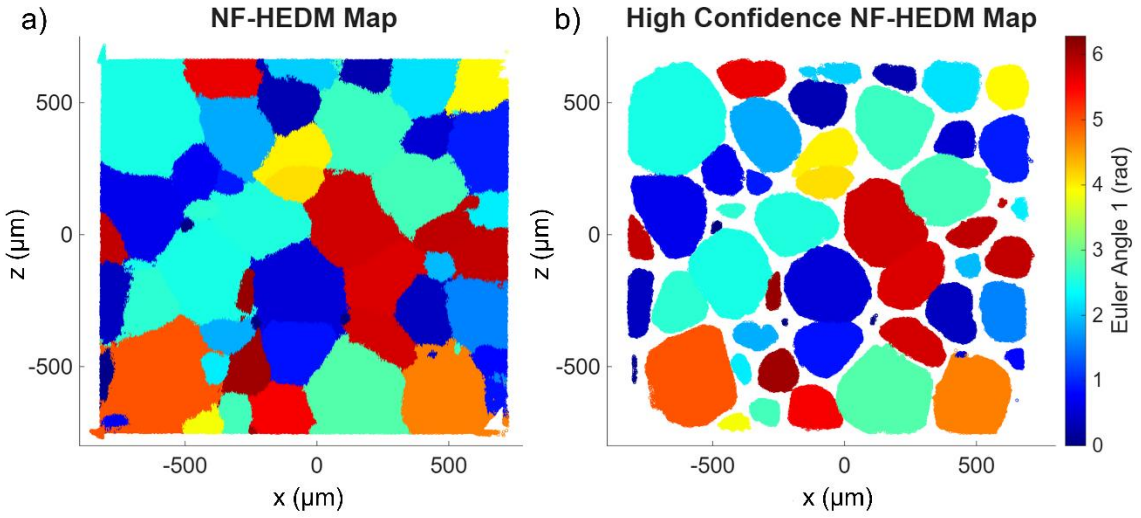

Figure 5.1: a) Near-field HEDM grain map from Volume 2 in Sample 1, colored by the first Euler angle. b) The map in a) with only points having a confidence value of 80% included, showing grain shapes without uncertain grain boundaries.

By substituting the centers-of-mass for the centroids in Equation 5.1, the basic Voronoi tessellation can be created. For the Laguerre-Voronoi tessellation, the spherical radius can then be used in creating the weight in the equation for the power-distance, but w_i does not necessarily have to equal r_i^2, and may have additional factors determining its value.

Two different versions of the power-distance were tested as a first step. Equation 5.4 is similar to Equation 5.3, with the square of the radius having an additional weight factor that

was probed at multiple values. Equation 5.5, meanwhile uses the square root of both the $|\boldsymbol{x} - \boldsymbol{z_j}|^2$ term and the r_i^2 term, while also weighting the radius to various extents.

$$d_L(\boldsymbol{x}, \boldsymbol{z_i}, w_i) = |\boldsymbol{x} - \boldsymbol{z_i}|^2 - b \cdot r_i^2 \qquad \text{Equation 5.4}$$

$$d_L(\boldsymbol{x}, \boldsymbol{z_i}, w_i) = |\boldsymbol{x} - \boldsymbol{z_i}| - b \cdot r_i \qquad \text{Equation 5.5}$$

The results for how well the tessellations matched the NF-HEDM ground truth are shown in Figure 5.2, indicating that for all the studied volumes, Equation 5.5 reached a greater maximum match percentage, achieved when the radius weight b had a value of around 1.25. The maximum values are reported in Table 5.2.

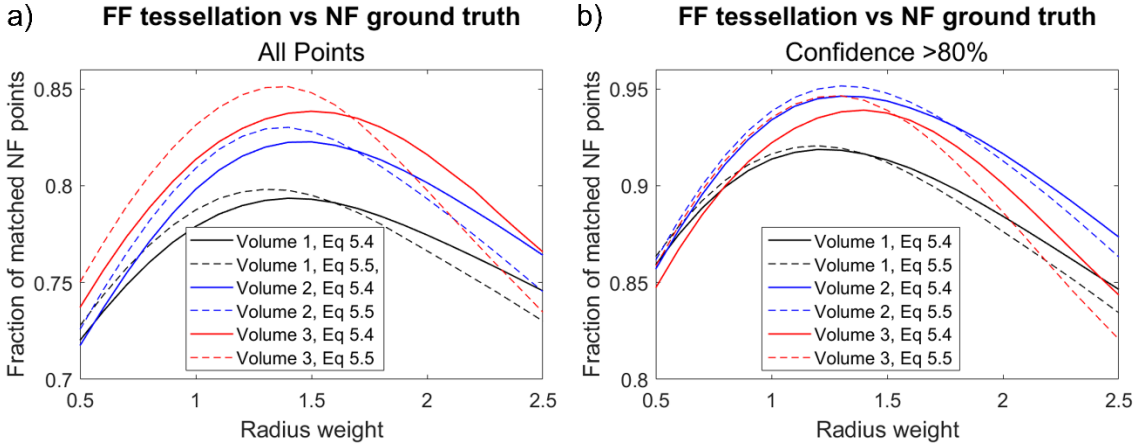

Figure 5.2: Results from Equations 5.4 and 5.5. a) Fraction of points attributed to the same grain as the equivalent NF-HEDM point, as a function of radius weight b. b) Fraction of correctly identified points using only NF-HEDM points with confidence >80%.

Table 5.2: Maximum percentage of ground truth NF-HEDM grain IDs matched by FF-HEDM tessellations using Equation 5.5.

	radius weight *b*	**Percentage of matched NF points**	**Percentage of matched NF points in confident regions**
Volume 1	1.2	79.68%	92.06%
Volume 2	1.3	83.01%	95.15%
Volume 3	1.3	85.11%	94.64%

5.2.3 Adjusting for orientation effects

While adjusting the power-distance based on grain radius allows size effects to be included, the value of the power-distance for a given grain is constant at all equivalent distances from the grain centroid, and grains are not entirely spherical. While a tessellation does introduce planar boundaries between grains reminiscent of real grain boundaries, impingement is not the only factor in determining where those grain boundaries will lie for most materials. Just as different planar arrangements of grains diffract at different angles, so too do those arrangements, with their unique spacings between sets of atoms, have different surface energies due to the atomic densities on the free surface [7]. As noted in Chapter 2, surface energy plays an important role in fracture, including the planes on which fracture is more energetically favorable. It also influences grain growth, as surfaces with lower surface energy can grow to larger areas when there are no other restrictions on where a grain can grow; minimizing the entire surface of a free grain results in a polyhedron with faces corresponding to the lowest surface-energy plane in that orientation.

While the surface energies of different planes for many elements and simple materials have been estimated, calculated, and tested [8], AlON does not have the same type of available data. For metals with the same face-centered cubic (FCC) structure as AlON, various analyses have been performed which have concluded that the {111} planes have the lowest energy of any surface, followed by the {100} plane, and thus these two plane families dominate the resultant grain shape (Figure 5.3) [7,9,10]. Thus, in the <111> directions, those grains might grow larger than the average radius of the grain, while in other directions the radius might be smaller.

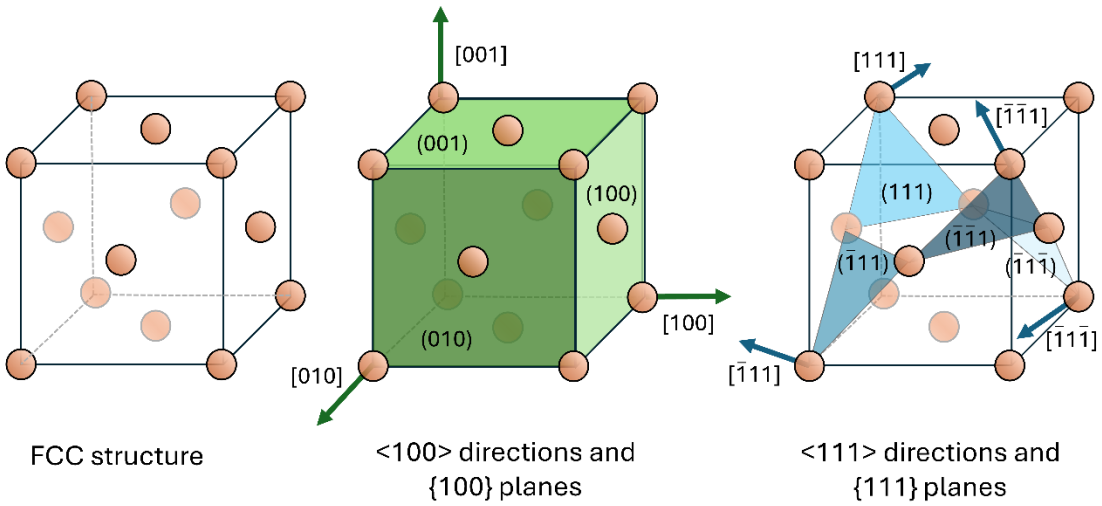

Figure 5.3: The face-centered cubic (FCC) structure, with the <100> and <111> directions and {100} and {111} planes pictured. For each set of directions and planes, the negative is also part of the same family but is not pictured for clarity.

To incorporate this aspect of real grains into the tessellation and the power-distance, the direction and distance of each point to each centroid in the tessellation was converted into a series of vectors. The orientation of that vector with respect to each grain's unit cell was then determined, then it was compared to the <100> and <111> vectors and the angles between them computed (Equations 5.6-7). Then an additional weighting factor was added to the power-distance based on the angular proximity to the two extremes. Since the <100> family has six equivalent directions, and the <111> family has eight, the closest vectors from each family, that is, those with the smallest angle between them and the location vector, were used for this calculation (Equation 5.8), which was then substituted into Equation 5.5 in place of w_i.

$$\boldsymbol{v} = \boldsymbol{Q}^{\boldsymbol{T}}|\boldsymbol{x} - \boldsymbol{z_i}| \qquad \text{Equation 5.6}$$

$$\theta = \cos^{-1}\frac{\hat{\boldsymbol{e}} \cdot \boldsymbol{v}}{\|\hat{\boldsymbol{e}}\|\|\boldsymbol{v}\|} \qquad \text{Equation 5.7}$$

$$w_i = b \cdot r_i\left(\frac{\theta_{\langle 111\rangle}(1-p) + \theta_{\langle 100\rangle}(1+p)}{\theta_{\langle 111\rangle} + \theta_{\langle 100\rangle}}\right) \qquad \text{Equation 5.8}$$

$\hat{\boldsymbol{e}}$ = unit vector for direction in grain (<100> or <111>)

$\boldsymbol{Q}^{T}$ = rotation matrix (grain reference frame to sample reference frame)

θ = angle between vectors

p = relative change in radius

A range of values for b and p were tested while substituting Equation 5.8 for $b \cdot r_i$ in Equation 5.5, with results shown in Figure 5.4. Negative values for p correspond to the <100> directions having a larger radius, as $\theta_{<100>}$ will be smaller than $\theta_{<111>}$ for directions closer to the <100> pole, while the <111> directions are weighted more heavily for positive values of p.

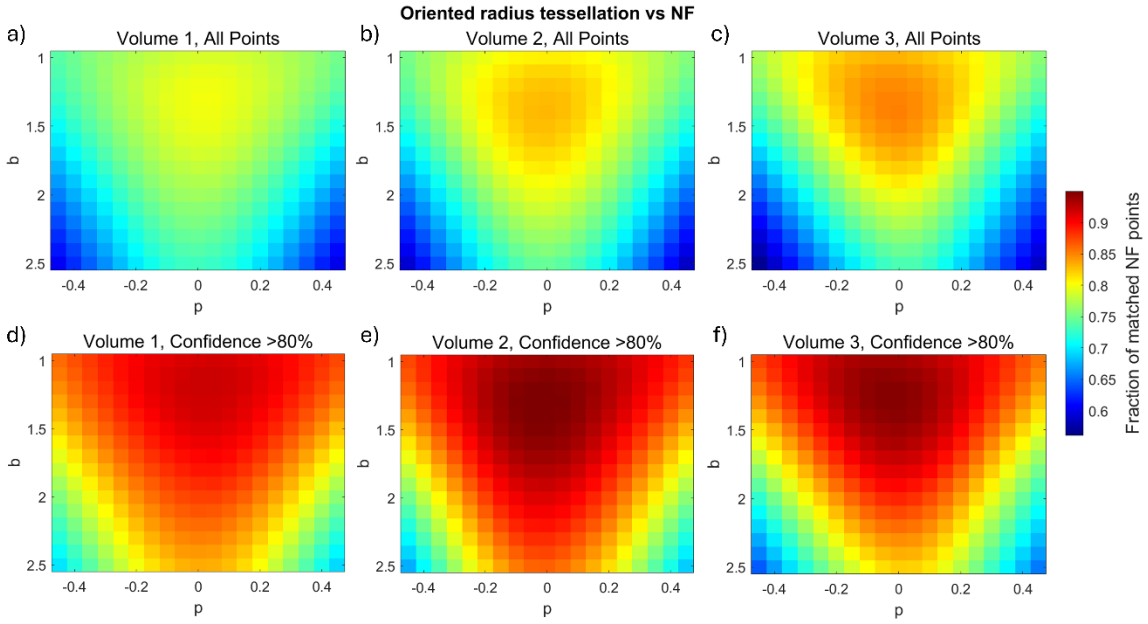

Figure 5.4: Results from using Equation 5.8 as the weighted factor in Equation 5.5.

As seen in Figure 5.4, the match between the tessellation and the NF-HEDM results for all volumes is maximized for some b when $p = 0$. For $p = 0$, $w_i = b \cdot r_i$ and thus the result is unchanged from Equation 5.5 and the results tabulated in Table 5.2. Therefore, either the {100} and {111} faces have very similar surface energies in AlON, or any difference in directional growth for the grains is already accounted for by the distribution of the centroids in space.

5.2.4 Adjusting for volume effects

One shortcoming of HEDM in tracking grains is that data is only reported for the illuminated volumes. Thus, the reported centers-of-mass are really the centers-of-mass for the section of the grain in a specific volume, and the true centroids of grains which extend beyond the top and bottom layers of the scans will be more distant from the center of the interrogated volume than reported. This fact is likely why, in Figure 5.2 and Table 5.2, Volumes 2 and 3 have greater match percentages between the tessellations and NF-HEDM data; the FF-HEDM data for those scans extended beyond the edges of the NF-HEDM volume (Table 5.1), and so data from beyond the region of interest is used, including grain centroids from outside that volume. When creating tessellations for the entire volume of a set of FF-HEDM scans, however, this effect will be lost. Furthermore, because the radius reported by HEDM is calculated using only the illuminated volumes, grains on the edges of the volume will actually have larger radii than shown in the data. Additionally, grains on the edges of a sample can be artificially cut off as a result of processing, skewing their shape; the original grain's centroid and radius will also be shifted from the HEDM values.

Adjusting the centroids presents the issue that the direction between the true and reported values is unknown; perturbing it at random in its three directions of freedom might bring the tessellation closer to the actual grain structure, but doing so might also worsen the match. As such, it will not be adjusted in the method presented here. The radius, however, can be more easily perturbed, since as a scalar it has a single degree of freedom and the direction of perturbation should be an increase for those grains missing parts of their volume.

Checking the tessellation from Equation 5.5 for any grains which lie on the edge in order to adjust their radii is unnecessarily time-consuming, as it would potentially result in an iterative process as tessellated grains are moved toward and away from the boundaries of the illuminated volume. Accordingly, the weighted radii used in Equation 5.5 can simply be adjusted based on the distance of each grain's centroid to the center of the overall volume (Equation 5.9).

$$b_i = s \cdot \frac{d_i}{d_{max}} + b_0 \qquad \text{Equation 5.9}$$

s = span between largest and smallest b_i | d_i = distance of centroid i to illuminated volume center | b_0 = smallest b_i | d_{max} = distance of sample corner to illuminated volume center

Adjusting the span of weights s that can be assigned to the power-distance and the minimum weight b_0 provides many opportunities for tailoring the tessellation. Since the match between the NF-HEDM maps and the tessellation from Equation 5.5 was maximized in the range of b = 1.2-1.3, including that value in the range b_i can take is sensible. A variety of spans ranging from 0 to 1 were tested, and both the overall match percentage and the percentage in the confident regions were increased for all volumes (Figure 5.5, Table 5.3) when s was set to 0.25 and b_0 was set to 1.25, meaning that the range of values b_i can take goes from 1.25 for a centroid at the center of the illuminated volume to 1.5 at a sample corner.

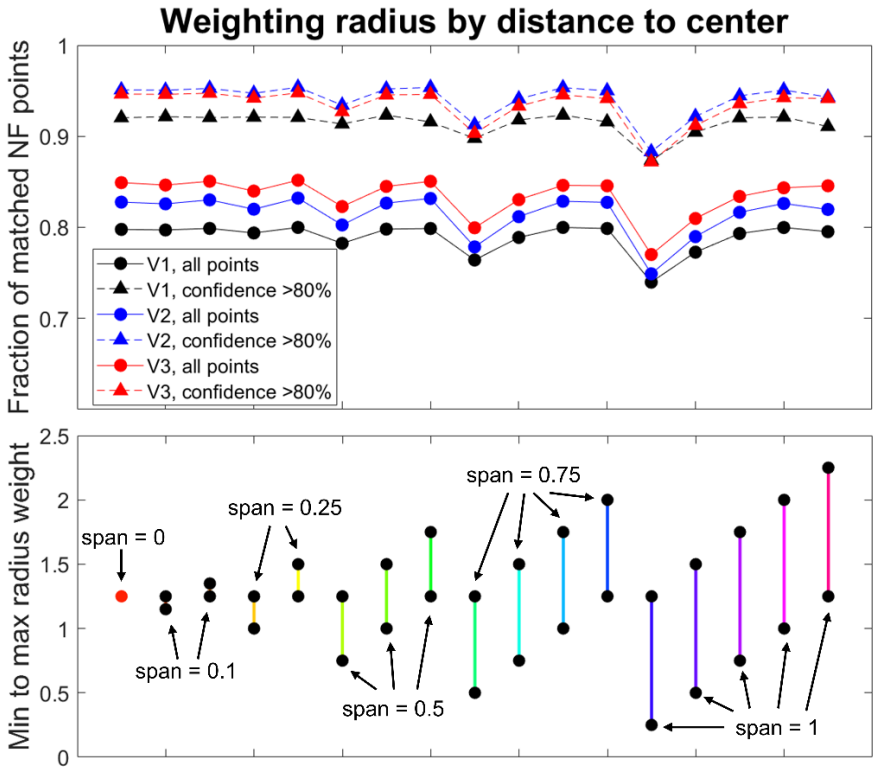

Figure 5.5: Results when the tessellation of Equation 5.5 is modified by Equation 5.9 so that the weight b_i on the radius r_i in the modified power-distance is determined by the distance of the centroid z_i to the center of the illuminated volume. At the center of the volume, b_i equals the minimum value of the range, shown in the bottom half of the figure, and it equals the maximum at the sample corner. The results for the verification of the tessellation against the ground truth NF-HEDM scans are reported at the top.

Table 5.3: The percentage match between the NF-HEDM grain maps and the FF-HEDM tessellation created by Equations 5.5 and 5.9, along with the increase in match percentage from the unmodified Equation 5.5. For Equation 5.9, $s = 0.25$ and $b_0 = 1.25$.

	Percentage of matched NF points	**Increase in percentage matched from Table 5.2**	**Percentage of matched NF points in confident regions**	**Increase in confident percentage matched vs Table 5.2**
Volume 1	79.99%	0.22%	92.07%	0.04%
Volume 2	83.21%	0.44%	95.39%	0.29%
Volume 3	85.17%	0.26%	94.77%	0.13%

While the increase in match percentage is modest, the fact that the increase was present among all tested volumes despite their different sizes demonstrates potential for this approach.

5.2.5 Using sub-granular FF-HEDM data

In the AlON experiments, the FF-HEDM scans were taken 100 μm apart. However, many of the grains were larger in diameter than that distance, meaning they spanned two or more FF-HEDM layers, and values for the centroid, radius, and stress tensor were calculated for each local volume. Using this sub-granular data is therefore considered here as an alternative way to formulate the tessellations, which might allow non-spherical and asymmetrically shaped grains to be better matched in space.

First, the centroids for each sub-granular volume were assumed to lie along a linear path (Figure 5.6a). Calculating a first-order line of best fit is trivial, and equations were created to track x and z as functions of y, the direction in which the sample was moved to take subsequent scans. Thus, the tessellation can be divided into any number of 2D slices in the y direction and a centroid for that slice can be calculated (Figure 5.6b).

Similarly, an equation for the radius as a function of y was created. It is assumed that the grain's volume, and consequently the reported radius, is maximized in its center (Figure 5.6a). In order for the equation to reach a single maximum, and for it to remain concave everywhere, a parabolic fit is used (Figure 5.6b). Since most of the AlON grains have radii smaller than 200 μm, very few should appear in more than three FF-HEDM scan volumes, so a fit of greater power is prohibited anyway.

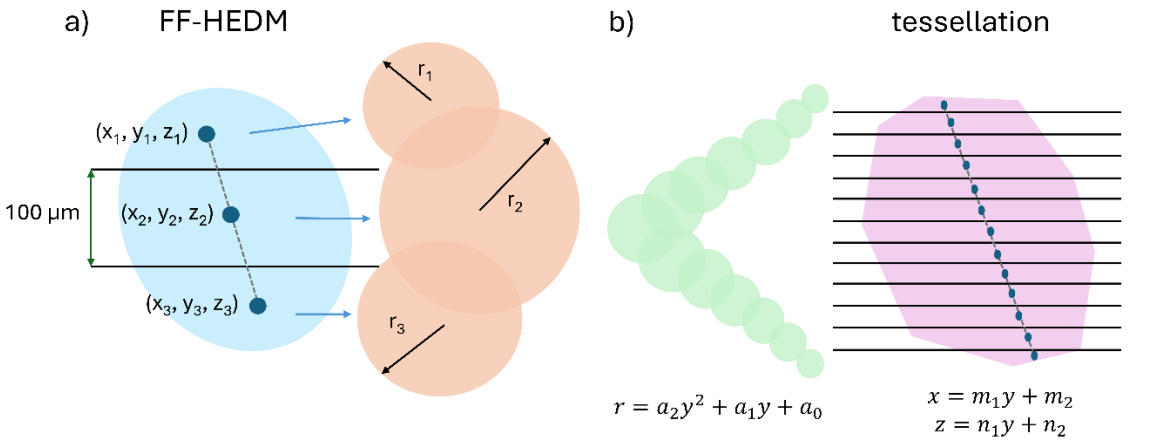

Figure 5.6: Using sub-granular FF-HEDM information to construct a series of 2D tessellations. a) Each FF-HEDM scan reports a center-of-mass and radius for each scan volume. b) By creating equations for x, z, and r in y, arbitrarily many 2D slices can be made in the volume, each with a value for x, z, and r.

For grains in only two volumes, two possible cases exist: first, that the grain is cut off by the edge of the FF-HEDM volume, and second, that it is fully contained within the volume. To determine which case each grain fell into, the conditions in Table 5.4 were used. If all conditions were satisfied, the grain was guessed to have part of its volume lying outside the FF-HEDM volume.

Table 5.4: Conditions for determining if part of a grain's volume lies outside the scanned FF-HEDM volume.

Condition	Reasoning
One sub-granular volume must be present in top or bottom FF-HEDM scan.	The grain must be on the edge of the FF-HEDM volume.
The sub-granular radius from the edge scan must be bigger than that from the inner scan.	If the grain radius is decreasing, the centroid is within the FF-HEDM volume already.
Both sub-granular radii must be greater than the scan height (100 µm).	The cumulative volumetric radius indicates a diameter greater than the height of two scans.

The grains with one or two FF-HEDM presences then had to have additional center-of-mass and radius values manufactured in order for the fits to be created, according to Figure 5.7 and Table 5.5. Two-datapoint grains determined to be interior to the FF-HEDM volume were assigned a point midway between the two existing *y* values with a radius calculated from the combined spherical volume of the existing datapoints. For the edge grains, since it cannot be determined how much grain volume might lie outside the FF-HEDM volume, and since most grains are not present across more than three sub-volumes, only one external value was added to those grains with two datapoints, and was equal to the smaller radius at a *y*-position mirrored across the *y*-position closer to the volume edge. Grains present in a single sub-volume could not be determined as having additional volume outside the scanned volume, and were assigned additional radius and *y* values corresponding to a sphere centered at the existing datapoint. The *x* and *z* positions for the linear fit were made to be constant and independent of *y*.

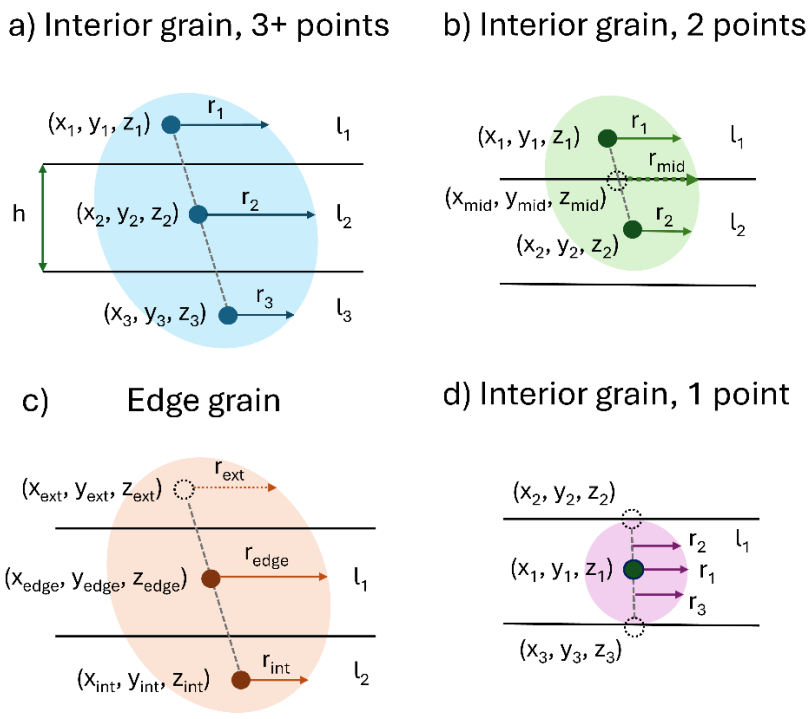

Figure 5.7: Possibilities for how grains present in FF-HEDM, and how the 2D-slice tessellations described in Table 5.4 can be created for each.

Table 5.5: Criteria and calculations for adding additional points to FF-HEDM grains in order to calculate polynomial fits.

Criterion	Radius Equation	*y* Equation
2 points, fully within FF-HEDM volume	$r_{mid} = \sqrt[3]{r_1^3 + r_2^3}$	$y_{mid} = \frac{y_1 + y_2}{2}$
2 points, grain bisected by edge	$r_{ext} = r_{int}$	$y_{ext} = 2y_{edge} - y_{int}$
1 point	$r_2 = r_3 = \frac{\sqrt{3}}{2} r_1$	$y_2 = y_1 - \frac{r_1}{2}$ $y_3 = y_1 + \frac{r_1}{2}$

Once the radius, and center-of-mass for every grain could be calculated based on *y*-position, tessellations could be made according to Equation 5.5, but with a separate calculation for each *y*-position of interest. Additionally, if the radius for a certain grain in a certain 2D slice would be negative, its value was set to zero and the center-of-mass for that grain was placed far outside the region of interest, so it would not be at risk of minimizing the power-distance. Results are shown in Figure 5.8. contrasted against the results from using Equation 5.5 and Figure 5.2 in its 3D form, the latter of which is shown to perform better both for the set of all NF-HEDM points and the set of confident points.

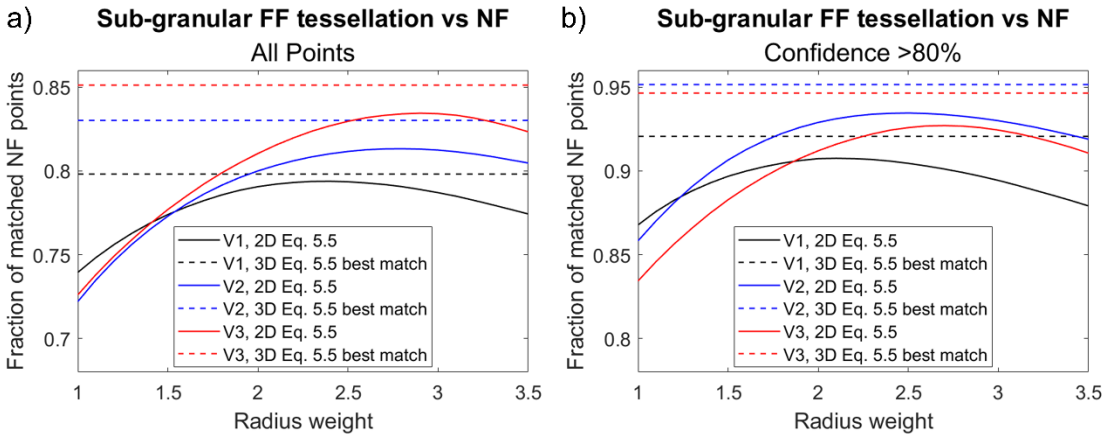

Figure 5.8: Results from making 2D-slice tessellations using Equation 5.5 and sub-granular FF-HEDM data as presented in Figure 5.6-7 and Tables 5.4-5. The best results for each volume from the 3D tessellation using Equation 5.5 are also shown for comparison, and show that the 3D tessellation is a better match for all volumes and confidence levels.

5.2.6 Correcting for volume mismatches

An additional piece of information that can be obtained from FF-HEDM and used independently of NF-HEDM is the overall grain volume. Exact volume matches are not generally possible, since the FF-HEDM volumes, and therefore the sub-granular volumes, usually do not exactly overlap with the NF-HEDM volumes, as seen in Table 5.1. However, the relative volume of a grain within the FF-HEDM volume can be compared to its relative volume in the tessellation (Equation 5.10).

$$\Delta V_i = \frac{V_{i,ff}}{\sum_{j=0}^{n} V_{j,ff}} - \frac{V_{i,tess}}{\sum_{j=0}^{n} V_{j,tess}} \qquad \text{Equation 5.10}$$

An iterative procedure was performed using this information. The grain boundaries in the tessellation along the x, y, or z direction were found, and the ΔV's of the grains on either side compared. If both had the same sign, then nothing was done. If they had opposite signs, this indicated that one tessellated grain was smaller than its FF-HEDM counterpart (positive ΔV), while one was larger (negative ΔV). The boundary was then changed by one voxel for every point along the boundary, increasing the too-small grain's volume and decreasing the larger grain's volume. The procedure was repeated for the other two orthogonal directions. All three directions could then be iterated over an arbitrary number of times until the average of the ΔV's neared zero.

Results are shown in Figure 5.9. While the match for Volume 1 increases very slightly with two iterations, overall it does not change very much, while the matches for Volumes 2 and 3 become increasingly worse. This is likely because of the difference in size between the FF-HEDM and NF-HEDM volumes (Table 5.1); while the sizes are similar for Volume 1, meaning that the relative grain sizes are roughly accurate, the data for Volumes 2 and 3 extend beyond the borders of their respective NF-HEDM volumes, meaning that the relative grain volumes are quite different between the NF-HEDM-sized tessellations and FF-HEDM. As a result, iterating causes grains extending beyond the upper and lower bounds of the volume, which have a lesser contribution to the NF-HEDM volume than the FF-HEDM volume, to grow into regions where they should only have minimal presence. When creating a tessellation with no ground truth, extending the full volume of an FF-HEDM dataset, this

error may be mitigated, but without an appropriate dataset for comparison, the conclusion is to use the original tessellation without attempting to correct the grain-volume mismatches.

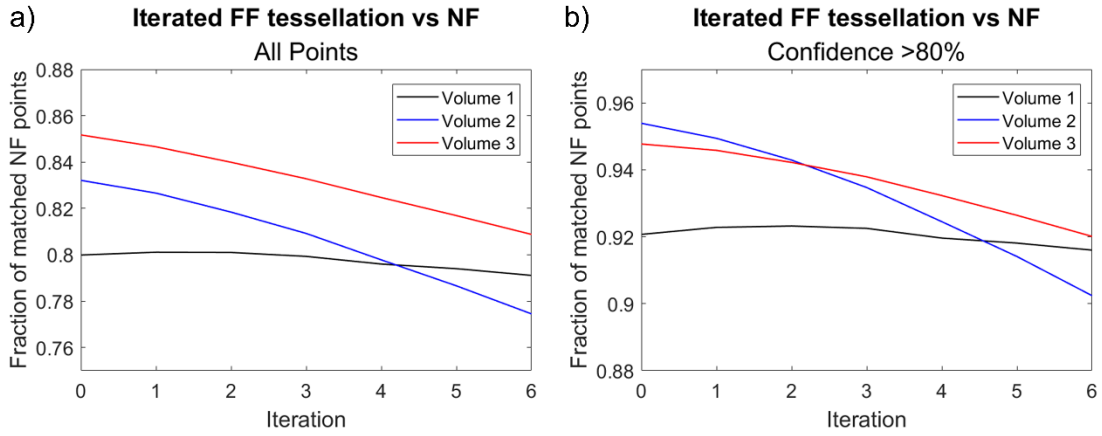

Figure 5.9: Results from iterating the tessellations made from Equation 5.5 to bring the relative tessellated grain volumes closer to the relative FF-HEDM grain volumes. Apart from a slight increase in the match fraction for Volume 1 after two iterations, this approach does not improve the tessellations' match to the NF-HEDM data.

5.2.7 Quantifying grain boundary accuracy

Given that the NF-HEDM grain boundaries are uncertain, the question arises of how well a grain can be determined to have cracked trans- or intergranularly. Using a tessellation with an additional level of uncertainty near the boundaries further complicates grain assignation. Quantifying the uncertainty would allow for some restrictions to be placed on how close the crack can come to the tessellation boundary to be considered as potentially being intergranular for a particular grain.

First, the difference between the nominal grain boundary and its true location must be estimated. As seen in Figure 5.1a, the grain boundaries resulting from assigning each NF-HEDM point to the closest-match grain, even if that match has low confidence, are irregular and imprecise. Restricting the confidence to 80% (Figure 5.2b) leaves some gaps between grains, but in some regions that gap is negligible, with a clean grain boundary appearing. The true grain boundary should also be clean and approximately planar, and should therefore lie somewhere between the nominal and confident boundaries. Exactly how wide that gap tends to be must be determined as a first step for an uncertainty estimate.

Simply summing the volume of each individual voxel assigned to a grain in NF-HEDM and calculating the equivalent spherical radii is not the most ideal estimate for either the overall size of the grain or its confident volume, since, as previously explicated, many of these grains may be cut off by the edges of the interrogated volume or the sample. Instead, the necessary information is the average difference between the surfaces of those volumes. By measuring the distance to the centroid from every point on both surfaces, the difference in those average distances can be measured. Additionally, there is then no need to eliminate datapoints from the volume surfaces, since the same distances would be calculated for both the confident and regular sets of voxels and will thus cancel out.

The same calculation can be performed on the voxels assigned to a grain from the tessellation to determine how far the tessellation's estimated boundary is from the approximate NF-HEDM one. The results from both calculations are presented in Table 5.6. Neither set of calculations trends with the overall FF-HEDM grain size.

Table 5.6: Differences between boundaries between the ground-truth NF-HEDM results and the best match tessellations.

	Δ(mean nominal NF boundary – mean confident NF boundary) (μm)	**Δ(mean nominal NF boundary – mean tessellation boundary) (μm)**
mean	20.95	4.79
median	20.00	4.26
standard deviation	9.29	13.01
extrema	55.79	-39.31, 44.34

Promisingly, the average difference between the NF-HEDM results and the tessellations is near zero, indicating that the tessellation does not trend toward over- or under-sizing grains. In general, the difference between the nominal but uncertain NF-HEDM boundary and its confident volume is a few tens of microns, which is about the same value as two standard deviations in either direction from the mean for the NF-to-tessellation difference. Therefore, allowing for an uncertainty in the tessellation boundary of about 30 μm in either direction should account for most of the error in the tessellation and also likely capture the true grain boundary.

5.2.8 Choosing a tessellation

As seen in Figures 5.4 and 5.8, attempts to use physical properties and sub-granular data, respectively, to correct the Laguerre-Voronoi tessellation, calculated by Equation 5.5 and shown in Figure 5.2, were unsuccessful in increasing the percent match of the tessellation to the NF-HEDM ground truth. The adjustment of Equation 5.5 by Equation 5.9 with the correct parameters did provide a modest increase in percent match (Table 5.3, Figure 5.5), so that adjustment was carried into the creation of tessellations for regions without NF-HEDM data. Pictorial results for the final tessellation are shown in Figure 5.10, with comparison to the ground truth.

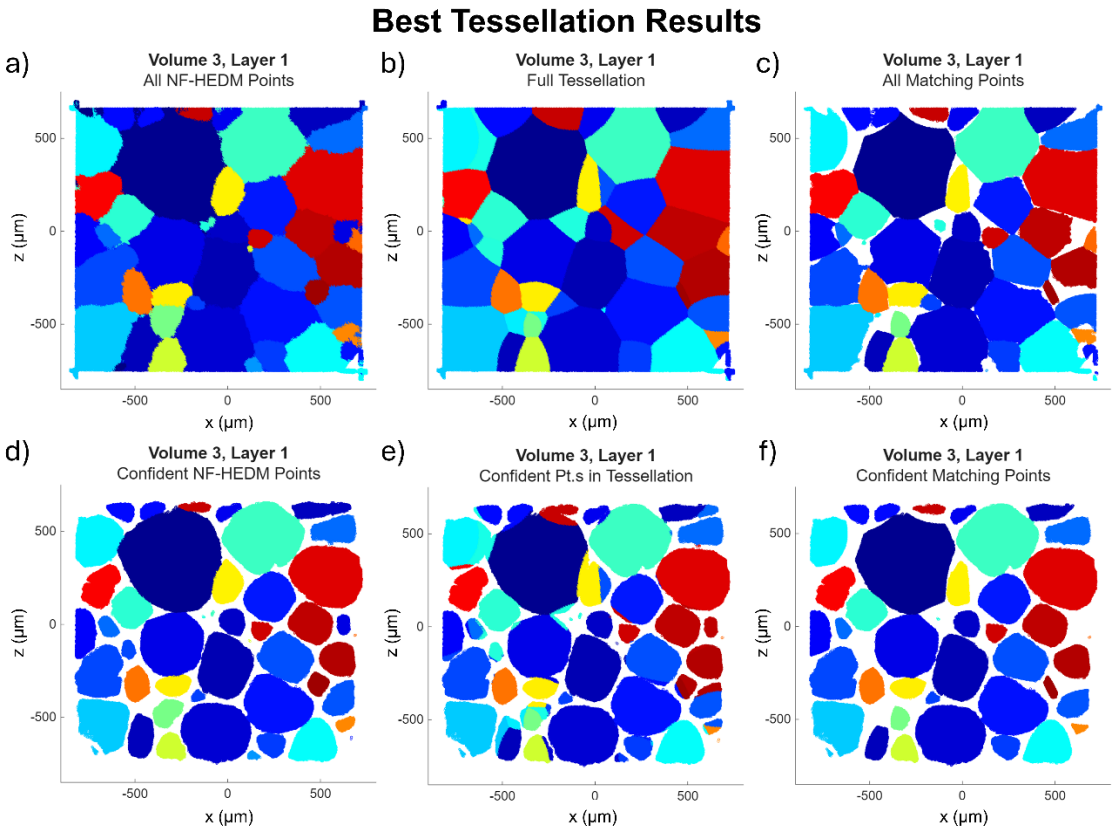

Figure 5.10: Results from the best tessellation, a combination of Equations 5.5 and 5.9, in a single 2D layer from Volume 3 in Sample 1. a) The full NF-HEDM reconstruction. b) The full tessellation. c) All points with the same grain assignation in both a) and b). d) The points in a) with confidence greater than or equal to 80%. e) The points from d) with their tessellated grain assignations. f) The points with the same grain assignation in both d) and e).

Tessellations were produced for regions in Sample 4 where FF-HEDM data was taken and the crack passed through, but for which no NF-HEDM data was available. Sample 1's FF-HEDM data without corresponding NF-HEDM were all taken in regions which did not crack and were thus not useful for determining crack behavior with regard to microstructure; additionally, the volume that was intersected by the crack was moved through completely in one extension event, meaning that no grain boundaries were obtained for grains which arrested the crack. In contrast, the crack stopped within some of the FF-HEDM volumes in Sample 4. The tessellations were generated with 200 evenly spaced points in x, y, and z, for voxels with side lengths of 6-8 μm. The tessellation's extrema were defined as ±50 μm from the extrema in the spread of FF-HEDM centroids.

An additional point of interest for the FF-HEDM scans of Sample 4 is that 12-15 100 μm-tall scans were taken for every load state, compared to 3-7 in Sample 1. As a result, the volumes all share some overlap with the preceding state, and often some of the state prior to that as well. Thus, the tessellations from subsequent scans can be checked against each other to verify the method works properly to assemble grains, even without the NF-HEDM maps being available. A sample location present in three of the FF-HEDM volumes is shown in Figure 5.11. In general, the grains exist in the same location with approximately the same size and shape among all three tests. The grain boundaries, and therefore the trijunctions between grains, can vary by a few tens of microns, in accordance with the acceptable expectations for error in Table 5.6.

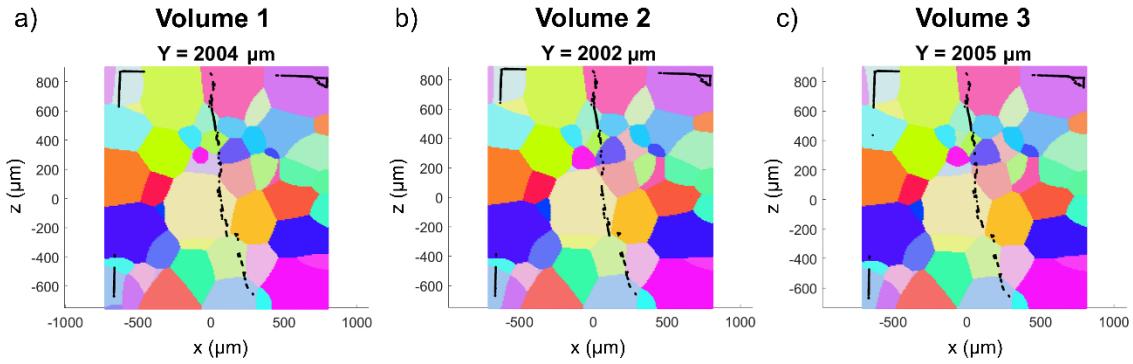

Figure 5.11: Tessellation sections from three FF-HEDM scans in Sample 4 with volume overlap. A representative 2D section is shown for each, demonstrating general similarity with some differences in grain boundaries and their distances to the crack. a) Volume 1, spanning 942 µm to 2451 µm. b) Volume 2, spanning 1536 µm to 2755 µm. c) Volume 3, spanning 1733 µm to 1961 µm.

5.2.9 Registering the tessellation to the crack

Registering the tomographic crack data to the tessellation can be performed just as it was to the NF-HEDM data in Chapter 4. From the tessellation, each grain's centroid was recalculated, since in the Laguerre-Voronoi formulation, the tessellation and seed centroids may not be identical [2]. The maximum distance from that point to the grain's surface was also calculated; grains which had a nearby crack point within 120% of that distance from the centroid were retained for examination as having been potentially intersected. As there was some overlap between the FF-HEDM volumes and therefore the tessellation volumes, grains which appeared in multiple volumes were examined for average edge-to-crack distances. Grains were then sorted into categories as defined and described in Table 5.7; the ±30 µm estimate for grain boundary accuracy (Table 5.6) was used to identify grains which were not clearly intergranular or transgranular. Additionally, grains which likely arrested the crack were identified when the last local crack points existed solely above the crack, within 55 µm (the grain boundary uncertainty plus the crack depth uncertainty from Chapter 4). Multiple assignations could be given if different branches of the crack intersected the same grain or if a grain arrested the crack at first but it later passed through intergranularly or transgranularly.

Table 5.7: Categories and definitions for tessellated grains near to the crack.

Category	Definition
Most likely transgranular	Crack cuts across grain; maximum distance to edge > 30 μm
Most likely intergranular	Crack parallel to and within 1 voxel of grain boundary
Uncertain	Crack passes within or outside grain by maximum 30 μm
Most likely arrested	All nearby crack points are above grain, within 55 μm

5.3 Results

5.3.1 Grain orientations

More than 1600 μm of the crack in Sample 4 was present in one or multiple tessellated volumes, resulting in many more grains identified as intergranular or transgranular than in the NF-HEDM results from Sample 1, although the percentages of each group compared to the total number of grains was similar (Table 5.8). With the additional information gained on grains that arrested the crack, orientation maps for the grains and the crack planes within them can be created to supplement Figure 4.10a,b (Figures 5.12-13). As before, in Figure 4.10c-f, the intergranularly- and transgranularly-cracked grains, and those which might belong to either group, do not display any prominent orientation preferences or persistent misorientations when compared to the other groups (Figures 5.12a-c, 5.13a-c). Furthermore, the grains which appear to have arrested the crack also have orientations and normals spread over the entirety of orientation space, both for those with a final arrested state and those which eventually propagated (Figures 5.12d-g, 5.13d-g).

Table 5.8: Numbers of total grains and those which cracked transgranularly or intergranularly in the studied volumes (one 250 μm-tall NF-HEDM volume for Sample 1 and a total of 2 mm of crack-containing tessellations for Sample 4).

	Number of grains in Sample 1 NF-HEDM	Percentage of grains in Sample 1 NF-HEDM	Number of grains in Sample 4 tessellation	Percentage of grains in Sample 4 tessellation
Transgranular	10	11.4%	43	12.4%
Intergranular	6	6.8%	11	3.2%
Uncertain	—	—	19	5.5%
Total	88		347	

Another piece of information not formerly available due to the small data size is orientation changes close to grain boundaries; the same 30 μm distance used to determine possible intergranular status was used to define “close”. Figure 5.13h shows the orientation planes that did crack for each grain and the changes between adjacent grains in blue, versus the potential grain-frame orientations that the crack apparently avoided by changing direction, in red. As there are no preferential orientations onto which the crack plane might be diverted, however, there is no apparent consistency between the orientation changes. Some changes lead the crack to reside on a very different plane while “avoiding” a plane with much smaller misorientation, while two grains with a similar crack plane might see that plane diverted to completely different orientations upon exiting. Thus, as noted in Chapter 4.4.1, crack direction and orientation must be more dependent on localized and volumetric effects than on individual grains’ properties, leading to gradual changes to the crack both before and after its interaction with a specific local volume.

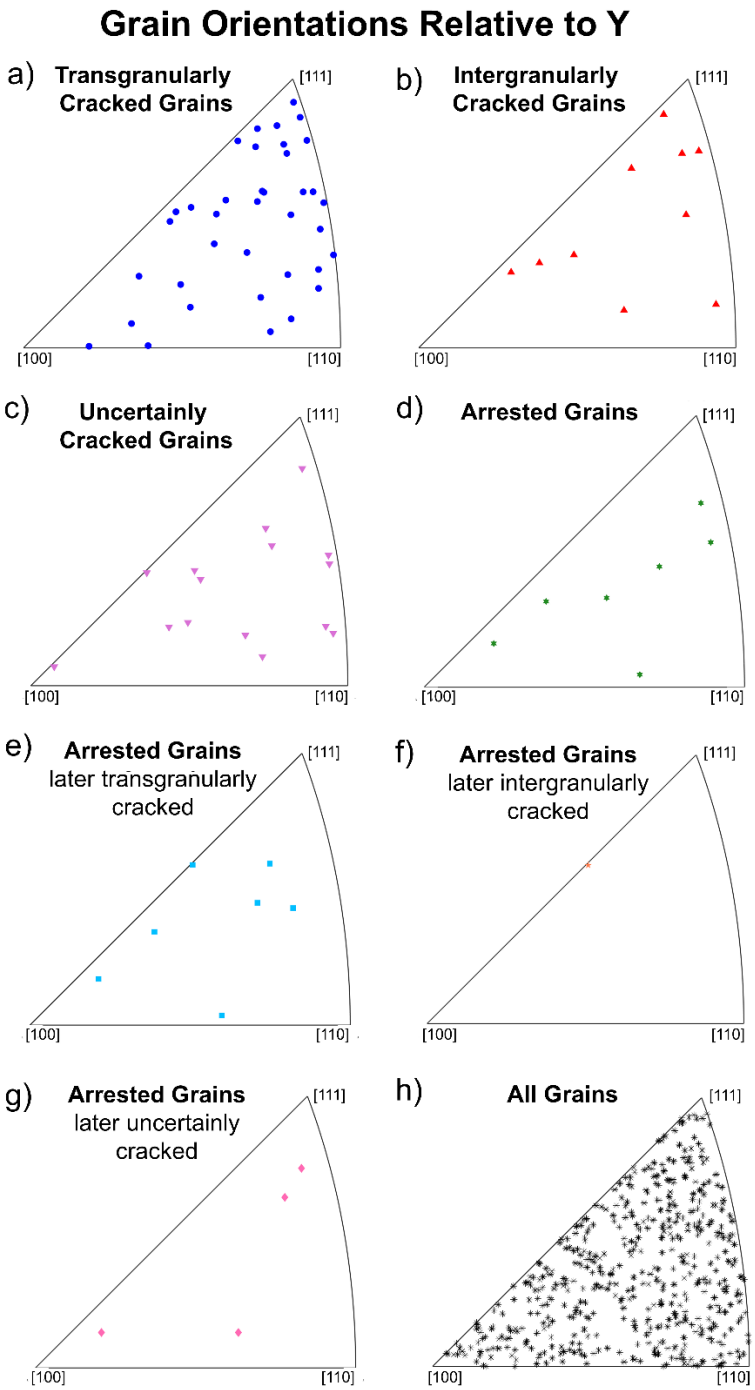

Figure 5.12: Inverse pole figures showing the orientations of FF-HEDM grains in Sample 4, relative to the loading (*y*) direction, identified as belonging to one or multiple groups described in Table 5.7. As in Figure 4.10, the groups do not display major distribution differences.

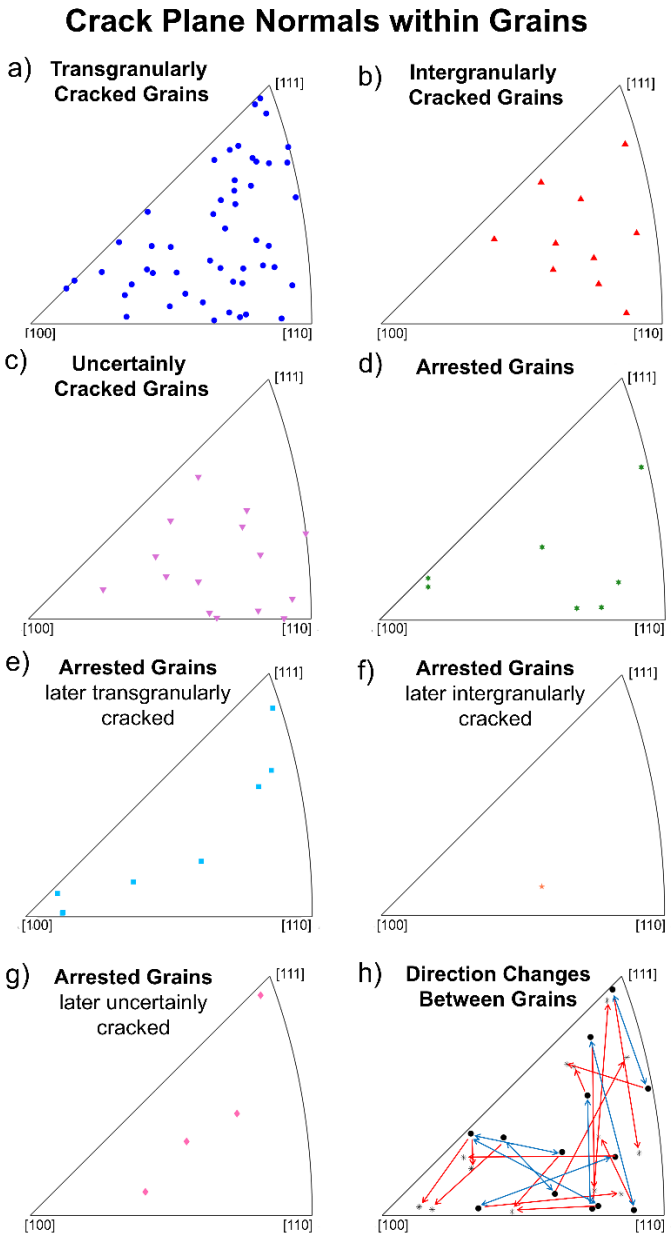

Figure 5.13: a-g) Distributions of the directions normal to the average crack plane in Sample 4 within each grain's unit lattice, with grains sorted into the groups described in Table 5.7, and generally distributed without trend. h) For cracks which changed direction near a grain boundary, the plane normal in both grains (dots), the crack orientation change between them (blue), the potential crack plane normal in the neighboring grain if the direction change did not occur (stars), and the crack orientation different to that normal (red), again without obvious trends.

While the overall orientation of the grains which appear to have arrested the crack in any capacity also do not follow a trend, by extracting the grain boundaries ahead of the crack, their normal vectors can be calculated and may reveal additional information. Figure 5.14 shows these vectors for the grains identified as arresting the crack and further delineates them into those which later cracked transgranularly, intergranularly, or uncertainly, and those which continued to arrest the crack until the end of the experiment. As noted in Chapter 4.4.3, sharp deflections of the crack, especially during a fast propagation event, are generally rare; thus, only a single grain later cracked intergranularly, and only because the original arrest occurred very close to that boundary. As expected, the grain which later cracked intergranularly has the smallest y component and the largest-magnitude x component due to the presence of the grain boundary on which it passed; the uncertain grains also have larger-magnitude x components as the grain boundaries slope down near their edges where the crack moved through (Figure 5.14c). The grains which first arrested the crack and later passed transgranularly also generally have smaller y components than the grains which were still arresting the crack at the end of the experiment, but larger y components than the other two populations. Thus, the crack reached the final arresting grains at planes nearly perpendicular to its direction of motion, which provided an effective barrier to further extension. For the grains which were later cracked transgranularly, the crack either had to divert slightly, if possible, to a more favorable plane, or it reached the grain at those planes initially, making them easier to crack.

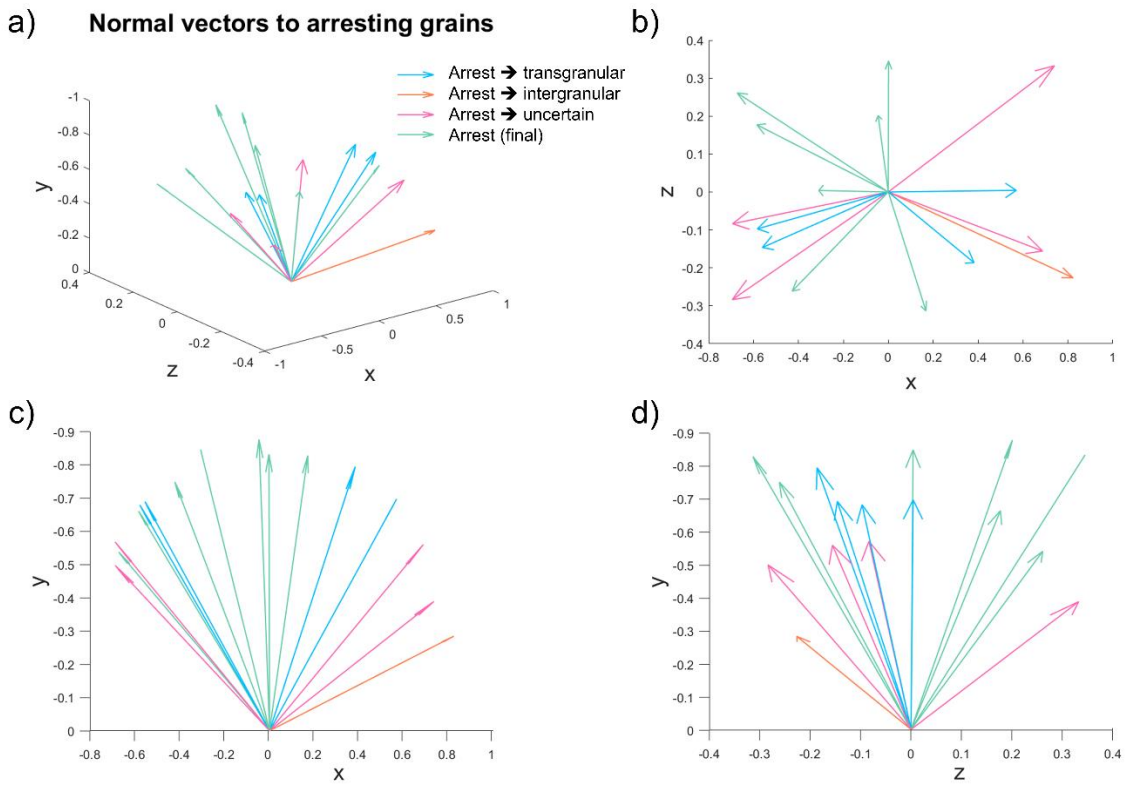

Figure 5.14: Grain boundary normal vectors ahead of the crack in Sample 4. a) 3D space b) x and z components c) x and y components d) y and z components. The grains which permanently arrested the crack have greater y components, indicating the crack reached them head-on.

5.3.2 Grain mechanical states

Similarly to the orientation results, while the analysis of grain stress states in the NF-HEDM data of Sample 1 did not show any particular trends (Figure 4.10a-b), those results can be expanded upon with the addition of more grains, overlapping volumes, and information on grains and regions which arrested the crack from the Sample 4 tessellations. Figure 5.15 shows the results from three FF-HEDM volumes with different grains highlighted. Figure 5.15a), c), and e) depict the volumes with overlaid information for grains which have already interacted with the crack; that is, those that have already cracked intergranularly or transgranularly, or been arrested, while Figure 5.15b), d), and f) show those same volumes with overlaid information for grains which cracked or which arrested the crack in the following extension. Volume 1 overlapped with the crack front after the first extension,

and thus includes grains of all types (Figure 5.15a); the next two extensions both added less than 100 μm to the overall crack length, and so few additional grains were identified as interacting with the crack, although some did arrest it (Figure 5.15b). Volume 3, meanwhile, contained only a few grains which had already cracked prior to the data collection (Figure 5.15c), but the ~800 μm extension that occurred next resulted in acquiring information on the stress states of many grains before they were cracked or arrested the crack (Figure 5.15d). Finally, Volume 4 was taken after that extension and did include the crack front with data on arrested grains and a few others (Figure 5.15e); however, examining that volume for grains which had not yet interacted with the crack did not uncover any which cracked in the next extension (Figure 5.15f). The next extension was the final one, and as described in Chapter 4.3.2, this extension did not propagate from the original crack front, but represented a second crack front that branched off of the initial one before propagating through the entire sample volume (Figure 4.3e-f). Thus, the previous Volumes 1 and 3 were examined for information on grains which cracked or arrested the crack with the new extension (Figure 5.15g-h).

As reported in Chapter 4.3.3, the stress values for all populations display no obvious trends. Representative statistics are reported in Table 5.9, with stresses normalized to the overall sample load for comparison. In both the x and y directions, the stresses in grains already cracked or arrested before the FF-HEDM data collection fall within similar ranges for all populations. For data taken before the crack reached the grains of interest, both σ_{xx} and σ_{yy} for the grains about to arrest the crack are higher than for grains of other populations, but are still within one standard deviation of the other population means as well as the mean stress for all grains in the volume.

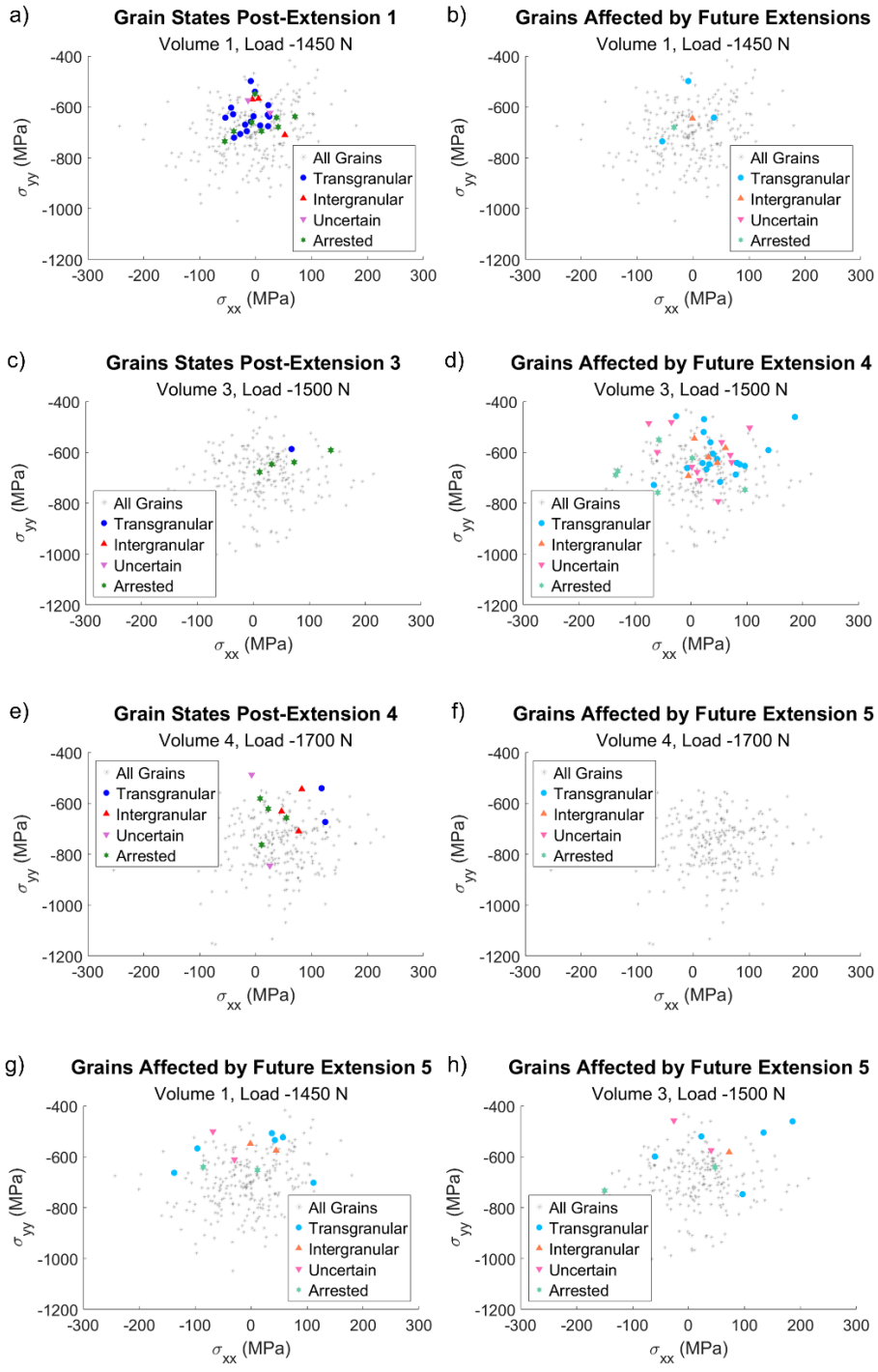

Figure 5.15: Stress states for FF-HEDM grains in Sample 4, highlighting those interacting with the crack. a,c,e) Highlighting grains which interacted with the crack before the FF-HEDM data was acquired. b,d,f-h) Highlighting grains which have not yet interacted with the crack.

Table 5.9: Stress statistics, calculated after normalizing to the overall load, for FF-HEDM grains in Sample 4, grouped into type of crack interaction and whether the FF-HEDM data is from before or after the interaction.

	Already interacted σ_{yy}/σ_a	**Not yet interacted** σ_{yy}/σ_a	**Already interacted** σ_{xx}/σ_a	**Not yet interacted** σ_{xx}/σ_a
Transgranular	0.95 ± 0.14	0.92 ± 0.13	-0.020 ± 0.10	-0.062 ± 0.084
Intergranular	0.90 ± 0.11	0.93 ± 0.09	-0.059 ± 0.048	-0.035 ± 0.041
Uncertain	0.87 ± 0.16	0.91 ± 0.15	0.011 ± 0.055	-0.029 ± 0.086
Arrest	0.99 ± 0.10	1.02 ± 0.11	-0.018 ± 0.091	0.066 ± 0.11
All grains	1.04 ± 0.16		-0.026 ± 0.095	

Due to the overlapping nature of the examined volumes, the changes in mechanical state for individual grains can also be explored. While the overlap was often small, only a few FF-HEDM scans or a few hundreds of microns, some grains of all the examined types had data from at least two scans (Figure 5.16). With so few data points, definitive claims will not be attempted, but in general, arresting grains, especially those which remained arrested for both scans in a comparison, tend to take on more tensile stress upon increase in load, with the magnitude of σ_{xx} increasing and that of σ_{yy} decreasing. This most likely is because without the barrier of the arresting grains, the crack would ideally open in that location, but due to the hindrance of its location and grain boundary orientation, a greater force is needed to do so when compared to more easily cracked grains. Meanwhile, grains which were cracked intergranularly or transgranularly in between the two scans have $\Delta\sigma_{xx}$ closer to, if not less than, zero, indicating a relief in stress as the crack is no longer being forced to open there.

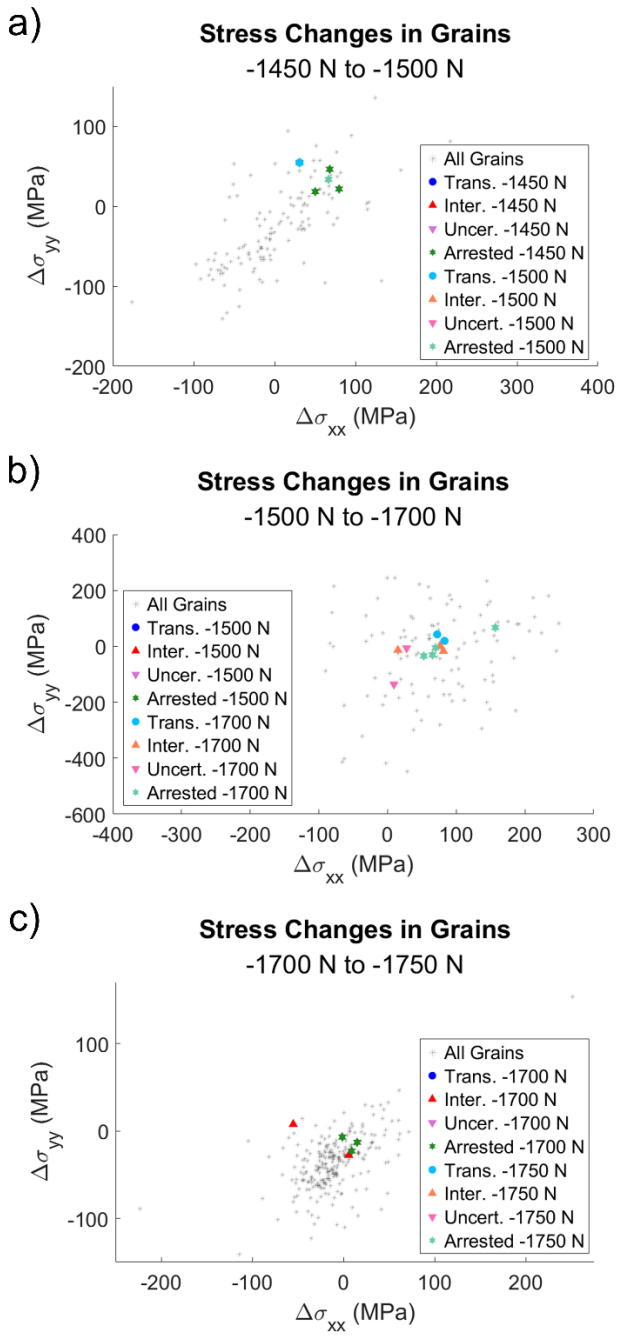

Figure 5.16: Changes in grain stress state between subsequent loading steps in Sample 4, with grains interacting with the crack highlighted similarly to Figure 5.17. Grains which had already cracked or arrested the crack by the time of the first scan are differentiated from those which were cracked or arrested the crack during the next extension, just before the second scan.

5.4 Discussion

5.4.1 Volumetric effects on crack extension

Chapter 4 and the previous section demonstrate that while individual grain properties do affect the crack in measurable ways, the interaction of the grains with each other produces other emergent effects which are more difficult to relate to specific crack movements. For example, while the fracture toughness of individual AlON grains can be calculated [11], studying an entire suite of grains can only result in obtaining the average local fracture toughness. However, this is not to indicate that such properties are beyond understanding or disassembling.

The local stress environment is explored in Chapter 4.3.1 and Figure 4.7, and this analysis can be extended by considering the strain energy density of the material. Strain energy is a measure of how much internal energy is contained within a volume as a result of stress buildup, and the variance of that energy independent of volume is the strain energy density *W*, the grain-averaged value of which can be calculated using Equation 5.11 and the FF-HEDM strain and stress tensors [12]. The strain energy density is also related to the stress intensity factor and strain energy release rate in that it can be related to the total amount of internal resistance to crack propagation (Equation 5.12) [13].

$$W = \frac{1}{2}\sum \sigma : \varepsilon \qquad \text{Equation 5.11}$$

$$G = \frac{\partial U_S}{\partial C} = \frac{\partial}{\partial C}\left[U_{other} + \int W dV\right] \qquad \text{Equation 5.12}$$

Thus, with an increase in strain energy ahead of the crack, it follows that *G* also increases, as more potential energy can be released upon crack extension, making it more favorable to propagate the crack. Similarly to the calculations in Figure 4.7, the strain energy density can be tracked in grains around the crack (Figure 5.17). For comparison, the value for *W* for an isotropic, uniaxially stressed AlON sample with the averaged reported Young's modulus and Poisson's ratio [14] is calculated and displayed (Equations 5.13-15) [12].

$$\sigma = \begin{bmatrix} 0 & 0 & 0 \\ 0 & \sigma_A & 0 \\ 0 & 0 & 0 \end{bmatrix} \qquad \text{Equation 5.13}$$

$$\varepsilon = \begin{bmatrix} -{}^{\nu\sigma_A}/_{E} & 0 & 0 \\ 0 & {}^{\sigma_A}/_{E} & 0 \\ 0 & 0 & -{}^{\nu\sigma_A}/_{E} \end{bmatrix} \qquad \text{Equation 5.14}$$

$$W = \frac{1}{2}\sum \sigma : \varepsilon = \frac{\sigma_A^2}{2E} = \frac{F^2}{2EA^2} \qquad \text{Equation 5.15}$$

F = force on sample A = area of sample face contacting the compression platens

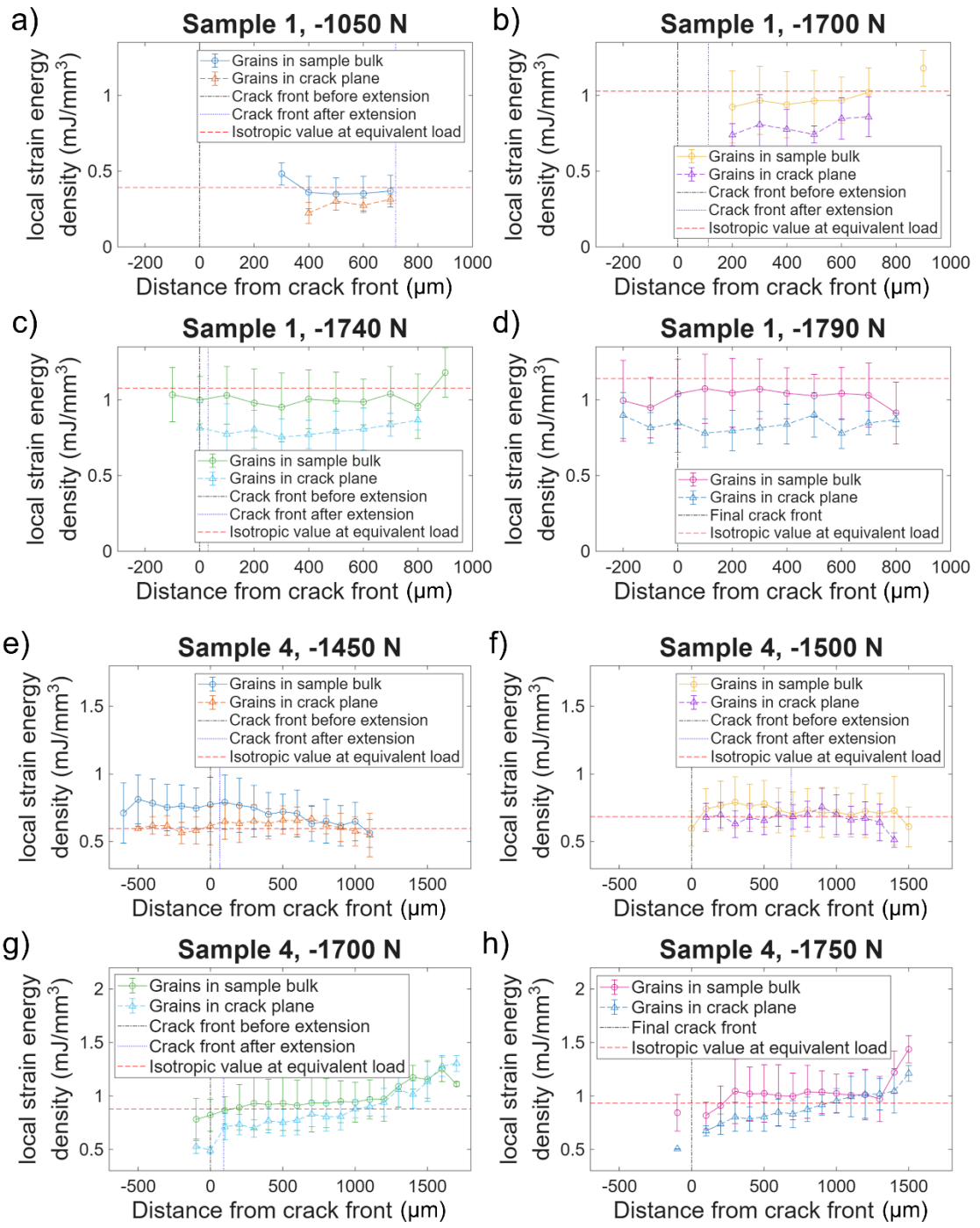

Figure 5.17: Strain energy density as a function of distance from the crack in Samples 1 and 4, compared to the expected value for an isotropic sample at equivalent load. a-d) Sample 1. e-h) Sample 4.

The gradient in σ_{yy} with distance from the crack tip noted in Chapter 4.4.1 directly affects the strain energy density, with a similar, positive gradient present in Sample 4 ahead of the crack at -1700 N and -1750 N (Figure 5.17g-h), where the initial crack and the secondary branching crack stopped growing, respectively. While these volumes did not crack over the duration of the experiment, they were accumulating strain energy as the stress continued to build without any extension to relieve it locally. In fact, for most of the volumes studied, the data for which was collected immediately after extension, the strain energy density remained mostly flat or decreased ahead of the crack front, indicating little additional impetus for the crack to extend.

Interestingly, the positive gradient in W for Sample 4 at the crack's final extensions is more prominently present far from the crack front, with the local volume just ahead of the crack still somewhat depressed, especially for the volume at lower load, and therefore lower stress.

The region just ahead of the crack front still shows an increasing trend, but the internal stress was not relieved by crack extension even after bringing the sample up in load to -1900 N. Investigation into that volume might reveal why no crack extension occurred despite the stress conditions being apparently favorable.

With the tessellations, the grain volumes can be considered at smaller sub-volumes than the 100-μm tall FF-HEDM volumes, and thus more localized effects can be considered. Specifically, when considering the average orientation of the grains with which the crack interacts, such information can be extracted for small sub-volumes such as those the crack extended through during its localized bursts of movement. Figure 5.18 shows the volume-averaged orientations, using the tessellated volumes as a basis, of the regions ahead of the crack, overlaid with the average length of the crack extensions seen in Figure 4.8. From the top of the tessellation to about 1500 μm, around which length the crack grew in short events and eventually stopped growing over a 200 N increase in load, the average plane orientation perpendicular to the crack was closest to the <110> directions. For the next few hundred microns of depth, that average normal moved closer to <111> directions before further changing to close to the <100> orientations. When the crack did eventually extend, in the nearly 800 μm fourth extension event, and in the subsequent branch pop-in and extension, it

moved fully past the near-<100> region before again stopping in a region closest to the <111> normals, with another near-<100> region existing ahead.

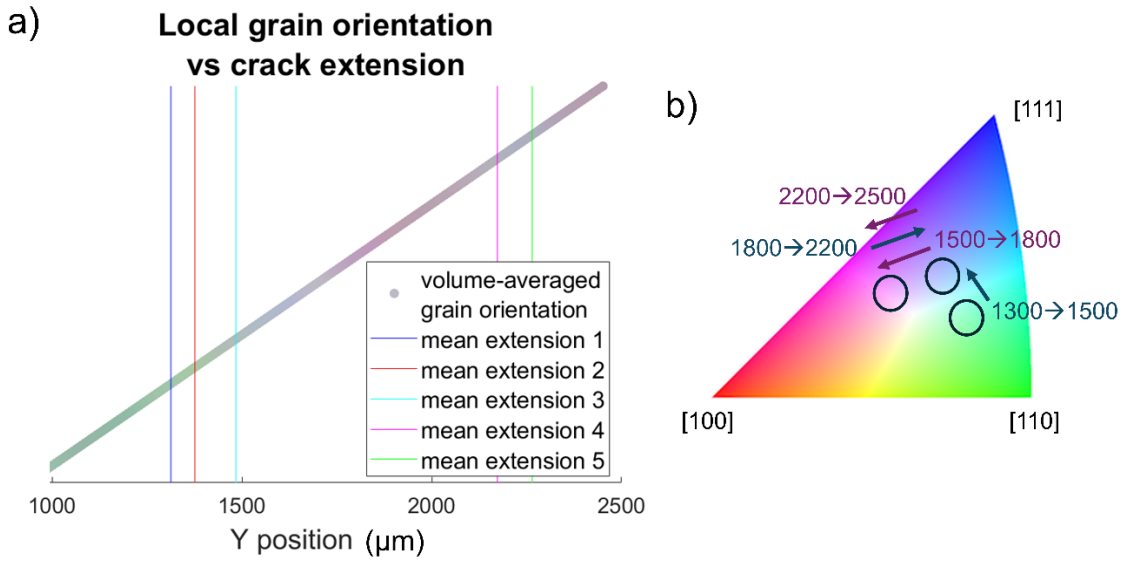

Figure 5.18: a) Crack extension in Sample 4 plotted against volume-averaged grain orientation, colored by standard IPF colors, for 2D slices in *y*. b) Standard IPF colors by orientation, with the average orientations for regions in a) marked and labeled, showing the transition between regions as a function of sample depth.

While, again, the crack does not show any major preferences for its eventual orientation within a grain, nor are individual grains of specific orientation more prone to arresting its motion, this result does suggest that when considering larger volumes and groups of grains, the total effect of grain orientation and the future crack plane orientation can serve to prevent crack extension and affect fracture toughness. Notably, in FCC materials, including AlON, the {111} planes are considered more prone to slippage and cracking [11], so the fact that the volumes ahead of the crack's stopped locations have a larger portion of <111>-oriented grains, perpendicular to the {111} planes, might play a role in why more energy must be accumulated to crack those regions. Once enough load has been achieved, the crack then moves fully past those regions before stopping at a similar localized group of orientations. This effect can be related to that hypothesized in Chapter 4.4.1, where regions of higher fracture toughness arrest the crack, and subsequent long extensions indicate it moving through a region with lower fracture toughness than that just experienced. Thus, a further

hypothesis can be created, that groups of grains of related orientations can create these regions of varying toughness.

5.4.2 Grain boundary and trijunction effects on crack orientation

Beyond the orientations of grains, the orientation of grain boundaries can also be explored using tessellations and the access they provide into sub-volumes of FF-HEDM data. As in the previous section, groups of grains and local changes can be examined to glean more information beyond the average orientations of grains which interacted with the crack in different ways.

One hypothesis that can be explored from the previous chapter is whether a grain boundary's proximity to the crack is a major factor in whether the crack will move intergranularly. Additional questions can be posited about the angle of the grain boundary compared to that of the crack, the misorientation of the two grains on either side of the grain boundary, and the amount by which the crack moves to intersect such a boundary at distances far from it. Some of these questions will be considered, with Figure 5.19 assisting the explanations.

In Figure 5.19a, the effect of grain boundary orientation in the sample is related to that of the crack. In general, the more angled the boundary is to the centerline of the sample, the greater the deviation the crack must make (when compared to its average linear profile) to intercept it; at the same time, grain misorientation shows little effect on that deflection (Figure 5.19b). Therefore, nearby grain boundaries of the correct orientation are more likely to be intergranular than those angled more dramatically to the crack, lending additional credence to the observation in Chapter 4.4.3, that intergranular fracture generally occurs as a result of grain boundary proximity and similarity to the existing crack.

When considering the initial deflection to the final orientation when leaving the grain boundary (compared to the crack's average linear profile over 300 μm at depths 50 μm above and below the boundary), the crack is found to generally have a smaller deflection upon exiting than it did upon entering (Figure 5.19c). Two possibilities therefore arise: that the crack has a persistent orientation shift as a result of the boundary, or that the boundary was closer to the crack's orientation deeper in the sample, and affected it enough to divert it even

when a larger deflection would be required. These effects are difficult to uncouple, especially when other nearby grains are also affecting the crack's local orientation. However, the second possibility may serve to explain the instances with particularly large deviations which are diminished upon the crack's exit from the boundary.

A final question arises due to Sample 4's more angled profile to the centerline of the sample when compared to Sample 1, even before the branching (Figure 4.3): whether the grain boundary deflections serve to orient the crack closer to straight through the sample center. However, when comparing the crack's deviation not from its linear profile but from the centerline of the sample before and after grain boundary interception, the crack is not found to substantially be diverted toward a more centered profile and instead retains a similar overall angle to the centerline (Figure 5.19d). Thus, grain boundaries may affect the crack locally but, as Figure 5.19a shows, the closeness to the angle the crack makes with the boundary is more of an effect than any possible future angular change the crack might make toward growing straight in the center.

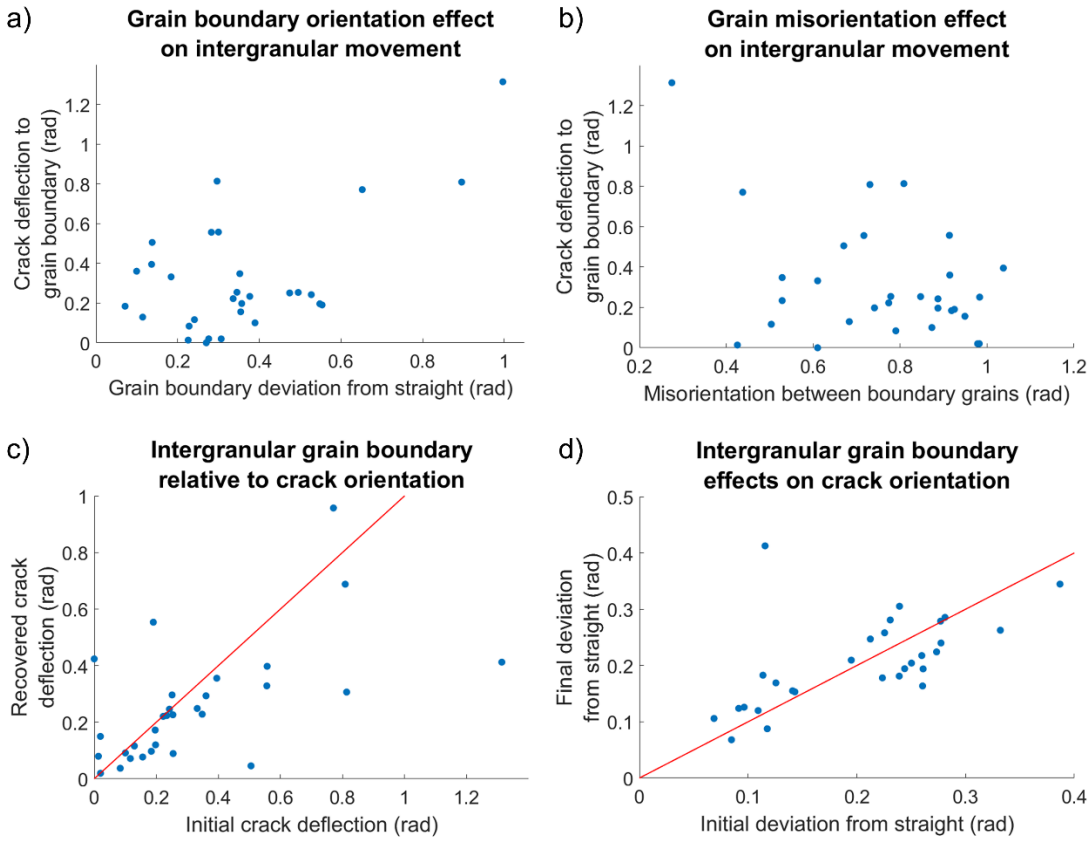

Figure 5.19: Intergranular grain boundary properties. a) The greater the angle the grain boundary makes to the centerline of the sample, the more the crack has to deflect to intercept it. b) The misorientation of the grains on either side of an intergranular grain boundary do not determine the crack's deflection. c) In general, the crack's initial deflection to intercept a grain boundary is greater than the angle it makes to the grain boundary after leaving. d) The angle the crack makes to the centerline of the sample does not change dramatically before and after following an intergranular grain boundary.

Some of these grain boundary effects are presented in more detail within the tessellated volumes in Figures 5.20 and 5.21. Figure 5.20 shows several 2D slices in the region cracked by the first crack extension, located roughly 50 μm apart in depth, and points out interactions with a few grains. In Figure 5.20a, the crack has intersected (to within one voxel) two trijunctions, pointed out in white arrows. Additionally, a short intergranular section is observed emanating out of the trijunction labeled in the lower half of the image (maroon

arrow). 50 μm deeper, in Figure 5.20b, the crack is still near both trijunctions in the upper portion. While it has moved away from the previously intergranularly-cracked boundary in the lower half, a small kink still remains in the crack's profile, roughly parallel to that boundary (gray arrow). In the upper half of the image, after leaving the trijunction, the crack has not substantially changed its angle, but now follows a grain boundary for nearly its entire length between two grains. Another 50 μm deeper, in Figure 5.20c, that intergranular section has disappeared, but again without much angular change, the crack now intersects a trijunction on the other side of the region the intergranular crack traversed. Essentially, the crack mostly followed a straight path between two trijunctions not connected by the same two grains, and in the process intersected with a grain boundary. In Figure 5.20d, the lower portion of the crack once more has a short intergranular section coincident on the same grain boundary as before, again tied to a trijunction, although a different one. Just as the kink from the first grain boundary intersection remained present for more than 100 μm, comparing this new intergranular section to the previous images shows that another kink had already developed 150 μm higher in the sample and slowly grew closer to the grain boundary until it became an intergranular section.

Fully determining how persistent these kinks are above and below the intergranular or intersection points, and therefore the force of attraction between the crack and the boundaries, is complicated due to the presence of other grains and grain boundaries. However, what is demonstrated is that even if a grain ultimately cracks transgranularly, its grain boundaries may serve as attractive regions for the crack to move through for short intervals during propagation. The grains identified as fully being intergranular (Figures 4.9-10, 5.12-13) may simply be those with a short boundary parallel to the crack which diverges above and below the point of contact; thus, their difference in orientation distribution from the transgranular grains, which may contain intergranular sections but which have boundary extrema farther from the crack, is unsurprising. Additionally, the presence of trijunctions on either side of a grain boundary may serve to direct the crack along such local grain boundaries.

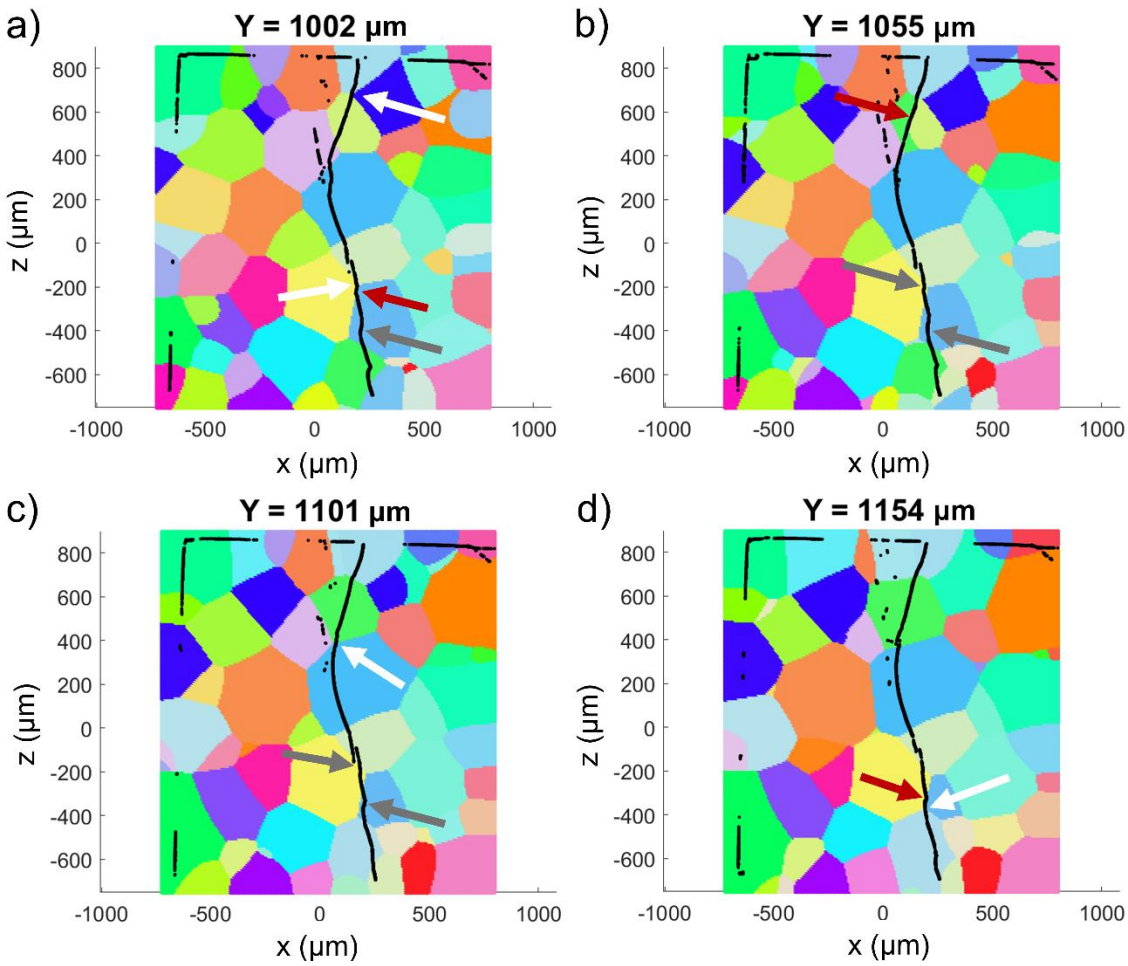

Figure 5.20: 2D slices of the tessellation for Volume 1 of Sample 4, overlaid with the final crack profile (black). White arrows mark the crack's intersection with a trijunction, maroon arrows indicate where the crack follows a grain boundary, and gray arrows point out kinks in the crack profile before and after one of the previous intersection types. a) The crack intersects with one trijunction near the top and one near the bottom, with the latter intersection extending into a local grain boundary for intergranular cracking. b) The crack leaves the upper trijunction and follows a parallel grain boundary; the crack also leaves the lower trijunction and boundary but retains a kink parallel to the grain boundary. c) The upper portion of the crack intersects with another trijunction. d) The lower portion of the crack has another section run parallel to the same grain boundary as in a), but pinned at the opposite trijunction.

In another region, this one within the near-[111] region pointed out in Figure 5.18, some of the extent of granular interaction effects on the crack can be seen. More intergranular sections and trijunction intersections are present in this section than the previous, potentially because of the region's resistance to cracking. Some of the grain boundaries might have served as easier-to-crack sections for the crack experiencing a paucity of low-energy locations through which to move. Specifically, the crack stays pinned at some of these regions, even when the crack must deflect to do so as boundaries and trijunctions move out of the crack's path. For instance, in the purple grain in the lower portion of Figure 20b-d, located about 75 μm apart in depth, the crack cuts transgranularly through it while intersecting with two opposing trijunctions. Even before the grain appears in the slice (Figure 20a), the crack has developed a curve in the region where the grain is about to appear as if to intercept the trijunction upon its genesis. Then, when the trijunction is about to move away from the crack, it again develops a curve following the trijunction's direction of movement, potentially indicating some favorability for staying pinned rather than continuing along a straight path. Additionally, upon its exit from both trijunctions in the grain, the crack cleaves through or parallel to grain boundaries on either side, following them intergranularly for a time before diverging. In the upper portion of the images, another series of intersected trijunctions and intergranular cracks is visible, with several smaller grains overtaking each other one-by-one and allowing the intersections to persist, all without the crack's orientation changing substantially.

Fully understanding the energy landscape in these regions remains complicated, although phase-field models show promise for uniting many aspects of the complex continuum mechanics present among these collections of grains [15–17]. The crack does clearly respond to changes resulting from the way grains of different sizes and orientations are arranged, so accurately capturing the variation in stress between and within grains via models will be a major step forward in understanding how and where cracks propagate in polycrystals.

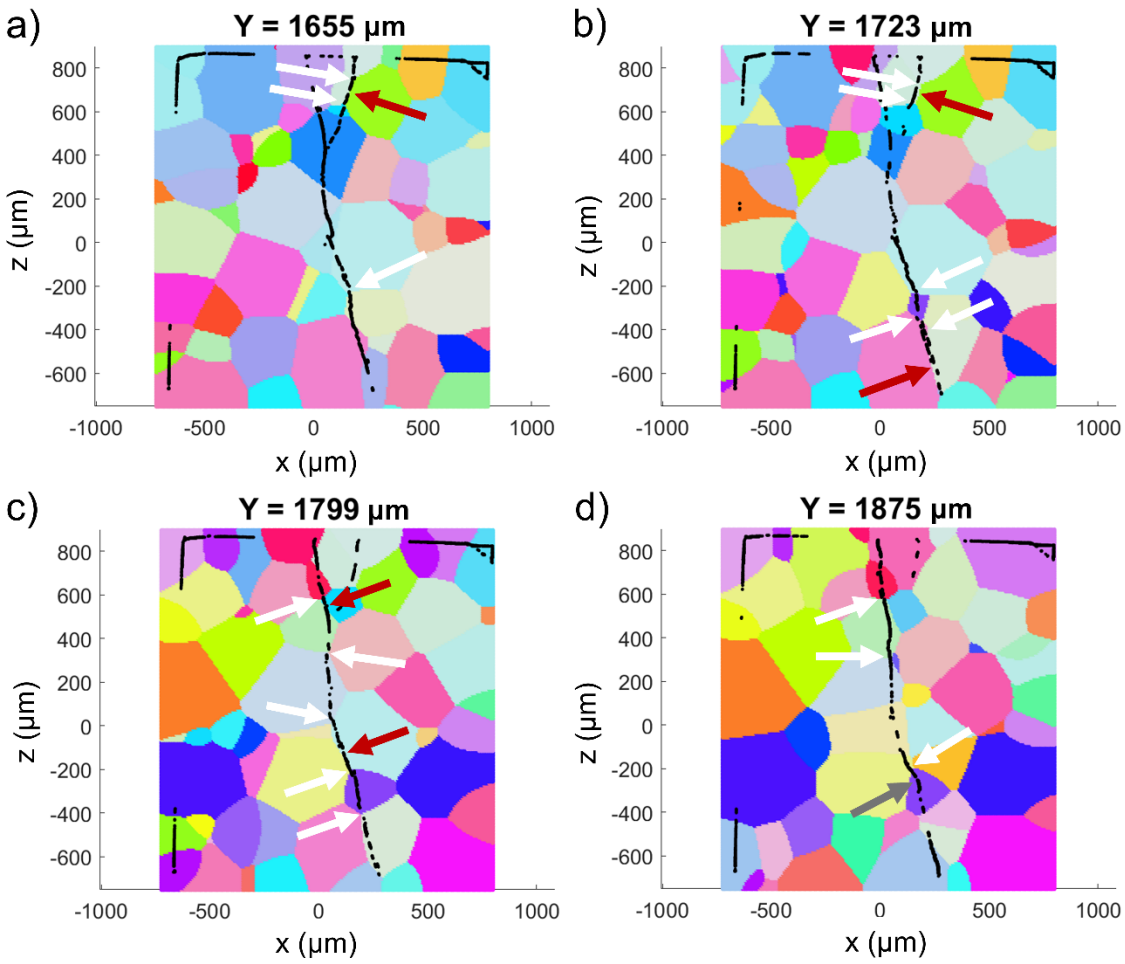

Figure 5.21: 2D slices of the tessellation for Volume 1 of Sample 4, overlaid with the final crack profile (black). White arrows mark the crack's intersection with a trijunction, maroon arrows indicate where the crack follows a grain boundary, and gray arrows point out kinks in the crack profile before and after one of the previous intersection types. a) The upper portion of the crack follows a grain boundary and intersects with both of the bordering trijunctions. b) The crack remains at the upper grain boundary; the lower portion of the crack bisects a grain through two trijunctions. c) A branch of the upper portion of the crack coincides with a trijunction and grain boundary; the lower portion remains pinned at the same trijunctions and also extends near grain boundaries on either side. d) The upper branch remains at the same trijunction; the lower portion does as well but has to develop a kink to stay pinned.

5.5 Conclusion

FF-HEDM data from AlON has been shown to produce maps of grains and microstructure with good agreement to more precise but more costly NF-HEDM data. As a result, conclusions about characteristics of grains which interacted with the crack in different ways can be expanded, and additional information about grains which arrested the crack gained. Exploring the latter reveals trends in the orientation of grain boundaries opposing the crack's motion, with those arresting the crack for longest being close to perpendicular to the crack's direction of propagation. Furthermore, arresting grains demonstrate a slight response toward accumulating stress in the crack opening direction with further application of load, as the energy required to overcome the resistance to cracking increases there.

Additionally, information on the average orientation of grains ahead of the crack is presented. With smaller volumetric subdivisions available from the tessellation than from the full FF-HEDM scans, gradual changes in the orientations of the collected grains are revealed, with many more grains with {111} planes perpendicular to the crack present ahead of regions where it stopped moving, as compared to regions which did not arrest the crack. Investigation into these regions shows that the crack interacted with more grain boundaries and trijunctions in the apparently unfavorable regions than in regions with more {110} planes perpendicular to the crack's direction of propagation.

Taken together with the results from full NF-HEDM, the promise of synchrotron experiments for capturing in-situ cracks in brittle materials with heterogeneous and anisotropic microstructure is extended further. The combination of HEDM and CT allows for both small-scale and larger-scale microstructural analyses around a growing crack, all of which is useful for obtaining data on specific grains as well as how the properties of those grains affect each other to allow or hinder crack propagation. While individual grains do not display obvious trends which would mark them as being predestined to crack in a certain way, the larger surrounding volume and nearby grains play a crucial role in determine the crack's motion through, around, or abutting against specific grains. As the stresses and strains within the material vary within and between grains, affected by their size, orientation, and boundary location, so too do the forces on the crack change, resulting in angular deviations and arrests that cannot be associated with any one grain or even a few local grains.

The use of phase-field models should hopefully prove promising in addressing such field inhomogeneities and their emergent effects on the crack's path and loading response, especially for modeling the relationship between how grains distribute stress among themselves and where the crack eventually moves. However, volumetric considerations must be considered, as increasing the size of a studied volume to capture all intergranular effects increases computation costs. Performing experiments on other materials may help reveal what effect grain size, sample size, and material choice have on the internal length and other properties used to determine how material properties change throughout the field, so that the necessary information most impacting the crack's progression can be prioritized.

Bibliography

[1] V. Tari, R.A. Lebensohn, R. Pokharel, T.J. Turner, P.A. Shade, J.V. Bernier, A.D. Rollett, Validation of micro-mechanical FFT-based simulations using high energy diffraction microscopy on Ti-7Al, *Acta Mater* 154 (2018) 273–283. https://doi.org/10.1016/j.actamat.2018.05.036.
[2] S. Falco, J. Jiang, F. De Cola, N. Petrinic, Generation of 3D polycrystalline microstructures with a conditioned Laguerre-Voronoi tessellation technique, *Comp Mater Sci* 136 (2017) 20–28. https://doi.org/10.1016/j.commatsci.2017.04.018.
[3] J. Kim, Y. Hayashi, S.S. Ha, M. Yabashi, Tessellation-based grain boundary determination for X-ray orientation microscopies, *Comput Phys Commun* 320 (2026) 109988. https://doi.org/10.1016/j.cpc.2025.109988.
[4] W.A. Tayon, D.C. Pagan, S.R. Yeratapally, T.Q. Phan, J.D. Hochhalter, Exploring the role of Type-II residual stresses in a laser powder bed fusion nickel-based superalloy using measurement and modeling, *Int J Fatigue* 181 (2024) 108153. https://doi.org/10.1016/j.ijfatigue.2024.108153.
[5] Q. Du, V. Faber, M. Gunzburger, Centroidal Voronoi tessellations: applications and algorithms, *SIAM Rev* 41 (1999) 637–676. https://doi.org/10.1137/S0036144599352836.
[6] B. Chen, D. Li, P. Davies, R. Johnston, X. Ge, C. Li, Recent progress of digital reconstruction in polycrystalline materials, *Arch Computat Methods Eng* 32 (2025) 3447–3498. https://doi.org/10.1007/s11831-025-10245-4.
[7] D. Wolf, Correlation between energy, surface tension and structure of free surfaces in fcc metals, *Surf Sci* 226 (1990) 389–406. https://doi.org/10.1016/0039-6028(90)90502-Y.
[8] R. Tran, Z. Xu, B. Radhakrishnan, D. Winston, W. Sun, K.A. Persson, S.P. Ong, Surface energies of elemental crystals, *Sci Data* 3 (2016) 160080. https://doi.org/10.1038/sdata.2016.80.
[9] B. Fu, W. Liu, Z. Li, Calculation of the surface energy of fcc-metals with the empirical electron surface model, *Appl Surf Sci* 256 (2010) 6899–6907. https://doi.org/10.1016/j.apsusc.2010.04.108.
[10] J. Wang, S.-Q. Wang, Surface energy and work function of fcc and bcc crystals: Density functional study, *Surf Sci* 630 (2014) 216–224. https://doi.org/10.1016/j.susc.2014.08.017.
[11] J.J. Guo, K. Wang, T. Fujita, J.W. McCauley, J.P. Singh, M.W. Chen, Nanoindentation characterization of deformation and failure of aluminum oxynitride, *Acta Mater* 59 (2011) 1671–1679. https://doi.org/10.1016/j.actamat.2010.11.034.
[12] Constitutive Equations, in: An Introduction to Continuum Mechanics with Applications, Cambridge University Press, n.d.: pp. 178–209.
[13] Linear fracture mechanics, in: Fracture Mechanics with an Introduction to Micromechanics, Springer, 2006: pp. 49–57. https://doi.org/10.1007/b22134.
[14] S. Satapathy, M. Ahart, D. Dandekar, R.J. Hemley, B. Schuster, P. Khoma, Single-Crystal Elastic Properties of Aluminum Oxynitride (AlON) from Brillouin Scattering, *J Amer Ceram Soc* 99 (2016) 1383–1389. https://doi.org/10.1111/jace.14065.
[15] R. Kiran, K. Choudhary, N. Nguyen-Thanh, Phase-field modeling of brittle anisotropic fracture in polycrystalline materials under combined thermo-mechanical loadings, *Comput Struct* 308 (2025) 107651. https://doi.org/10.1016/j.compstruc.2025.107651.

[16] S. Riad, D. Bardel, J. Réthoré, Unified phase field model to simulate both intergranular and transgranular failure in polycrystalline aggregates, *Finite Elem Anal Des* 194 (2021) 103555. https://doi.org/10.1016/j.finel.2021.103555.
[17] J.D. Clayton, J. Knap, Phase field modeling of directional fracture in anisotropic polycrystals, *Comp Mater Sci* 98 (2015) 158–169. https://doi.org/10.1016/j.commatsci.2014.11.009.

Chapter 6

CONCLUSION: BREAKING THROUGH

Through experiments on both the TGC system and AlON, this thesis has shown that 3D brittle cracks can be tracked and visualized *in situ* and related to phenomena and properties of the anisotropic, inhomogeneous microstructures through which they propagate. Using μ-CT to visualize the crack and second-phase particles, FF-HEDM to obtain information on the mechanical states and orientations of grains encountered by the crack, and NF-HEDM to retrieve grain boundaries and relate them to crack location, comprehensive datasets were created and analyzed.

In the TGC system, the crack in the alkali-aluminosilicate matrix was primarily deflected around the ~15 μm-diameter trevorite particles as a result of residual thermal stresses. However, when the crack would have to deflect significantly (more than 0.45 radians) to continue moving intergranularly, it did not do so. Instead, it cracked through particles transgranularly, or stopped upon reaching the grain and continued after, creating a bridge in the system. In particular, grains with a higher aspect ratio were successful in bridging the crack, and transgranular grains were often larger than the mean, accounting for the greater angle the crack would need to deflect to fracture around them. Orientation of the grain relative to the crack was not a factor in the eventual manner of crack propagation, nor were transgranular or bridging grains observed to have higher or lower stresses in any direction than intergranular ones.

Crack growth in the TGC system was also related to the average stresses experienced by the collective population of grains in the volume ahead of the crack front. When the grains ahead of the crack experienced less tensile stress in the crack opening direction than other volumes at the same load, crack extension occurred in the latter volume first, at lower loads. The volume with depressed stress, meanwhile, reached a higher load before propagating, resulting in an increase in observed fracture toughness.

In AlON, a primary question was whether cracks tended to propagate intergranularly or transgranularly. The cracks actually propagated in both manners, with growth along grain

boundaries not linked to any particular crack orientation. As in the TGC system, geometric considerations were most representative of the way the crack grew rather than orientation or mechanical load. When grain boundaries were close to the crack's profile before the crack reached them, it could gradually shift orientation toward those locations. However, the cracks did not display significant deviation in order to intersect a more distant grain boundary, instead cracking closer grains transgranularly.

AlON also displayed differing fracture toughness between regions and samples. Additionally, it extended irregularly, sometimes through a few grains near the existing crack front, and sometimes by hundreds of microns. It also often did not experience any extension even as the load was increased by hundreds of N. Thus, regions of high fracture toughness existed which could arrest the grain's motions, while other regions experienced greater propagation at smaller load increments and had a smaller fracture toughness.

FF-HEDM grain data was also used to create tessellations for AlON, informed by physical properties including grain radius and centroid, and verified against NF-HEDM maps. The resultant tessellations demonstrated reproducibility when comparing the same region from different sub-volumes and different tessellations. Analyzing tessellations in regions without ground truth NF-HEDM, which was limited in the total volume able to be scanned, allowed larger volumes of grains to be considered as an ensemble and further illuminated aspects of crack growth. Evaluations of specific grains had some uncertainty due to the grain boundaries only being estimates, but when considered as a collective, interesting observations emerge. For example, many grains with lattice plane normals close to the <111> direction oriented along the direction of crack growth were present ahead of the crack front in a location where it stopped extending for 200 N. The {111} planes are preferential crack planes for some spinel materials such as AlON, and their presence may have contributed to those volumes having larger fracture toughness. Additionally, in a possibly related observation, the crack eventually grew on more intergranular planes in that region.

These results together indicate that the entirety of the sample plays a role in eventual crack path and propagation. Individual grains in both AlON and the TGC system which cracked in different manners did not demonstrate noticeable, differentiable trends in orientation or mechanical state. However, ensemble data reveals that collections of grains,

the vector and tensor field properties of which impact each other, can be related to crack motion and arrest. When considering one goal of these experiments, to use them as verification for phase-field models, this reliance on broader volumetric data makes that approach even more promising due to PF models' use of vector and tensor fields.

Beyond elucidating microstructural effects on crack path, a key benefit of these experiments is that by using the DCDC geometry, unstable crack propagation can be avoided. Not only does this setup allow the crack front to be reconstructed at a stable position, but it also allows that process to be performed multiple times. As a result, information about specific volumes' impact on the crack path can be used to calculate values such as fracture toughness; in unstable configurations, these intermediate properties cannot be considered. Capturing the variance in the stress field and fracture toughness throughout the volume, as demonstrated in this thesis, is critical for modeling the crack path and for gaining new insights into the properties affecting crack deflection and inter- versus transgranularity.

This type of multimodal experimental data provides a wealth of information which will aid in developing and ensuring accuracy in anisotropic 3D model systems, including phase-field models. In turn, the vector and tensor fields utilized by models can be used in a variety of operations and calculations, such as the J-integral, which could reveal further relationships between the crack path and the surrounding microstructure and help guide the focus of future experiments. Eventually, given sufficient information about the starting state of a material, including flaws and other heterogeneous aspects, the goal is to be able to produce a fully or partially predictive model using both computation and experimentation. Such models could help determine the best use for or lifetime of a brittle material in a real application.

Even without predictive models, these experiments represent a significant step forward in understanding brittle fracture in real materials. Obtaining and analyzing combined μ-CT and HEDM datasets for many more materials is possible, and encouraged, in order to more fully understand crack paths in brittle materials representing a range of complexity. Sensible next steps would be to perform similar experiments for materials with more anisotropy, a smaller or larger grain size, or a less equiaxed aspect ratio than either TGC or AlON.

Additionally, as synchrotron technologies are continually being upgraded, including the shift to third-generation sources as at the APS and ever-better detectors, further opportunities

will continue to arise. More brilliant sources can improve the quality of the data, and with increased resolution, narrower crack widths may be detected in μ-CT and smaller particles may produce sufficient signal for HEDM analysis, broadening the classes of materials that can be analyzed using these techniques. New sophisticated measurement techniques are also being created, such as point-focused HEDM, which can reveal intragranular and intergranular stresses in a way FF-HEDM cannot. Such stress data would be very useful for examining the local environment around a growing crack front. Additionally, the technique of digital image correlation, already implemented in some workflows at the synchrotron beamlines used in these experiments, could be added to the modalities used in these experiments. This technique tracks deformation and strain on sample surfaces, potentially providing more detail as to how cracks affect brittle materials beyond simply opening them up.

In conclusion, performing multimodal synchrotron techniques leveraging the stable crack propagation of the DCDC geometry has been presented as a novel and viable way to obtain visualizations of a brittle crack front and crack path at multiple stages of growth. Anisotropy and heterogeneity in real-world materials creates more complex crack fronts than idealized models, necessitating a full 3D understanding of their nature, and two such materials are considered here successfully. This work opens up a broad swath of new and exciting directions for both computational and experimental research into brittle fracture with implications for improving reliability and predictability of brittle materials in real-world applications.

SUPPLEMENTAL INFORMATION

S.1 Crack detection protocol in TGC

Step 1: Import .h5 file into ImageJ and save as an Image Sequence of .tiffs

Step 2: Apply the structural and modified median filters, and extract grains

tomoFilter.m

```
scan = '69'; % scan number
state = '1'; % loading step
sample = '02'; % sample number

% find the .tiffs and initialize other folders
imFolder = ['H:/CHESStransfer/dcdc-gc-' sample '/tomo_' scan '/tiffs/'];
baseName = ['s' state '_t' scan '_'];
%altName = ['s4_t179']; %for naming mistakes ie forgetting _
saveFolderStr = ['H:/CHESStransfer/dcdc-gc-' sample '/tomo_' ...
    scan '/filtered_step1/'];
saveFolderFin = ['H:/CHESStransfer/dcdc-gc-' sample '/tomo_' ...
    scan '/filtered_step2/'];
saveFolderGrain = ['H:/CHESStransfer/dcdc-gc-' sample '/tomo_' ...
    scan '/final_grains/'];

baseim = imread([imFolder baseName '0000.tif']); % test image for dimensions
[zDim, xDim] = size(baseim);
yDim = size(dir(imFolder),1) - 2; % directory always counts two extra

% import the corners for the desired sample
bigcorners = [556, 44; 57, 898; 840, 1344; 1340, 489]; % tomo 69, sam2
% move away from the edges to avoid affecting the background mean
% 40 pixels in at 30d angle for sample 02
smallcorners = bigcorners + [18, 24; 24, -18; -18, -24; -24, 18];

% calculate bounding box for ROI around crack
ma = (smallcorners(2,2) - smallcorners(3,2)) / ...
    (smallcorners(2,1) - smallcorners(3,1));
ba = smallcorners(2,2) - ma * smallcorners(2,1);
% hole is located in center of x face
xa = max(round(smallcorners(2,1) + ...
    0.4 * (smallcorners(3,1) - smallcorners(2,1))), 0);
za = max(round(ma * xa + ba), 0); % no values outside the image frame
xb = max(round(smallcorners(2,1) + ...
    0.6 * (smallcorners(3,1) - smallcorners(2,1))), 0);
zb = max(round(ma * xb + ba), 0);

mb = (smallcorners(4,2) - smallcorners(1,2)) / ...
    (smallcorners(4,1) - smallcorners(1,1));
```

```
bb = smallcorners(4,2) - mb*smallcorners(4,1);
md = (smallcorners(2,2) - smallcorners(1,2)) / ...
    (smallcorners(2,1) - smallcorners(1,1));
bd = za - md * xa;
xd = max(round((bd - bb) / (mb - md)), 0);
zd = max(round(md * xd + bd), 0);
xc = max(xd + xb - xa,0);
zc = max(round(mb * xc + bb),0);

roiCorners = [xa,za; xb,zb; xc,zc; xd,zd];

zindices = repmat(1:xDim, [zDim 1]);
xindices = repmat(1:zDim, [xDim 1])';
ROI = inpolygon(xindices, zindices, roiCorners(:,1), roiCorners(:,2));

% set the rectangular structuring element to approximately the size and
% shape of the vertical streaks
recelem = strel('rectangle',[25 3]);

% set the cubic structuring element to extend one pixel in every dir.
cubelem = strel('cube',3);

% structural element filtering
parfor iim = 0:yDim-1
    useim = imread([imFolder, baseName, sprintf('%04d',iim), '.tif']);
    adjim = uint16(useim*1.5e6);
    strim = imopen(adjim,recelem); % open with structural element
    midim = medfilt2(adjim - strim,[1 3]); % top hat

    % save for further filtering
    filtim = Tiff([saveFolderStr, baseName, ...
        sprintf('%04d',iim), '.tif'], 'w');
    tagstr = struct();
    tagstr.ImageLength = size(useim,1);
    tagstr.ImageWidth = size(useim,2);
    tagstr.Photometric = Tiff.Photometric.MinIsBlack;
    tagstr.BitsPerSample = 16;
    tagstr.SamplesPerPixel = 1;
    tagstr.SampleFormat = Tiff.SampleFormat.UInt;
    tagstr.PlanarConfiguration = Tiff.PlanarConfiguration.Chunky;
    tagstr.Compression = Tiff.Compression.None;
    filtim.setTag(tagstr);
    filtim.write(midim);
    filtim.close();
end

parfor islice = 2:yDim-4 % don't use edges because of local stack size
    localStack = int16(zeros(zDim,xDim,3));
    sliceNum = islice + 1;
    % get a stack 5 slices deep
    for jlocal = 1:5
```

```
    localStack(:,:,jlocal) = imread([saveFolderStr, baseName, ...
        sprintf('%04d',sliceNum + jlocal - 3), '.tif']);
end

midim = localStack(:,:,3);
grains = localStack>4000; % find grains
laygrains = midim>4000; % find grains in the central layer
gbw = bwconncomp(laygrains); % get clusters of points in grain binary
gns = bwpropfilt(gbw,'Area',[20 10000]); % remove spurious points
gfilt = cc2bw(gns);
% Save the processed image for the current slice
grainim = Tiff([saveFolderGrain, baseName, ...
    sprintf('%04d',sliceNum + jlocal - 3), '.tif'], 'w');
tagfin = struct();
tagfin.ImageLength = zDim;
tagfin.ImageWidth = xDim;
tagfin.Photometric = Tiff.Photometric.MinIsBlack;
tagfin.BitsPerSample = 8;
tagfin.SamplesPerPixel = 1;
tagfin.SampleFormat = Tiff.SampleFormat.UInt;
tagfin.PlanarConfiguration = Tiff.PlanarConfiguration.Chunky;
tagfin.Compression = Tiff.Compression.None;
grainim.setTag(tagfin);
grainim.write(uint8(gfilt)*255);
grainim.close();

% create random noise around backgroud mean where grains are located so
% bright points aren't included in local background calculations
grainIntens = localStack(grains);
laygrainIntens = midim(laygrains);
numgrainPts = size(grainIntens,1);
rpl = 1000*rand(numgrainPts,1)+1600;
localStack(grains) = rpl;

% open and close with the cubic element to remove noisy points both
% dark and bright
newstack = 0.5*imclose(localStack,cubelem) + ...
    0.5*imopen(localStack,cubelem);
newmidim = newstack(:,:,3);
placeholder = newmidim;

% get median values for regions of different sizes around each point
localenvA = medfilt3(newstack,[3 3 3]);
useenvA = localenvA(:,:,3);
localenvB = medfilt3(newstack,[5 5 5]);
useenvB = localenvB(:,:,3);
localenvC = medfilt3(newstack,[7 7 5]);
useenvC = localenvC(:,:,3);
localenvE = medfilt3(newstack,[11 11 5]);
useenvE = localenvE(:,:,3);
```

```
    % get the mean of each point in the stack at the location to reduce
    % noise and strengthen persistent signals
    deep3d = sum(newstack,3)/5;

    % create conditions for finding the dark and bright crack sections
    % based on analysis of values for representative regions
    crackCheck = deep3d<1600 & useenvB<1600 & useenvC<1800 & ROI;
    darkCheck = ~crackCheck & deep3d<1600 & ~laygrains & ROI;
    artCheck = deep3d>2200 &  useenvB>2200 & useenvC>2000 & ~laygrains & ROI;
    brightCheck = ~artCheck & deep3d>2200 & ~laygrains & ROI;
    otherCheck = ~crackCheck & ~artCheck & ~laygrains & ...
        ~brightCheck & ~darkCheck;

    % strengthen signal for the strongest signals, use a small ROI median
    % filter on those somewhat strong, use a large ROI median filter elsewhere
    placeholder(crackCheck) = 0.75*deep3d(crackCheck);
    placeholder(darkCheck) = useenvA(darkCheck);
    placeholder(artCheck) = 1.2*deep3d(artCheck);
    placeholder(brightCheck) = useenvA(brightCheck);
    placeholder(otherCheck) = useenvE(otherCheck);

    % replace grains in image
    placeholder(laygrains) = laygrainIntens;

    % save filtered image
    portim = Tiff([saveFolderFin, baseName, ...
        sprintf('%04d',islice), '.tif'], 'w');
    tagfin = struct();
    tagfin.ImageLength = size(midim,1);
    tagfin.ImageWidth = size(midim,2);
    tagfin.Photometric = Tiff.Photometric.MinIsBlack;
    tagfin.BitsPerSample = 16;
    tagfin.SamplesPerPixel = 1;
    tagfin.SampleFormat = Tiff.SampleFormat.Int;
    tagfin.PlanarConfiguration = Tiff.PlanarConfiguration.Chunky;
    tagfin.Compression = Tiff.Compression.None;
    portim.setTag(tagfin);
    portim.write(placeholder);
    portim.close();
end
```

Step 3: Use ImageJ to Enhance Contrast and normalize for the top and bottom 1% of pixels in the entire image sequence, and save

Step 4: Get connected components after thresholding and filter them by size and location to find those belonging to the crack

`bwPropFilter.m`

```
scan = '69'; % scan number
```

```
state = '1'; % state number
sample = '02'; % sample number
baseFolder = ['H:/CHESStransfer/dcdc-gc-' sample '/tomo_' scan ...
    '/contrast/s' state '_t' scan '_'];
saveFolder = ['H:/CHESStransfer/dcdc-gc-' sample '/tomo_' scan ...
    '/final_crack_bins/s' state '_t' scan '_'];
baseim = imread([baseFolder '0000.tif']); % sample image for dimensions
[zDim, xDim] = size(baseim);
yDim = size(dir(['H:/CHESStransfer/dcdc-gc-' sample '/tomo_' scan ...
    '/contrast/']),1) - 2;

% same procedure for ROI as in tomoFilter.m
bigcorners = [556, 44; 57, 898; 840, 1344; 1340, 489]; % tomo 69, sam2
smallcorners = bigcorners + [18, 24; 24, -18; -18, -24; -24, 18]; % sam2

zindices = repmat(1:xDim,[zDim 1]);
xindices = repmat(1:zDim,[xDim 1])';
bigROI = inpolygon(xindices, zindices, smallcorners(:,1), smallcorners(:,2));

ma = (smallcorners(2,2) - smallcorners(3,2)) / ...
    (smallcorners(2,1) - smallcorners(3,1));
ba = smallcorners(2,2) - ma * smallcorners(2,1);
xa = max(round(smallcorners(2,1) + ...
    0.45 * (smallcorners(3,1) - smallcorners(2,1))), 0);
za = max(round(ma * xa + ba), 0);
xb = max(round(smallcorners(2,1) + ...
    0.55 * (smallcorners(3,1) - smallcorners(2,1))), 0);
zb = max(round(ma * xb + ba), 0);

mb = (smallcorners(4,2) - smallcorners(1,2)) / ...
    (smallcorners(4,1) - smallcorners(1,1));
bb = smallcorners(4,2) - mb * smallcorners(4,1);
md = (smallcorners(2,2) - smallcorners(1,2)) / ...
    (smallcorners(2,1) - smallcorners(1,1));
bd = za - md * xa;
xd = max(round((bd - bb) / (mb - md)), 0);
zd = max(round(md * xd + bd), 0);
xc = max(xd + xb - xa,0);
zc = max(round(mb * xc + bb), 0);

roiCorners = [xa,za; xb,zb; xc,zc; xd,zd];

% get edge pixels for the crack ROI
smallROI = inpolygon(xindices, zindices, roiCorners(:,1),roiCorners(:,2));
longEdge = round(sqrt((xa-xd)^2 + (za-zd)^2));
shortEdge = abs(xa-xb);
xBegin = round(linspace(xa,xd,longEdge));
xFinal = round(linspace(xb,xc,longEdge));
xCen = round((xBegin+xFinal)/2);
zBegin = round(linspace(za,zd,longEdge));
zFinal = round(linspace(zb,zc,longEdge));
```

```
zCen = round((zBegin+zFinal)/2);

goodCrack = false(zDim,xDim,yDim);

parfor iyslice = 0:yDim-2
    testim = im2int16(imread(sprintf([baseFolder '%04d.tif'],iyslice)));
    crackbw = testim<-24000 & bigROI; % get points below threshold
    cc = bwconncomp(crackbw);
    cnc = bwpropfilt(cc, 'Circularity', [0 0.7]); % keep noncircular
    co = bwpropfilt(cnc,'Orientation',[-30 45]); % some deviation, esp near hole
    cbm = bwpropfilt(co, 'MinorAxisLength', [50 500]); %keep hole remnants
    csm = bwpropfilt(co, 'MinorAxisLength', [0 12]); % rest is lines
    cf = cc2bw(cbm) + cc2bw(csm);
    cfc = bwconncomp(cf);

    % good bright crack pixels are similar to the dark ones but as they
    % are deeper in the sample, will be straighter
    artbw = testim>-15000 & testim < -10000 & bigROI;
    ac = bwconncomp(artbw);
    anc = bwpropfilt(ac, 'Circularity', [0 0.3]); % more rigorous
    ao = bwpropfilt(anc, 'Orientation', [30 60]);
    asm = bwpropfilt(ao, 'MinorAxisLength', [0 12]);

    % combine both bright and dark results and keep those with
    % centroids in the ROI
    combo = cc2bw(asm) + cc2bw(cfc);
    combocc = bwconncomp(combo);
    numGroups = length(combocc.PixelIdxList);
    cents = regionprops(combocc, 'Centroid');

    for igroup = 1:numGroups
        gcent = cents(igroup).Centroid;
        if ~inpolygon(gcent(2), gcent(1), roiCorners(:,1), roiCorners(:,2))
            combocc.PixelIdxList{igroup} = [];
            combo = cc2bw(combocc);
        end
    end

    % use the edge pixels to create line scans perpendicular to the crack
    % and since there is only one crack, if multiple components intersect
    % with the line scan, keep the one closest to the center of the ROI
    for ix = 1:longEdge
        % get the values for the bounding box edges
        xProf = xBegin(ix):xFinal(ix);
        proflen = length(xProf);
        zProf = round(linspace(zBegin(ix), zFinal(ix), proflen));
        intersectdat = [];
        % find components in touching the line
        for iz = 1:proflen
            for ig = 1:numGroups
                locinIm = sub2ind(size(testim), xProf(iz), zProf(iz));
```

```
            if any(combocc.PixelIdxList{ig} == locinIm)
                intersectdat = [intersectdat; ig iz];
            end
        end
    end

    % if the line intersects multiple groups, find which they are, keep
    % the ones closest to the center, and delete the others so they
    % aren't intersected again
    if ~isempty(intersectdat) & size(unique(intersectdat(:,1)),1) > 1
        groupInter = unique(intersectdat(:,1));
        numInter = size(groupInter,1);
        ceninterdat = zeros(numInter,2);
        % get the mean for that line
        for jinter = 1:numInter
            ingroup = intersectdat(:,1)==groupInter(jinter);
            ceninterdat(jinter,:) = [groupInter(jinter)...
                mean(intersectdat(ingroup,2))];
        end
        dtocen = abs(shortEdge/2-ceninterdat(:,2));
        [~,closecen] = min(dtocen);
        grouptokeep = ceninterdat(:,1)==ceninterdat(closecen,1);
        badgroups = ceninterdat(~grouptokeep);
        % zero out the points in the non-chosen groups
        for ibad = 1:length(badgroups)
            if size(combocc.PixelIdxList{badgroups(ibad)},1) < 200
                combocc.PixelIdxList{badgroups(ibad)} = [];
                combo = cc2bw(combocc);
            end
        end
    elseif ~isempty(intersectdat)
        intergroup = intersectdat(1,1);
        numgroup = size(combocc.PixelIdxList{intergroup},1);
        zdtocen = abs(mean(intersectdat(:,2))-shortEdge/2);
        if zdtocen > 25 && numgroup < 200
            combocc.PixelIdxList{intergroup} = [];
            combo = cc2bw(combocc);
        end
    end
end

% if too few points total in the slize, zero it all out
pcttrue = length(find(combo))/zDim/xDim;
if pcttrue <= 1.5e-4
   combo = false(zDim,xDim);
end

% save final images
portim = Tiff(sprintf([saveFolder '%04d_final_pts.tif'],iyslice), 'w');
tag = struct();
tag.ImageLength = zDim;
```

```
    tag.ImageWidth = xDim;
    tag.Photometric = Tiff.Photometric.MinIsBlack;
    tag.BitsPerSample = 8;
    tag.SamplesPerPixel = 1;
    tag.SampleFormat = Tiff.SampleFormat.UInt;
    tag.PlanarConfiguration = Tiff.PlanarConfiguration.Chunky;
    tag.Compression = Tiff.Compression.None;
    portim.setTag(tag);
    portim.write(uint8(combo)*255);
    portim.close();
end
```

Step 5: Use ImageJ to Enhance Contrast and normalize for the top and bottom 1% of pixels in the entire image sequence, and save

Step 6: Use .h5 detector metadata to align find the x and z points that align for consecutive tomo scans, and fiducial markers (grain shapes) to find where the overlap in y is for consecutive scans

Step 7: Stack all scans into a single image sequence and keep points with a high incidence across multiple layers

alignmentTomo.m

```
groupNum = 1;
firstScan = 64;
numScans = 3;
scanStep = 5;
% each scan had a bright field and dark field before and after so the true
% scans are spaced 5 apart
scans = firstScan:scanStep:firstScan+scanStep*(numScans-1);
bigDir = 'H:/CHESStransfer/dcdc-gc-02/tomo_';
grainDir = '/final_grains/';
crackDir = '/final_crack_bins/';
saveDir = ['H:/CHESSresults/tomo_s' num2str(groupNum) '/'];
gsDir = 'aligned_grains/';
csDir = 'initial_alignment_crack/';
lims = zeros(3,2,numScans);

% s1, pixel limits from aligning known real locations [x; z; y (slice)]
% in y, keep the slices more centered in their respective scan instead of edges
lims(:,:,1) = [81, 1400; 1, 1320; 87, 700]; % 64
lims(:,:,2) = [44, 1363; 34, 1353; 65, 588]; % 69
lims(:,:,3) = [9, 1328; 32, 1351; 2, 608]; % 74

% finish alignment
totalNumIms = sum(lims(3,2,:)) - sum(lims(3,1,:)) + numScans;
finxDim = lims(2,2,1) - lims(2,1,1)+1;
finzDim = lims(1,2,1) - lims(1,1,1)+1;
```

```
orderIms = [lims(3,2,1):-1:lims(3,1,1) ...
    lims(3,2,2):-1:lims(3,1,2) ...
    lims(3,2,3):-1:lims(3,1,3)];
scanOrder = [ones(1, lims(3,2,1) - lims(3,1,1)+1) ...
    2*ones(1, lims(3,2,2) - lims(3,1,2)+1) ...
    3*ones(1, lims(3,2,3) - lims(3,1,3)+1)];

%set metadata for images
tag = struct();
tag.ImageLength = finzDim;
tag.ImageWidth = finxDim;
tag.Photometric = Tiff.Photometric.MinIsBlack;
tag.BitsPerSample = 8;
tag.SamplesPerPixel = 1;
tag.SampleFormat = Tiff.SampleFormat.UInt;
tag.PlanarConfiguration = Tiff.PlanarConfiguration.Chunky;
tag.Compression = Tiff.Compression.None;

% stack initial images
parfor iim = 1:totalNumIms
    iscan = scanOrder(iim);
    iscanNum = scans(iscan);
    islice = orderIms(iim);
    imlims = lims(:,:,iscan);

    % grains
    fullgim = imread([bigDir num2str(iscanNum) '\final_grains\s' ...
        num2str(groupNum) '_t' num2str(iscanNum) ...
        sprintf('_%04d.tif',gslice)]);

    cropgim = fullgim(imlims(1,1):imlims(1,2),imlims(2,1):imlims(2,2));

    grainim = Tiff(sprintf([saveDir gsDir 'grains_%04d.tif'],iim), 'w');
    grainim.setTag(tag);
    grainim.write(cropgim);
    grainim.close();

    % crack
    fullcim = imread([bigDir num2str(iscanNum) '\final_crack_bins\s' ...
        num2str(groupNum) '_t' num2str(iscanNum) ...
        sprintf('_%04d',islice) '_final_pts.tif']);
    cropcim = fullcim(imlims(1,1):imlims(1,2),imlims(2,1):imlims(2,2));

    crackim = Tiff(sprintf([saveDir csDir 'crack_%04d.tif'], iim), 'w');
    crackim.setTag(tag);
    crackim.write(cropcim);
    crackim.close();
end

finDir = 'clean_crack/';
```

```
%s1 hole locations in y, for different treatment
holeConTop = 644;
holeConBot = 704;

% create bins of 100 slices, to be used to filter the center 50 images in
% the bin
startBlockA = 1:50:holeConTop-100;
endBlockA = 100:50:holeConTop;
lastProcBlockA = endBlockA(end) - 25;

startBlockB = flip(totalNumIms-99:-50:holeConBot);
endBlockB = flip(totalNumIms:-50:holeConBot+100);
lastProcBlockB = startBlockB(1)+25;

startBins = [startBlockA,lastProcBlockA+1,startBlockB];
endBins = [endBlockA,lastProcBlockB-1,endBlockB];

% different bin containing images with the hole
cenBin = find(startBins==lastProcBlockA+1);

binSizes = endBins-startBins+1;
% 8 images out of 100 worked the best; larger than many small grains that might
% be counted as noise, but small enough that deflections in the crack away from
% straight can still be captured
binMinReach = 255*8*ones(size(startBins));
%crack wiggles more near crack so needs less intensity to keep
binMinReach(cenBin-1:cenBin+1) = 255*6*ones(1,3);

numBins = length(startBins);
parfor ibin = 1:numBins
    if ibin~=cenBin && ibin~=cenBin-1 && ibin~=cenBin+1
        sizehere = binSizes(ibin);
        startim = startBins(ibin);
        endim = endBins(ibin);
        locims = startim:endim;
        locstack = uint8(zeros(finzDim,finxDim,sizehere));
        for jim = 1:sizehere
            locstack(:,:,jim) = imread(sprintf([saveDir csDir ...
                'crack_%04d.tif'], locims(jim)));
        end
        sumim = sum(double(locstack),3);
        badlocs = find(sumim<binMinReach(ibin));
        figure,imagesc(sumim)
        for kcheck = 26:75
            useim = locstack(:,:,kcheck);
            useim(badlocs) = uint8(zeros(size(badlocs)));

            cleanim = Tiff(sprintf([saveDir finDir 'crack_%04d.tif'], ...
                locims(kcheck)), 'w');
            cleanim.setTag(tag);
            cleanim.write(useim);
```

```
            cleanim.close();
        end
    else
        %at center there is no crack, keep all points
        for kim = lastProcBlockA:lastProcBlockB-1
            origim = imread(sprintf([saveDir csDir 'crack_%04d.tif'],kim));
            bwim = Tiff(sprintf([saveDir finDir ...
                'crack_%04d.tif'], kim), 'w');
            bwim.setTag(tag);
            bwim.write(origim);
            bwim.close();
        end
    end
end
```

Step 8: Find the crack edges and crack front to determine its length

```
crackEdgeFinder.m

pxSize = 0.00148;
crackPts = cell(1,4);
cracklens = zeros(4,8);
numStates = 4; % number of total extension events

for state = 1:4

    % find the images
    crackFolder = (['H:/CHESSresults/tomo_s' num2str(state) ...
        '/clean_crack/']);
    numFiles = size(dir(crackFolder),1) - 2; % extra two in directoy

    firstYcen = -6.15; % position of the hole center at zero load, in mm

    maxpts = [];

    % image limits in all coordinates
    if state == 1
        xVals = -1.07670:pxSize:0.87542;
        zVals = -1.23358:pxSize:0.71854;
        yVals = -7.07008:pxSize:-4.48896;
        % the images tend to still have noise at the very edges, so make
        % sure that isn't included by stopping the program from including
        % those
        imlims = [1,1200];
        yCen = -6.077; % position of the hole center at this load, in mm
    elseif state == 2
        xVals = -1.09002:pxSize:0.83;
        zVals = -1.24838:pxSize:0.70374;
        yVals = -7.88408:pxSize:-4.44012;
        imlims = [584,1916];
        yCen = -6.077;
```

```
    elseif state == 3
        xVals = -1.04118:pxSize:0.91094;
        zVals = -1.24838:pxSize:0.70374;
        yVals = -8.25652:pxSize:-4.03704;
        imlims = [700,2400];
        yCen = -6.038;
    elseif state == 4
        xVals = -1.02638:pxSize:0.91094;
        zVals = -1.23358:pxSize:0.71854;
        yVals = -8.57708:pxSize:-3.54656;
        imlims = [595,3155];
        yCen = -6.067;
    end

    holeMidBot = yCen + 0.043;
    holeMidTop = yCen - 0.043; % where the cones intersect
    holeBot = yCen + 0.215;
    holeTop = yCen - 0.215; % where the crack first/last appears
    yCenShift = yCen-firstYcen;

    for ifile = imlims(1):imlims(2)
        % import the binary image
        crackim = imread(sprintf([crackFolder 'crack_%04d.tif'],ifile));
        bwp = find(crackim);
        % if the image isn't just noise, find the crack extrema for the 2d
        % slice and record all values and depths
        if length(bwp)>100
            % points on image with crack
            [imr,imc] = ind2sub([size(crackim,1), size(crackim,2)], bwp);
            crackr = xVals(imr);
            crackc = zVals(imc);
            imy = yVals(ifile);
            % get the min and max in x and corresponding z, and the min and
            % max in z and corresponding x, and calculate average endpoints
            ptA = mean([min(crackr) mean(crackc(crackr==min(crackr))); ...
                mean(crackr(crackc==max(crackc))) max(crackc)]);
            ptB = mean([max(crackr) mean(crackc(crackr==max(crackr))); ...
                mean(crackr(crackc==min(crackc))) min(crackc)]);
            maxpts = [maxpts;ptA imy ptB imy];
        end
    end
    numLays = size(maxpts,1);

% due to variation in where the extrema are located on each slice, the
    % actual edge is very jagged and sometimes disappears altogether, so ti
    % must be mitigated
    xA = smooth(maxpts(:,1),0.1);
    zA = smooth(maxpts(:,2),0.1);
    xB = smooth(maxpts(:,4),0.1);
    zB = smooth(maxpts(:,5),0.1);
```

```
% find the points where even after smoothing, the crack edge becomes
% very jumpy (where only a few points are found); search within the
% last 50 points marked for simplicity
jumpAbot = 50 - max([find(abs(diff(flip(zA(1:50))))>0.01,1) ...
    find(abs(diff(flip(xA(1:50))))>0.01,1)]);
jumpAtop = min([find(abs(diff(zA(numLays-49:numLays)))>0.01,1), ...
    find(abs(diff(xA(numLays-49:numLays)))>0.01,1)]) + numLays - 50;

jumpBbot = 50 - max([find(abs(diff(flip(zB(1:50))))>0.01,1) ...
    find(abs(diff(flip(xB(1:50))))>0.01,1)]);
jumpBtop = min([find(abs(diff(zB(numLays-49:numLays)))>0.01,1), ...
    find(abs(diff(xB(numLays-49:numLays)))>0.01,1)]) + numLays - 50;

% the crack in the original images is rotated, so rotate it into a
% near-planar position for ease of calculation
skewR = [cos(pi/6) sin(pi/6) 0;-sin(pi/6) cos(pi/6) 0; 0 0 1];
skewptsA = (skewR*maxpts(:,1:3)')';
skewptsB = (skewR*maxpts(:,4:6)')';
newpts = [skewptsA(:,2:3),skewptsB(:,2:3)];

% initialize
newpts(1:jumpAbot,1:2) = nan(jumpAbot,2);
newpts(jumpAtop:numLays,1:2) = nan(numLays-jumpAtop+1,2);
newpts(1:jumpBbot,3:4) = nan(jumpBbot,2);
newpts(jumpBtop:numLays,3:4) = nan(numLays-jumpBtop+1,2);

% get the last 5 points before the identified jumpiness
smoothZ = [smooth(newpts(:,1),0.1) newpts(:,2) ...
    smooth(newpts(:,3),0.1) newpts(:,4)];
lastptsA = smoothZ(jumpAbot+1:jumpAbot+5,1:2);
lastptsB = smoothZ(jumpBbot+1:jumpBbot+5,3:4);

% make a parabola connecting the last points with a deeper
% point identified before the jumpy points were suppressed
pflast = polyfit([lastptsA(1,1), mean([zA;zB]), lastptsB(1,1)],...
    [lastptsA(1,2), mean(maxpts(1:min([jumpAbot,jumpBbot]), 3)), ...
    lastptsB(1,2)], 2);

% get points along the prospective crack front and calculate the
% expected depth along it
testzbot = linspace(lastptsA(1), lastptsB(1), jumpAbot+jumpBbot);
testybot = pflast(1) * testzbot.^2 + pflast(2) * testzbot + pflast(3);

% connect all points into a single front
smoothZ(1:jumpAbot,1:2) = [testzbot(jumpAbot:-1:1); ...
    testybot(jumpAbot:-1:1)]';
smoothZ(1:jumpBbot,3:4) = [testzbot(jumpAbot+1:jumpAbot+jumpBbot); ...
    testybot(jumpAbot+1:jumpAbot+jumpBbot)]';

% do the same with the crack on the other half of the sample
numAtop = numLays-jumpAtop + 1;
```

```
    numBtop = numLays-jumpBtop + 1;
    firstptsA = smoothZ(jumpAtop-5:jumpAtop-1,1:2);
    firstptsB = smoothZ(jumpBtop-5:jumpBtop-1,3:4);
    pffirst = polyfit([firstptsA(1,1), mean([zA;zB]),firstptsB(1,1)],...
        [firstptsA(1,2), ...
        mean(maxpts(max([jumpAtop,jumpBtop]):numLays,3)), ...
        firstptsB(1,2)], 2);
    testztop = linspace(firstptsA(1),firstptsB(1),numAtop+numBtop);
    testytop = pffirst(1)*testztop.^2 + pffirst(2)*testztop + pffirst(3);
    smoothZ(jumpAtop:numLays,1:2) = [testztop(1:numAtop); ...
        testytop(1:numAtop)]';
    smoothZ(jumpBtop:numLays,3:4) = [testztop(numAtop+numBtop:-1:numAtop+1); ...
        testytop(numAtop+numBtop:-1:numAtop+1)]';

    % combine all points from top and bottom
    allPtsRd = [smoothZ(:,1:2);flip(smoothZ(:,3:4))]; %;smoothZ(1,1:2)];
    crackPts{state} = allPtsRd;

    % calculate the crack lengths and errors from the top and bottom holes
    botmax = max(allPtsRd(:,2));
    % crack error (longer): deepest point identified originally
    botErrmax = max(maxpts(:,3)) - botmax;
    % crack error (shorter): deepest point before jumpiness
    botErrmin = max(jumpAbot,jumpBbot)*pxSize;
    obotlen = botmax - holeBot;
    ibotlen = botmax - holeMidBot;
    topmax = min(allPtsRd(:,2));
    topErrmax = topmax - min(maxpts(:,3));
    topErrmin = min(numAtop,numBtop)*pxSize;
    otoplen = holeTop - topmax;
    itoplen = holeMidTop - topmax;

    cracklens(state,:) = [obotlen ibotlen botErrmax botErrmin ...
        itoplen otoplen topErrmax topErrmin];
end
```

S.2 Crack detection protocol in AlON

Step 1: Find the places in each consecutive tomography scan where overlap begins and average the overlapping scans for each y position due to noisiness on the edges

Step 2: Denoise the stacked images then apply a 3D non-local means filter with automatically estimated parameters to the whole stack, followed by a 2D non-local means filter on each individual slice to remove localized artifacts

Step 3: Classify points in the images as the crack so they can be registered with HEDM grains

fullTomoStitch.m

```
% import tiffs
state = 's1'; % tomography state number

baseFolder = ['K:\tomo_stitches\good\' state '_3dLMN_median_2dLMN\'];
totFiles = length(dir(baseFolder)) -2;
startNum = 10;
endNum = totFiles - 11;
startFileName = Tiff([baseFolder state num2str(startNum,'%04.0f') ...
    '.tif'], 'r');

pxSize = 1.172;

dims = size(read(startFileName));
dimsY = dims(1);
dimsX = dims(2);

% get an image from the end for basic parameters
blankIm = read(Tiff([baseFolder state num2str(totFiles-10,'%04.0f') ...
    '.tif'], 'r'));
% blur it out so no extra lines show up
blurIm = imgaussfilt(blankIm,2);
% use a Hough transform to find the sample edges
[H,theta,rho] = hough(edge(blurIm,'Canny'), 'RhoResolution', 1, ...
    'Theta', -90:0.05:89);
hPks = houghpeaks(H,10);
hLns = houghlines(edge(blurIm), theta, rho, hPks);
lineRh = [hLns.rho];
goodLns = unique(lineRh(1,:));
slopes = zeros(1,4);
intercs = zeros(1,4);
% sometimes a line is broken up but has the same angle, use only one
for iline = 1:length(goodLns)
    loc = find(lineRh==goodLns(iline));
    if length(loc) > 1
        lineLens = zeros(1,length(loc));
        for mark = 1:length(loc)
            y1 = hLns(loc(mark)).point1(1);
            x1 = hLns(loc(mark)).point1(2);
            y2 = hLns(loc(mark)).point2(1);
            x2 = hLns(loc(mark)).point2(2);
            lineLens(mark) = sqrt((y2 - y1)^2 + (x2 - x1)^2);
        end
        longest = find(lineLens == max(lineLens));
        goodNum = loc(longest);
    else
        goodNum = loc;
    end

    % store slope and intercept data
```

```
    lineData = hLns(goodNum);
    y1 = lineData.point1(1);
    x1 = lineData.point1(2);
    y2 = lineData.point2(1);
    x2 = lineData.point2(2);
    slopes(iline) = (y2 - y1) / (x2 - x1);
    intercs(iline) = y2 - slopes(iline) * x2;
end

% make sure no vertical lines
goodslopes = zeros(1,4);
goodintercs = zeros(1,4);
kline = 1;
for jlinecheck = 1:length(slopes)
    if abs(slopes(jlinecheck)) ~= Inf
        goodslopes(kline) = slopes(jlinecheck);
        goodintercs(kline) = intercs(jlinecheck);
        kline = kline+1;
    end
end
slopes = goodslopes;
intercs = goodintercs;

% get the corners by intersecting the lines
[sortSlopes,sortOrder] = sort(slopes);
sortIntercs = intercs(sortOrder);
cornerPts = zeros(2,4);
fillPt = 1;
for ipoint = 1:2
    usePoint = sortOrder(ipoint);
    for secondary = 3:4
        secondPoint = sortOrder(secondary);
        xPoint = (intercs(secondPoint) - intercs(usePoint)) / ...
            (slopes(usePoint) - slopes(secondPoint));
        % if points are outside the image dimensions, set them to within
        % the image
        if xPoint < 1
            cornerPts(1,fillPt) = 1;
        elseif xPoint > dimsX
            cornerPts(1,fillPt) = dimsX;
        else
            cornerPts(1,fillPt) = round(xPoint);
        end
        yPoint = slopes(usePoint) * xPoint + intercs(usePoint);
        if yPoint < 1
            cornerPts(2,fillPt) = 1;

        elseif yPoint > dimsY
            cornerPts(2,fillPt) = dimsY;
        else
            cornerPts(2,fillPt) = round(yPoint);
```

```
        end
        fillPt = fillPt+1;
    end
end

% use the corners to calculate final slopes
miny = min(cornerPts(2,:));
xatminy = cornerPts(1, cornerPts(2,:)==miny);
maxy = max(cornerPts(2,:));
xatmaxy = cornerPts(1, cornerPts(2,:)==maxy);
minx = min(cornerPts(1,:));
yatminx = cornerPts(2, cornerPts(1,:)==minx);
maxx = max(cornerPts(1,:));
yatmaxx = cornerPts(2, cornerPts(1,:)==maxx);

mA = (miny - yatminx) / (xatminy - minx);
bA = miny - mA*xatminy;
mB = (yatmaxx - miny) / (maxx - xatminy);
bB = yatmaxx - mB * maxx;
mC = (maxy - yatminx) / (xatmaxy - minx);
bC = maxy - mC * xatmaxy;
mD = (yatmaxx  -maxy) / (maxx - xatmaxy);
bD = yatmaxx - mD * maxx;

% find the edge points in x
xRange = minx:maxx;
xRangeA = minx:xatminy;
xRangeB = xatminy+1:maxx;
xRangeC = minx:xatmaxy;
xRangeD = xatmaxy+1:maxx;

% calculate the edge points in z
upperLimA = round(mA * xRangeA + bA);
upperLimB = round(mB * xRangeB + bB);
upperLim = [upperLimA upperLimB];
lowerLimC = round(mC * xRangeC + bC);
lowerLimD = round(mD  *xRangeD + bD);
lowerLim = [lowerLimC lowerLimD];

% set threshold limits
whiteMask = 1;
blackMask = 1.25;
strongBlackMask = 1.5;
mostBlackMask = 2;

% initialize storage
peaks = cell(1,totFiles);
chasms = cell(1,totFiles);
loners = cell(1,totFiles);
valleys = cell(1,totFiles);
```

r

```
%% initial point identification

parfor ilayer = startNum:endNum
    % set initial points in the layer to be blank
    imStack = zeros(dimsY,dimsX);
    whiteStackWgts = zeros(dimsY,dimsX);
    whiteStack = false(dimsY,dimsX);
    blackStack = true(dimsY,dimsX);
    strongBlackStack = blackStack;
    mostBlackStack = blackStack;

    % make a localized stack of 11 images for each center
    for jline = 1:11
        imLay = jline-6;
        imStack(:,:,jline) = double(read(Tiff([baseFolder state ...
            num2str(ilayer - imLay,'%04.0f') '.tif'], 'r')));
    end

    im2Use = imStack(:,:,6); % center image

    % get the overall stack properties
    tomoMean = mean(imStack, 'all');
    tomoStd = std(imStack, 0, 'all');

    % for each value in x, find the corresponding z values marking the
    % sample edges, then using the environment around a point (x,z) find if
    % it matches any of the thresholds
    for kx = minx:maxx
        xLoc = find(xRange==kx);
        zLims = [upperLim(xLoc), lowerLim(xLoc)];
        zStart = min(zLims);
        zEnd = max(zLims);

        % relevant region to be used for calculations can't extend past
        % image limits, so set appropriate limits
        if kx<21
            krangebot = 1;
            krangetop = kx + 20;
        elseif kx>dimsX-21
            krangebot = kx - 20;
            krangetop = dimsX;
        else
            krangebot = kx - 20;
            krangetop = kx + 20;
        end

        for jz = zStart:zEnd
            % limits in z
            if jz<21
                jrangebot = 1;
                jrangetop = jz + 20;
```

```
        elseif jz>dimsY-21
            jrangebot = jz - 20;
            jrangetop = dimsY;
        else
            jrangebot = jz - 20;
            jrangetop = jz + 20;
        end

        % find the mean and standard deviation in the region around
        % each point to modify the overall image values with
        localSubset = imStack(krangebot:krangetop, ...
            jrangebot:jrangetop, :);
        localMean = mean(localSubset, 'all');
        localStd = std(localSubset, 0, 'all');

        % let the mean be the average of image and local means
        useMean = 0.5 * localMean + 0.5 * tomoMean;
        % let the standard deviation rely more on the local value than
        % overall
        useStd = 0.75 * localStd + 0.25 * tomoStd;

        % the bright parts are an upper threshold, find if matching the
        % requirement
        whiteMin = useMean + whiteMask * useStd;
        if im2Use(kx,jz) > whiteMin
            whiteStackWgts(kx,jz) = (65535 - im2Use(kx,jz)) / ...
                (65535 - whiteMin);
            whiteStack(kx,jz) = true;
        end

        % apply the three different dark thresholds
        if imStack(kx,jz) < (useMean - blackMask * useStd)
            blackStack(kx,jz) = false;
        end
        if imStack(kx,jz) < (useMean - strongBlackMak * useStd)
            strongBlackStack(kx,jz) = false;
        end
        if imStack(kx,jz) < (useMean - mostBlackMask * useStd)
            mostBlackStack(kx,jz) = false;
        end
    end
end

% initialize the types of point being looked for
layPeaks = [];
layChasms = [];
layValleys = [];
layLoners = [];

% again look for points
for ax = minx:maxx
```

```
xLoc = find(xRange==ax);
zLims = [upperLim(xLoc), lowerLim(xLoc)];
zStart = min(zLims);
zEnd = max(zLims);

for bz = zStart:zEnd

    % count a bright point as a peak if it has dark shadows on
    % either side
    if whiteStack(ax,bz) == 1 && ...
            any(~blackStack(ax, bz-10:bz-1)) && ...
            any(~blackStack(ax, bz+1:bz+10))
        layPeaks = [layPeaks;bz,ax];
    end

    % three different criteria being checked for dark points
    if blackStack(ax,bz) == 0
        leftCheck = 0;
        rightCheck = 0;
        leftBright = 0;
        rightBright = 0;
        backwardWhiteWeights = 10:-1:1;

        % find out if there's a brighter peak on either side of a
        % dark point within 10 pixels
        for range = 1:10
            if whiteStackWgts(ax,bz-range) ~= 0
                leftCheck = leftCheck + 1;
                leftBright = leftBright + ...
                    whiteStackWgts(ax, bz-range) * ...
                    backwardWhiteWeights(range);
            end
            if whiteStackWgts(ax,bz+range) ~= 0
                rightCheck = rightCheck + 1;
                rightBright = rightBright + ...
                    whiteStackWgts(ax, bz+range) * ...
                    backwardWhiteWeights(range);
            end
        end

        % if bright neighbors were found, weight by how wide they
        % are
        if leftCheck > 0
            leftBright = leftBright / leftCheck;
        end
        if rightCheck > 0
            rightBright = rightBright / rightCheck;
        end

        % if both peaks are there, they don't have to be that big
```

```
                % for the point to be recorded as a crack. One sufficiently
                % wide peak beside the dark point is also good. Then very
                % dark points are always recorded as crack points
                if leftCheck >= 4 && rightCheck >= 4
                    layValleys = [layValleys;bz,ax];
                elseif (leftCheck >= 8 || rightCheck >= 8) && ...
                        strongBlackStack(ax,bz) == 0
                    layChasms = [layChasms;bz,ax];
                else
                    if mostBlackStack(ax,bz) == 0
                        layLoners = [layLoners;bz,ax];
                    end
                end
            end
        end
    end
    peaks{ilayer} = layPeaks;
    valleys{ilayer} = layValleys;
    chasms{ilayer} = layChasms;
    loners{ilayer} = layLoners;
end

%% combine all the dark points and bright points from different y slices

allpts = [];
allpks = [];
for ilayer = startNum:endNum
    if ~isempty(valleys{ilayer})
        vecpts = [valleys{ilayer}, ilayer * ones(size(valleys{ilayer},1), 1)];
        allpts = [allpts; vecpts(:,1), vecpts(:,2), vecpts(:,3)];
    end
    if ~isempty(chasms{ilayer})
        vecpts = [chasms{ilayer}, ilayer * ones(size(chasms{ilayer},1), 1)];
        allpts = [allpts; vecpts(:,1), vecpts(:,2), vecpts(:,3)];
    end
    if ~isempty(loners{ilayer})
        vecpts = [loners{ilayer}, ilayer * ones(size(loners{ilayer},1), 1)];
        allpts = [allpts; vecpts(:,1), vecpts(:,2), vecpts(:,3)];
    end
    if ~isempty(peaks{ilayer})
        vecpts = [peaks{ilayer}, ilayer * ones(size(peaks{ilayer},1), 1)];
        allpks = [allpks; vecpts(:,1), vecpts(:,2), vecpts(:,3)];
    end
end

%% fill in gaps, reduce noise, and check for bright regions
% indicating a narrow crack

numpts = size(allpts,1);

% find all unique(x,z) points the crack was found on in any layer
```

```
[xypts,~,~] = unique(allpts(:,1:2), 'rows');
numUniqueXY = size(xypts, 1);
morepts = cell(1,numUniqueXY);

% some points recorded as peaks are just artifacts, but some represent the
% crack when it was very thin
parfor ipt = 1:numUniqueXY

    % create a line of all marked points for each (x,z) point
    parXY = xypts(ipt,:);
    linecrack = sort(allpts(allpts(:,1)==parXY(1) & ...
        allpts(:,2)==parXY(2), 3));
    whiteArt = sort(allpks(allpks(:,1)==parXY(1) & ...
        allpks(:,2)==parXY(2), 3));
    parNum = 0;
    parCrack = [];

    % crack needs to be sufficiently long not to be nosie
    if length(linecrack) > 5
        % the crack might move away and back to a point as the crack
        % changes orientation
        spacing = diff(linecrack);
        jumps = find(spacing>1);

        % if there are not too many jumps, analyze
        if length(jumps) < length(linecrack)/3
            % move jump by jump to test crack locations
            check = 1;
            while ~isempty(jumps)
                jumploc = jumps(check);

                % If the jump happens very early on, the first point is
                % likely spurious; if it happens very late, the last point
                % is also likely spurious. If the jump is small, there is
                % likely a blurry or narrow crack; fill it in. Otherwise,
                % split the crack into two for analysis of the first part
                % and send the rest back for the same set of tests
                if jumploc <= 2
                    linecrack = linecrack(jumploc+1:length(linecrack));
                elseif jumploc >= length(spacing) - 2
                    linecrack = linecrack(1:jumploc);
                    break
                elseif spacing(jumploc) <= 10
                    endpt = jumploc;
                    startpt = jumploc+1;
                    linecrack = [linecrack(1:endpt); ...
                        (linecrack(endpt)+1:linecrack(startpt)-1)'; ...
                        linecrack(startpt:length(linecrack))];
                else
                    crackparta = linecrack(1:jumploc);
                    if length(crackparta) > 5
```

```
                for ptentryA = 1:length(crackparta)
                     parCrack(parNum+ptentryA,:) = [parXY(1), ...
                         parXY(2), linecrack(ptentryA)];
                end
                parNum = parNum+length(linecrack);
            end
            crackpartb = linecrack(jumploc+1:length(linecrack));
            linecrack = crackpartb;
        end
        spacing = diff(linecrack);
        jumps = find(spacing>1);
    end

    % if the remaining length of crack after all spaces have been
    % accounted for is long enough, keep it
    if length(linecrack)>5
        for ptentryLeft = 1:length(linecrack)
           parCrack(parNum+ptentryLeft,:) = [parXY(1), ...
               parXY(2), linecrack(ptentryLeft)];
        end
        parNum = parNum+length(linecrack);
    end

% if there are a lot of jumps relative to the length of the
% identified points along the line, see if the part before the
% noise is long enough and keep, otherwise, discard
else
    linecrack = linecrack(1:jumps(1));
    if length(linecrack) > 5
        for ptentryStart = 1:length(linecrack)
            parCrack(parNum+ptentryStart,:) = [parXY(1), ...
                parXY(2), linecrack(ptentryStart)];
        end
        parNum = parNum+length(linecrack);
    end
end

% If there are identified bright points for that point, look at
% those points directly ahead of the final portion of the crack. If
% they don't begin too much later, add them to the crack
if ~isempty(whiteArt)
    extraWt = whiteArt(whiteArt>max(linecrack));
    if ~isempty(extraWt) && (min(extraWt)-max(linecrack))<4
        possExt = find(whiteArt > endNum-6);
        for addpt = 1:length(possExt)
            parCrack(parNum+addpt,:) = [parXY(1), parXY(2), ...
                possExt(addpt)];
            parNum = parNum+1;
        end
    end
end
```

```
    end
    morepts{ipt} = parCrack;
end

%% unpack the cell

crackpts = [];
crackFrontPts = [];
for ipt = 1:numUniqueXY
    if ~isempty(morepts{ipt})
        vecpts = morepts{ipt};
        crackpts = [crackpts; vecpts(:,1), vecpts(:,2), vecpts(:,3)];

        % deepest point for a given (x,z)
        topPt = find(vecpts(:,3)==max(vecpts(:,3)));
        crackFrontPts = [crackFrontPts; vecpts(topPt,:)];
    end
end

writematrix(crackpts, ['sam1_' state '_final_crack_pts.csv'])
writematrix(crackFrontPts, ['sam1_' state '_final_crack_front_pts.csv'])

%% rotated version of the crack plane for depth analysis

ang = -19.6*pi/180; % rotation angle for given sample
R = [cos(ang) -sin(ang) 0;sin(ang) cos(ang) 0;0 0 1];
crackRotated = crackpts*R;
xLimCrack = crackRotated(crackRotated(:,1)>200 & ...
    crackRotated(:,1)<1000,:);
goodAreaCrack = round(xLimCrack(xLimCrack(:,2)>730 & ...
    xLimCrack(:,2)<1900,:));
yLines = unique(goodAreaCrack(:,2));
maxinLine = zeros(length(yLines),1);
for iline = 1:length(yLines)
    yLine = yLines(iline);
    yLineData = goodAreaCrack(goodAreaCrack(:,2)==yLine,:);
    maxinLine(iline) = max(yLineData(:,3));
end
writematrix([yLines,maxinLine],['sam1_' state '_crack_front_line_rot.csv'])
```

Step 4: Calculate the crack front depth

```
plotSam1Fronts.m (and plotSam4Fronts.m)

% read in the front points (not all states had tomography)
baseStr = 'sam1_s0_crack_front_line_rot.csv';

pxSize = 1.172;

sOneFront = readmatrix(replace(baseStr,'0','1'))*pxSize;
sTwoFront = readmatrix(replace(baseStr,'0','2'))*pxSize;
```

```
sSixFront = readmatrix(replace(baseStr,'0','6'))*pxSize;
sNineFront = readmatrix(replace(baseStr,'0','9'))*pxSize;
sTwelveFront = readmatrix(replace(baseStr,'0','12'))*pxSize;
sThirteenFront = readmatrix(replace(baseStr,'0','13'))*pxSize;

% get the points across the hole (shifted because rotation wasn't around 0),
% consistent across states, as x
frontLocs = sSixFront(:,1)-855.5;

% use the angle of the cylindrical hole sections to get its location at all
% points (x,y)
mA = -10.377;
b = 544.29;
mC = 9.2658;

holeYA = frontLocs(1:457);
holeXA = (holeYA-b)/mA;
holeYC = frontLocs(458:1171);
holeXC = (holeYC-b)/mC;
fullholeX = [holeXA;holeXC];

% for each front, find its stats
[minOne, maxOne, meanOne, ptsOne] = getFrontData(sOneFront, 53);
[minTwo, maxTwo, meanTwo, ptsTwo] = getFrontData(sTwoFront, 80);
[minSix, maxSix, meanSix, ptsSix] = getFrontData(sSixFront, 65);
[minNine, maxNine, meanNine, ptsNine] = getFrontData(sNineFront, 68);
[minTwelve,maxTwelve,meanTwelve,ptsTwelve] = getFrontData(sTwelveFront, 73);
[minThirteen,maxThirteen,meanThirteen, ...
    ptsThirteen] = getFrontData(sThirteenFront, 69);

function [minD,maxD,meanD,ptsOI] = getFrontData(front,offset)
% get stats about the crack front; offset tells how much the hole position
% changed between datasets

% smooth it over a small region so any spurious points that made it out
% of the last filtering (usually in the center where ring artifacts often
% made persistent shadows) go away, also for nicer plotting
newFront = smooth(front(:,2)-offset*1.172,15);

% calculate its length from the hole at each x position
minD = min(newFront(100:1171))-fullholeX(newFront==min(newFront));
maxD = max(newFront(100:1171))-fullholeX(newFront==max(newFront));
meanDif = abs(newFront-mean(newFront));
meanD = mean(newFront(100:1171))-fullholeX(meanDif==min(meanDif));

% report a few points along the front to compare apart from overall depth
ptsOI = newFront([109,315,374,534,723,910,1020]);

end

end
```

S.3 Tessellation creation protocol in AlON

voronoiNoGroundTruth.m

```
state = 's1'; % state name
sam = 'sam4'; % sample name
displace = 1000; % value in um of center of first scan
confLim = 0.8; % minimum confidence to keep in tessellation
allGrains = readmatrix(['K:/' sam '_final_data/ff/' sam '_' state ...
    '_ff_sam_ao_individual_grain_stats.csv']);
grains = allGrains(allGrains(:,6)>=0.8, :);

numGrains = size(grains,1);


sideLen = 200; % number of voxels in each of x, y, and z

ycom = -grains(:,3) + displace; % adjust y to match tomography orientation
xyz = [grains(:,4), ycom, grains(:,2)]; % adjust x and z to match tomo
Eul = grains(:,25:27);
EulOne = Eul(:,1);
EulTwo = Eul(:,2);
EulThree = Eul(:,3);
Stress = grains(:,16:21);
IDs = grains(:,1);
rads = grains(:,5);

totRadV = sum(4 * pi * (rads.^3) / 3);

lims = [min(xyz) - 50; max(xyz) + 50]; % set extrema
Xpts = linspace(lims(1,1), lims(2,1), sideLen); % create voxel nodes
Ypts = linspace(lims(1,2),l ims(2,2), sideLen);
Zpts = linspace(lims(1,3), lims(2,3), sideLen);
[X,Y,Z] = ndgrid(Xpts, Ypts, Zpts);


% initialize for speed
grainDists = zeros(sideLen, sideLen, sideLen, numGrains);

for indgrain = 1:numGrains
    graincom = xyz(indgrain,:);
    grainrad = rads(indgrain);
    % calculate the distances of grain centroids to nodes
    grainDblock = sqrt((graincom(1) - blockCOM(1))^2 + ...
        (graincom(2) - blockCOM(2))^2 + (graincom(3) - blockCOM(3))^2);
    % create the power-distance
    grainDweight = 0.25 * grainDblock / maxD + 1.25;
    % adjust the distance with the power-distance
    grainDists(:, :, :, indgrain) = sqrt((X - graincom(1)).^2 - ...
        (Y - graincom(2)).^2 + (Z - graincom(3)).^2) + ...
        grainDweight * grainrad;
end
```

```
% find the grain with the minimum distance to each node
[~, minDists] = min(grainDists, [], 4);

% assign grain IDs; can use Euler or stress to create other representations
tessMatch = reshape(IDs(minDists), sideLen, sideLen, sideLen);
```